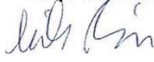# Koillismaa Deep Hole -
Final Report

Jonna Tirroniemi, Alan Bischoff, Michal Malinowski, Uula Autio, Tuomo Karinen, Vaula Lukkarinen, Suvi Heinonen, Perttu Mikkola, Tuomas Leskelä, Cedric Patzer, Kaiu Piipponen, Maarit Nousiainen, Petri Hakala, Ilkka Martinkauppi, Teemu Anttilainen, Jon Engström, Jukka Konnunaho, Pertti Telkkälä, Samuli Haavikko

21.12.2023   GTK/640/03.00/2020
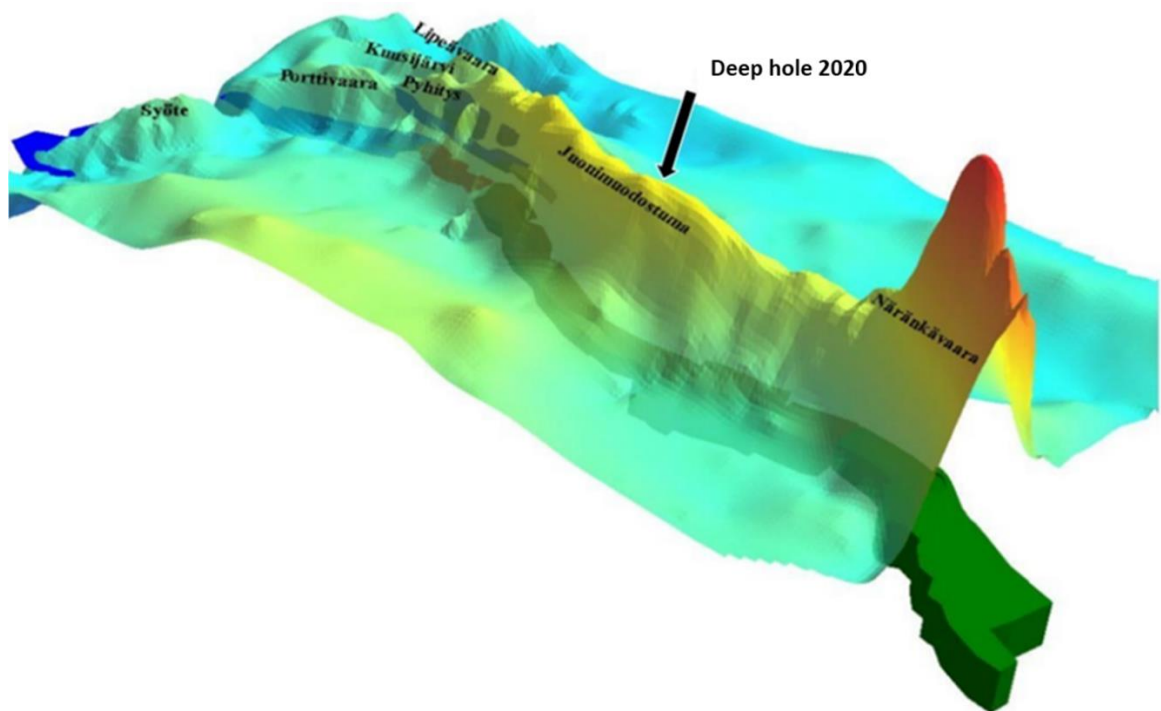
Cover Image. Gravity field intensity in the research area. Näränkävaara, Syöte, Porttivaara, Pyhitys, Kuusijärvi and Lipeävaara are surface-exposed layered intrusions. The deeper-seated 'dyke structure' connecting them within the crust is not observable from surface outcrops. (Salmirinne 2020)

GEOLOGICAL SURVEY OF FINLAND   DOCUMENTATION PAGE

Authors	Type of report
Jonna Tirroniemi, Alan Bischoff, Michal Malinowski, Uula Autio, Tuomo Karinen, Vaula Lukkarinen, Suvi Heinonen, Perttu Mikkola, Tuomas Leskelä, Cedric Patzer, Kaiu Piipponen, Maarit Nousiainen, Petri Hakala, Ilkka Martinkauppi, Teemu Anttilainen, Jon Engström, Jukka Konnunaho, Pertti Telkkälä, Samuli Haavikko	GTK Open File Work Report
	Commission by
	Geological Survey of Finland, Mineral Economy Solutions

Title of report
Koillismaa Deep Hole Final Report

Abstract
The primary objective of the Koillismaa Deep Borehole Project was to identify the source of potential field anomalies occurring between the Koillismaa and Näränkävaara intrusions. Based on the deep borehole drilling conducted in 2020, it was determined that the anomalies are caused by mafic and ultramafic plutonic rocks, which are genetically linked to the intrusions. This report describes the deep borehole drilled in Koillismaa and a series of multidisciplinary studies conducted at the drill site and the surrounding area from 2020 to 2023.

Keywords
Koillismaa deep hole, Koillismaa intrusion, Koillismaa Complex, gravity anomaly, potential field anomaly, feeder dyke, hidden dyke

Geographical area
Koillismaa, Kuusamo, Southern Kuusamo

Report serial		Archive code	
GTK Open File Work Report		4/2024	

Total pages	Language	Price	Confidentiality
73	English	N/A	Public

Unit	Project number
Mineral Economy Solutions	50402–20112

Signature/Name	Signature/name
Jonna Tirroniemi	Mika Posio

CONTENTS

1　INTRODUCTION

The Koillismaa area in eastern Finland has been of interest for several decades, primarily driven by the presence of the 2.45 Ga Koillismaa and Näränkävaara mafic–ultramafic layered intrusions and their associated Cu–Ni–PGE and V–Ti–Fe mineralizations. The 60-kilometre-long anomaly connecting the two intrusives (Figure 1) was originally observed in the 1950s, when the earliest ground gravimetric and airborne geophysical measurements were performed. Much scientific work has been conducted on the Koillismaa and Näränkävaara intrusions, but a remaining open question has been the origin of the Bouguer anomaly connecting the two complexes. Earlier studies applying potential field modelling have indicated that the upper surface of the anomaly's source is at ~1.5 km depth. However, direct evidence was lacking until recently. In 2020, GTK initiated a three-year research project named the Koillismaa Deep Hole, in which a 1724-metre-deep research borehole was drilled into the bedrock between Kuusamo and Taivalkoski (Figure 1).
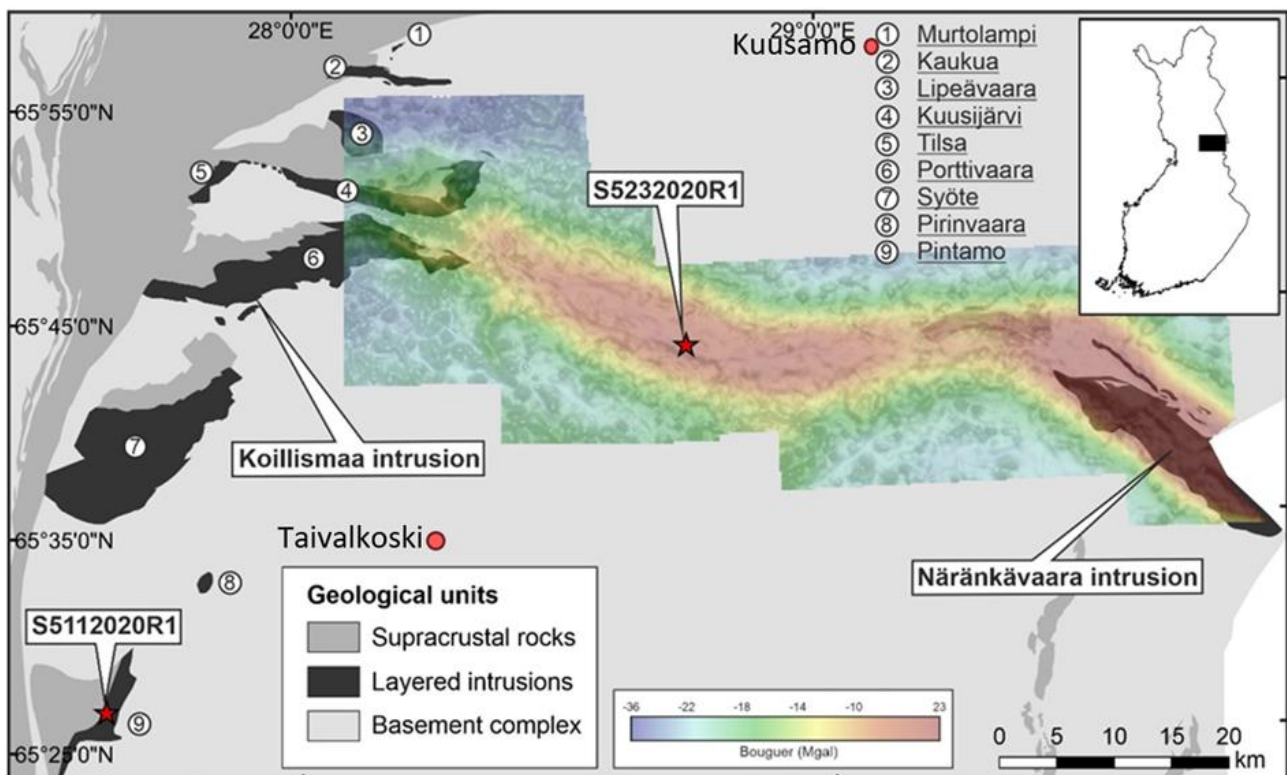

Figure 1. A simplified geological map over the Koillismaa area, with outcropping mafic–ultramafic intrusions of the Koillismaa intrusion complex (1. Murtolampi, 2. Kaukua, 3. Lipeävaara, 4. Kuusivaara, 5. Tilsa, 6. Porttivaara, 7. Syöte, 8. Pirinvaara, 9. Pintamo) and the Näränkävaara intrusion, which are connected by a strong gravimetric anomaly not explained by the rocks observed in outcrops. GTK's deep drilling sites from 2020 (Koillismaa deep hole: S5232020R1 and Pintamo: S5112020R1). (Thurman et al. 2023)

The focus of the study was on previously unexplored parts and features of the rocks, as well as on possible deeper extensions. The objectives of the research were to enhance fundamental knowledge of the formation of the bedrock in the area and to develop GTK's expertise in geophysical and geothermal modelling and interpretation. The project involved seismic and various applied geophysics studies during the 2022 field season, preceded by an extensive petrophysics sampling campaign from drill cores. The deep borehole provided substantial opportunities especially for

geothermal energy potential research, but also in general for mineral system studies, geological 3D modelling and rock mechanical studies. In addition to these, snow and soil geochemical studies were conducted in the vicinity of the deep borehole (Kinnunen, in preparation), and environmental conditions were monitored throughout the entire duration of the project through water, stream sediment and benthos sampling (Lukkarinen et al. in preparation). Furthermore, the Koillismaa Deep Hole project formed basis for the ERA-MIN-funded SEEMS DEEP project (1.5.2022–30.4.2025), which is developing a novel workflow for integrating seismic and electromagnetic (EM) methods for deep bedrock imaging and mineral exploration.

2 BACKGROUND

Over 30 mafic–ultramafic layered intrusions are emplaced in the NE Fennoscandian Shield, mainly in Finland and Russia (Figure 2) (Alapieti et al. 1990). These intrusions are located in the Kola and Karelian cratons, with ages ranging between 2.53–2.40 Ga (Bayanova et al. 2019). Intrusions within the Karelian craton are concentrated around the age of 2.44 billion years, with some of these hosting orthomagmatic ore deposits (Iljina & Hanski 2005; Iljina et al. 2015).

The study area lies within the Karelia Province in central Finland, a collage of Precambrian accretionary terranes and remnants of oceanic crust that constitute part of the Fennoscandian Shield. During the Archean, mantle segregation and continental growth gave rise to ~2.80 Ga TTG (tonalite–trondhjemite–granodiorite) gneisses that were migmatized and intruded by leucogranites at ~2.70 Ga (Lauri et al. 2006; Hölttä et al. 2021). Rifting of the Archean crust began at 2.44 Ga, resulting in voluminous mafic–ultramafic magmatism along with a few A-type granitic intrusions and episodic emplacement of dyke swarms until 1.98 Ga (Vuollo and Huhma 2005; Lauri et al. 2012; Kärenlampi et al. 2019).

The onset of the Svecofennian orogeny at ~1.91 Ga initiated a compressional tectonic phase that resulted in multiple continental collisions and the development of large-scale shear zones that remained active until at least 1.79 Ga (Kontinen et al. 2013; Nironen 2017). This event induced metasomatic alterations in the Karelian crust, predominantly within narrow shear zones (Pajunen and Poutiainen 1999), and more widespread rehydration reactions that affect both the Archean and Paleoproterozoic rocks (Hölttä and Heilimo 2017). At the end of the Paleoproterozoic, the Karelia Province became a stable craton, experiencing only limited subsequent deformation events related to orogens in western Fennoscandia, localized intraplate magmatism and glacial-isostatic adjustments (Kohonen and Rämö 2005).
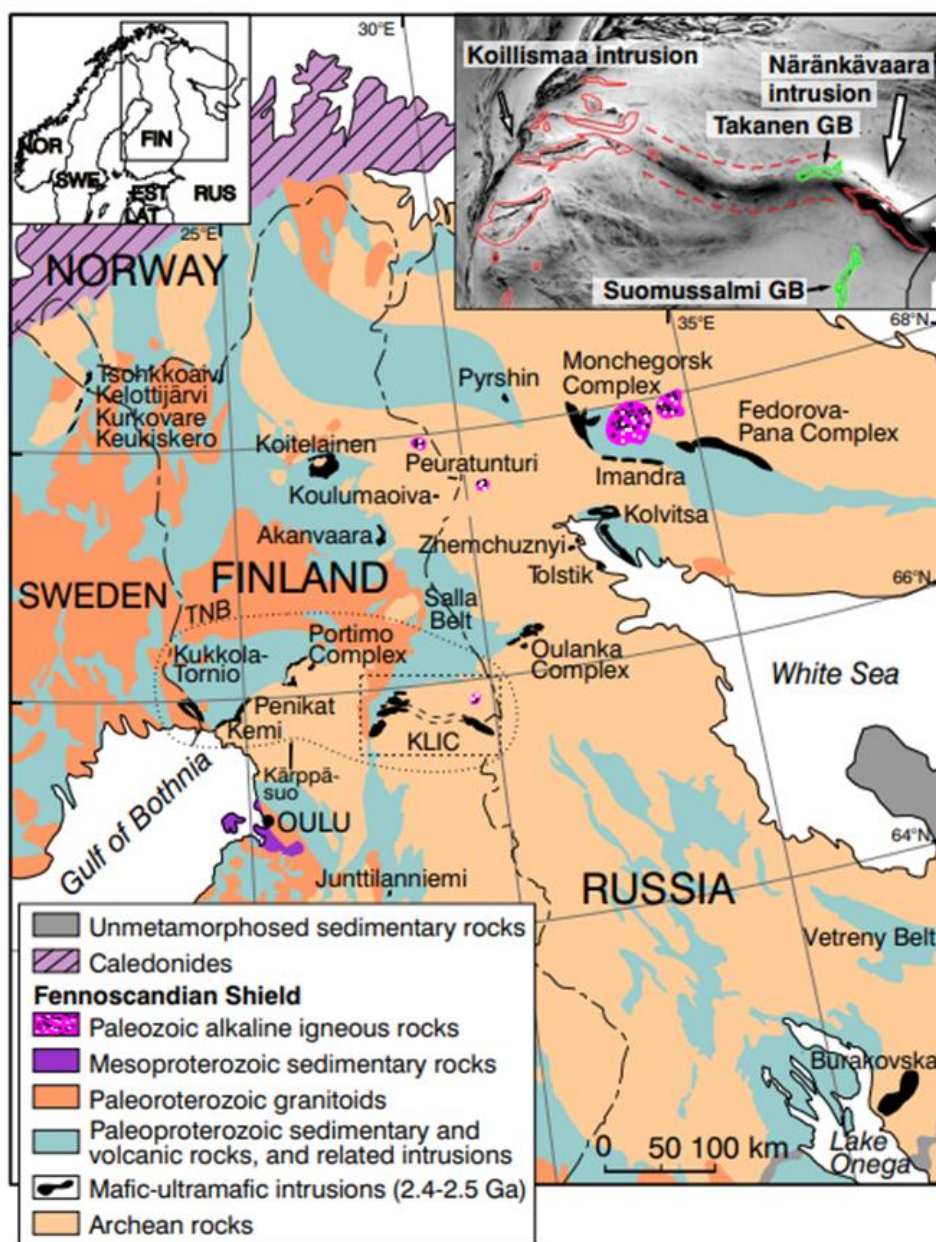
Figure 2. Geological map of the Fennoscandian shield showing the distribution of 2.53–2.39 Ga mafic–ultramafic intrusions. The Koillismaa–Näränkävaara layered intrusion complex (KLIC) and gravity anomaly on a magnetic map in the upper right corner. (After Alapieti 1990, Karinen 2010 and Järvinen 2022)

The Koillismaa–Näränkävaara Layered Igneous Complex (KLIC) is comprised of two mafic–ultramafic intrusions connected by a positive unexposed magnetic and gravity anomaly, with a total length of about 100 km (Alapieti 1982; Karinen 2010; Järvinen et al. 2022). These intrusions formed approximately 2440 million years ago, when magma rose from deep within the Earth's mantle and crystallized in the upper portions of the rifting intracratonic Archean continental crust.

The gravity anomaly connecting the intrusions is known as the 'hidden dyke' (Alapieti 1982) or 'feeder dyke' (Figures 1 and 2). The anomaly, the Näränkävaara intrusion and the Koillismaa complex have been studied in various projects. The most significant of these was the so-called Koillismaa

Research Project on the ore-critical areas of Koillismaa conducted by the University of Oulu during 1971 to 1976 (Piirainen et al. 1978), through which understanding of the complex structure largely took its current form.

Näränkävaara stands out for its unique composition, in which about half of its cumulate stratigraphy is dominated by olivine adcumulates, while the other intrusions are generally more pyroxenitic. The Koillismaa intrusion complex units are, on average, more evolved, pyroxenitic–gabbroic, compared to the dunite–pyroxenite-dominated Näränkävaara intrusion (Figure 3) (Karinen 2010; Järvinen et al. 2022).
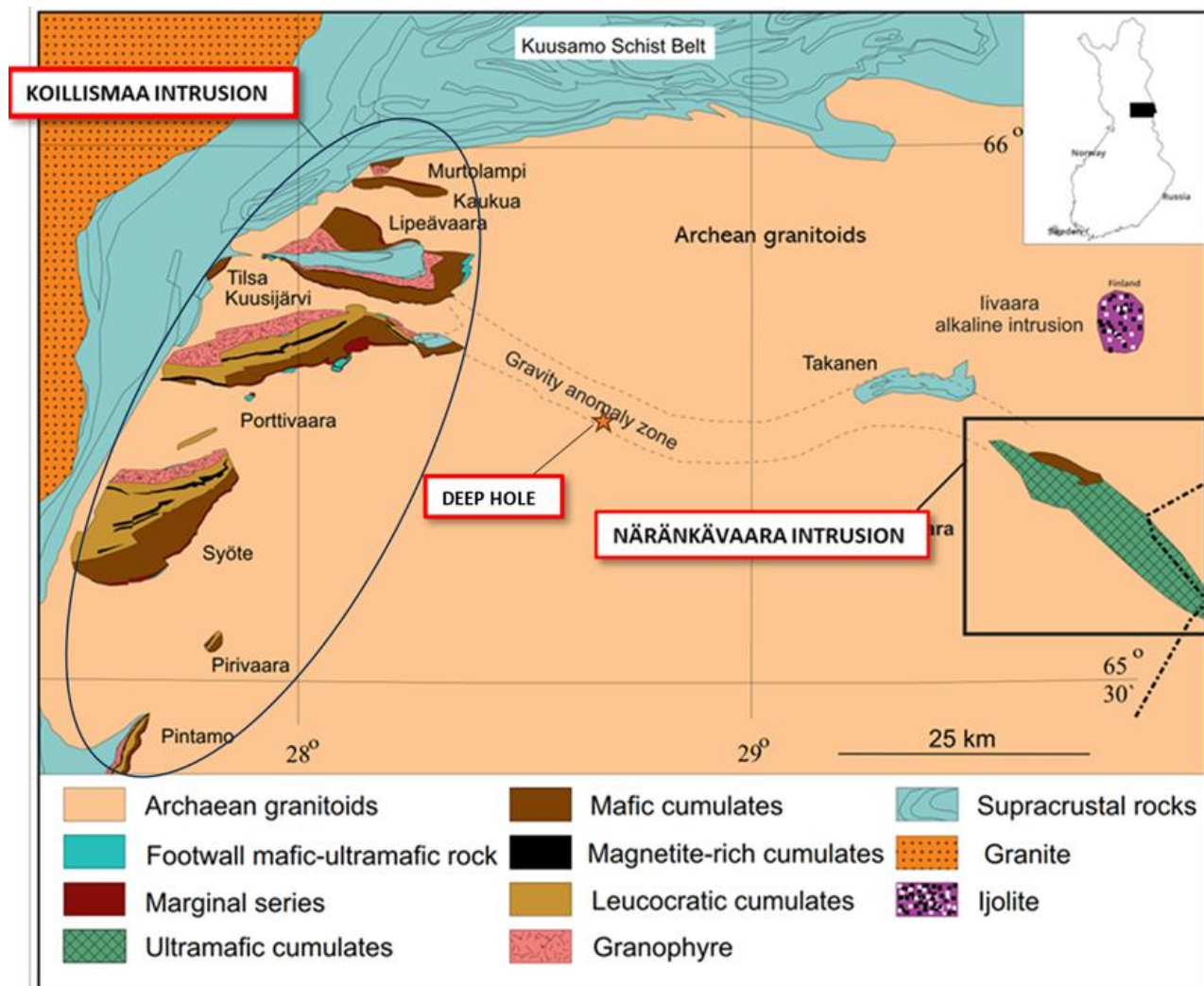
Figure 3. Basic lithological units over Koillismaa, with the deep drillhole indicated with a red star. (Modified after Karinen 2010)

GTK attempted to drill through the connecting gravity anomaly during 2003–2004 at the Takanen greenstone belt (DD R339). At that time, based on computational models, it was expected that the answer to the anomaly's cause would be found at a depth of around 1500 metres, but the drilling had to be abandoned at a depth of 1200 metres due to technical difficulties (Iljina et al. 2006).

In 2020, a new drilling programme was planned for Koillismaa, aiming for a depth of 3 kilometres.

3   STUDY AREA

The 2020 drilling site was located in southern Kuusamo, near the southern border of Kuusamo city and the northern Taivalkoski municipality border (Figure 4), where GTK had a valid reservation area during 2020–2022. Since then, an exploration permit has been applied for covering the same area.
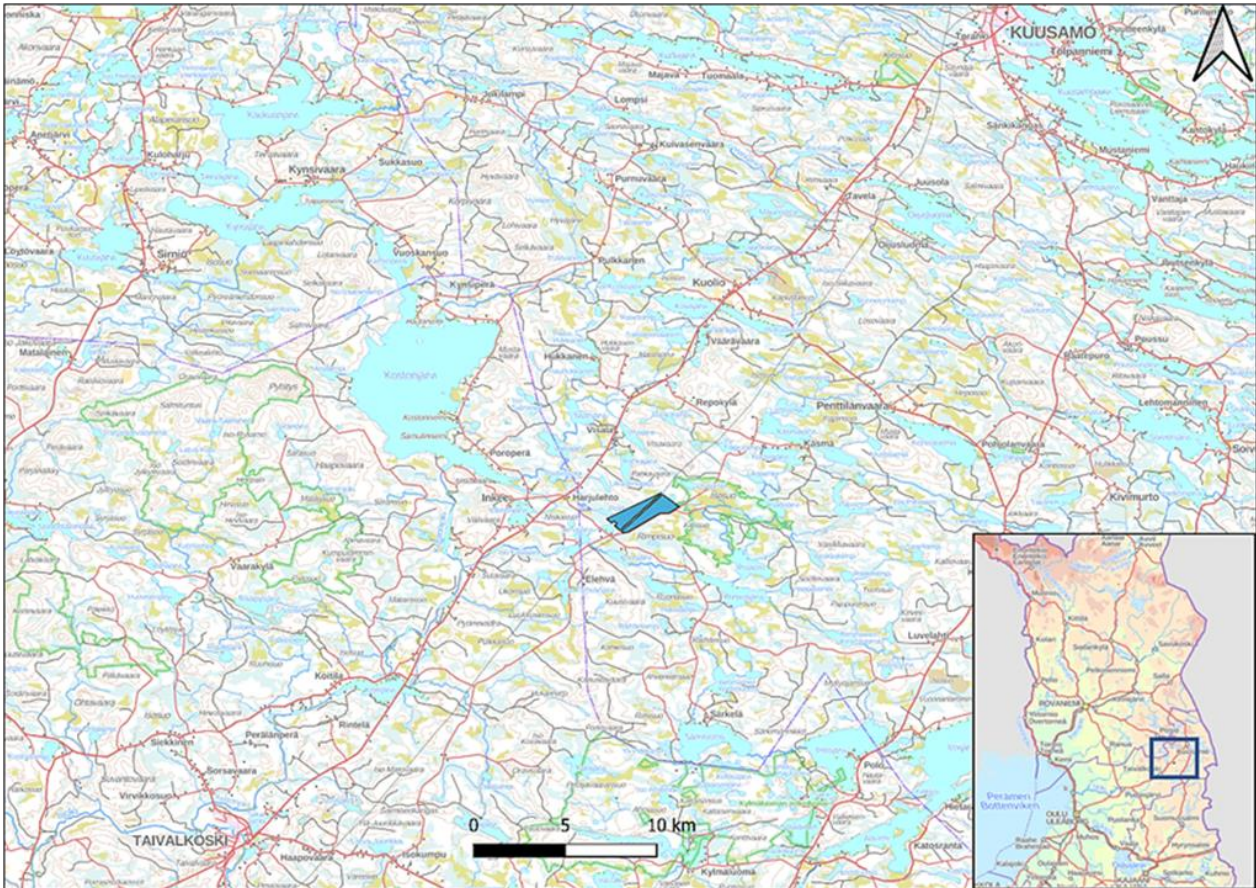

Figure 4. Location of the old reservation and current exploration permit application area (blue) in southern Kuusamo.

Near the study area, there are several partially overlapping conservation areas: 1) a Natura 2000 area named Isosuo–Kivisuo (FI1101617), 2) a bog conservation area known as Isosuo–Kivisuo (SSA110073), 3) a private nature reserve called Pahka-aho (YSA250044), 4) a conservation programme area for the old forests of Visavaara (AMO110220) and 5) a bog conservation programme area, Isosuo–Kivisuo (SSO110370). Figure 5 shows the most important conservation areas in the vicinity of the study programme. The Natura 2000 area Isosuo–Kivisuo (FI1101617) and the conservation programme area for the old forests of Visavaara (AMO110220) are approximately 60 metres away from the drilling site, while the bog conservation area Isosuo–Kivisuo (SSA110073) and the bog conservation programme area Isosuo–Kivisuo (SSO110370) are about 1200 metres away from the drilling site (Figures 5 and 6).
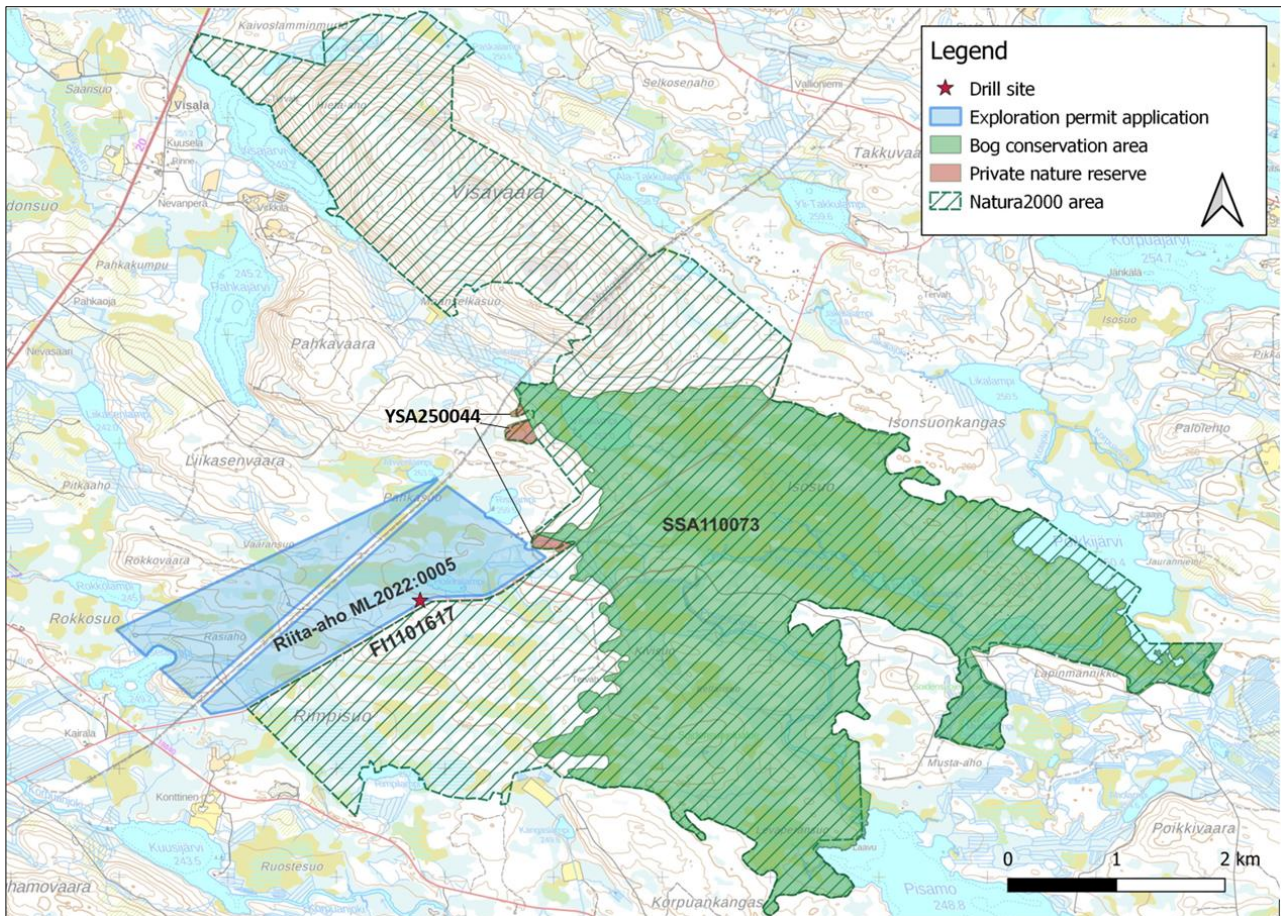
Figure 5. The most important protected areas in the vicinity of the deep drillhole (red star): A bog conservation area (green), private nature reserve areas (red) and an overlapping Natura2000 area (green stripes).

4   CONDUCTED STUDIES

4.1   Drilling programme

The drilling programme started with an ambitious plan to drill down to 3 km depth. The contractor performing the drilling was Arctic Drilling Company Ltd (ADC) from Rovaniemi. ADC uses diamond drill rigs of their own design and construction. The drilling started in September 2020 and continued until 1 March 2021. The drilling project started with rig model K5, with a 30-m cemented anchoring hole (diameter 96 mm). Anchoring commenced on 23 September and was planned to prevent resonation of the rig once the core reaches a certain depth. Drilling, after the anchor hole, started on 24 September.

At the beginning of the drilling campaign, fractured bedrock caused serious technical challenges down to 300 m, which mostly showed up as continuous losses of water pressure and jamming of the drill pipes. Therefore, a decision was eventually made to use 96 mm rods (HQ) as a casing for the first 300 m.
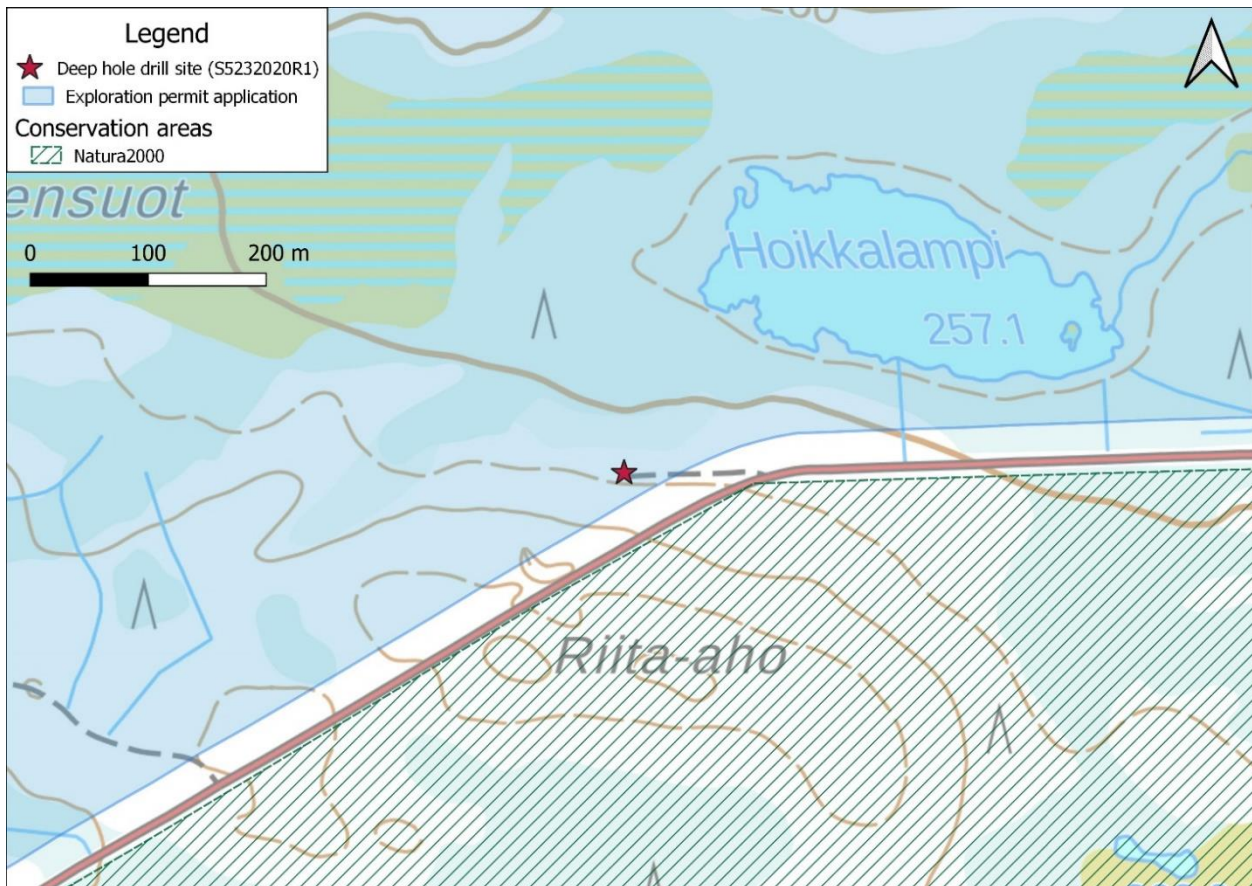
Figure 6. Drill site at Poikkivaarantie, SW of Hoikkalampi (N = 7290550 ja E = 579780).

The rig was eventually changed to a more powerful K10 version when the first half of the planned length was reached in December 2020. The change to a more powerful drill rig was planned to ensure that the drilling would reach the targeted 3000 m depth. The K10 was in theory capable of reaching depths of 3500 m.

After numerous technical issues with the rig and mechanically very challenging bedrock conditions, the main hole was drilled to a depth of 1724.70 metres. After a break in drilling during the Christmas holidays, it was observed that the main hole had collapsed. The new rig couldn't pass through the collapsed zones after several attempts. To circumvent the fractured zone, a bypass hole was commenced on 20 February 2021, from depth of 1419 metres after the lowering of a wedge. The bypass hole was drilled to a depth of 1594.9 metres before it was discontinued on 1 March 2021, due to scheduling reasons, after four months of drilling in total.

Originally, drilling was planned to continue later in 2022 or 2023, but due to timing, technical and economic reasons, the plan was ultimately abandoned.

Figure 7. ADC drill rig K5 settling at the drilling site in Koillismaa in autumn 2020. Hoikkalampi visible in NE.

4.2   Simplified lithology of the drill core

The uppermost 658 m of this borehole penetrated TTG (tonalite–trondhjemite–granodiorite) gneisses that are intruded by leucogranites and diabase dykes of varying widths. The central section (658–1410 m) consists of homogeneous granites and quartz diorites (Figure 8). Below 1410 m, granites interfinger and locally intermingle with mafic–ultramafic rocks that correlate with the layered intrusions of the Tornio–Näränkävaara belt (Alapieti et al. 1990; Lauri et al. 2006). The ultramafic rocks were identified as the source of the gravity anomaly, and as they continued until the end of the drillhole, their depth extent remains open.

Age determinations from zircon and baddeleyite grains of ultramafic rocks have confirmed that they are of the 2.45 Ga age at the two exposed intrusions in Koillismaa, the Koillismaa intrusion and Näränkävaara intrusion (Karinen et al. in preparation). Therefore, as had already been anticipated, the exposed intrusions belong to one layered intrusion complex where the unexposed mafic–ultramafic part studied in this project is its significant part and is named here as the Koillismaa Deep Intrusion (KDI). In the drill core, the mafic rocks of the KDI show a distinct chilled margin with the granite, and our future study will focus on the chilled margin and its usability as the parental magma candidate of the intrusion. The two exposed layered intrusions of KLIC have been linked into

compositionally different magma types, and in our future contribution, to be submitted for review during 2024, we examine how the chilled margin of the KDI could be linked with the proposed parental magmas of the exposed intrusions. Figure 8 presents micro-textures of the rocks of the KDI.

The gneisses were dated as Archean (2.9–2.8 Ga), with locally intense alteration and shearing occurring at ~2.7 Ga. Younger granites and granodiorites and diabase dykes crystallized at ~2.44 Ga (Anttilainen 2023). Geochemically, the younger granitoids exhibit an anorogenic A-type signature, whereas the diabase dykes have a calc-alkaline composition (Anttilainen 2023). Collectively, structural, petrological, geochronological and geochemical observations strongly indicate that Proterozoic felsic and mafic melts were coeval, both belonging to the ~2.44 Ga bimodal magmatism related to the rifting of the Archean crust. For a description of the observed felsic units, their geochemistry and age determinations, see the M.Sc. thesis of Anttilainen (2023). The material collected for the thesis will be published as a peer-reviewed article, to be submitted for review during 2024.
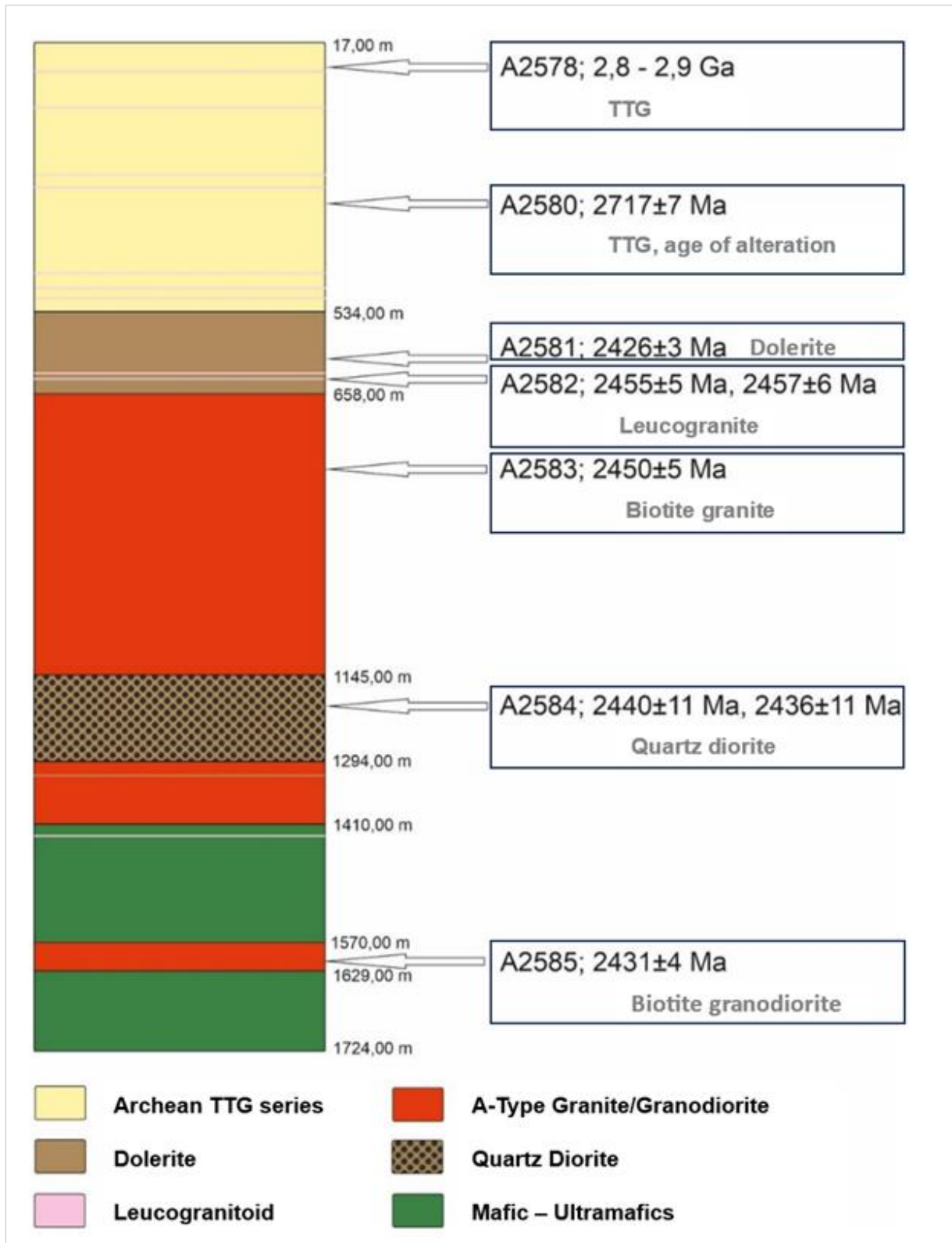
Figure 8. A rock column for the hole and age determination results from Anttilainen (2023). Note that the age results have larger uncertainties than indicated by the given 2σ errors.
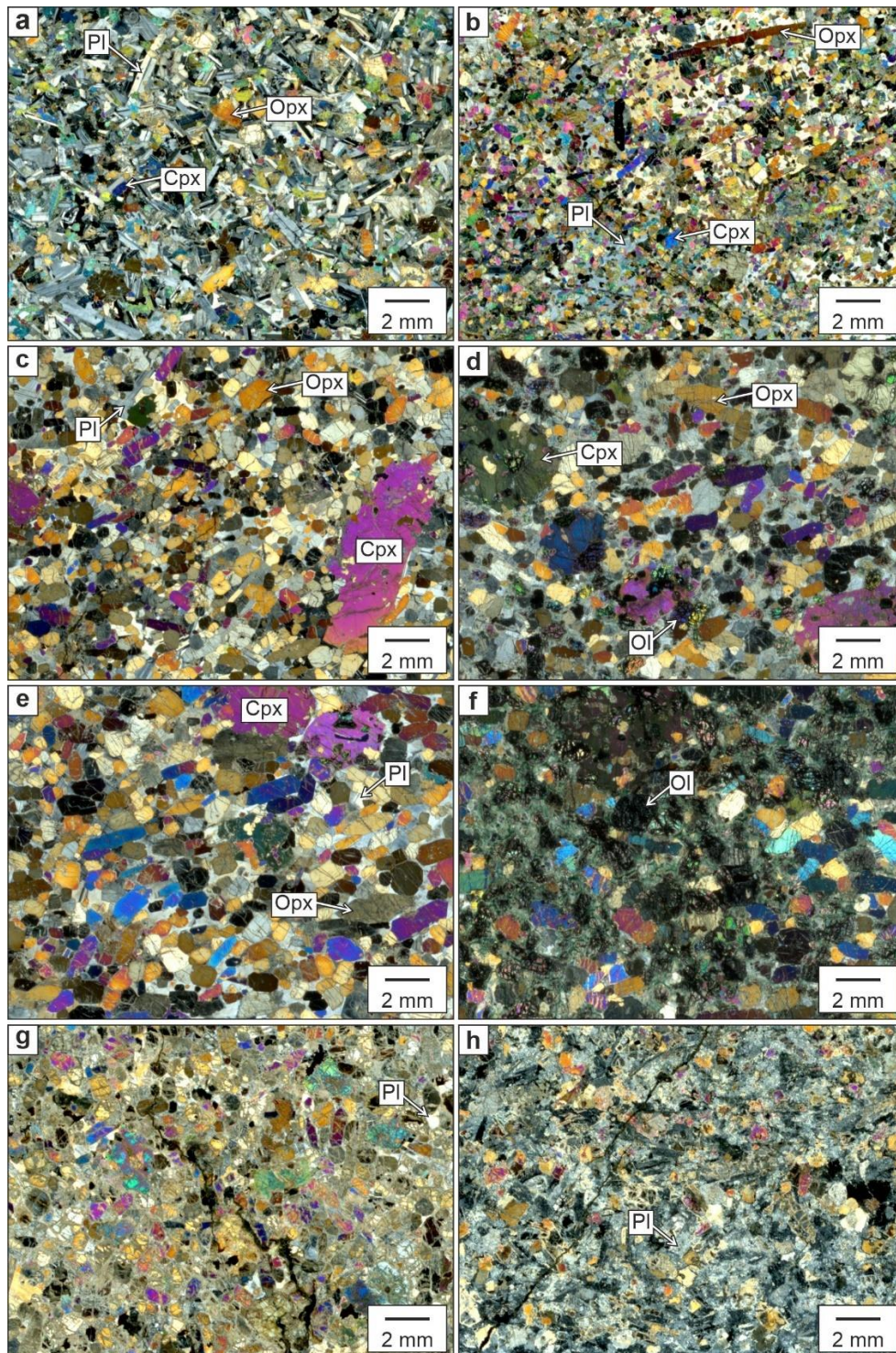
Figure 9. Photomicrographs illustrating textural varieties in the KDI. (a) Equigranular orthopyroxene gabbro (chilled margin) at 1440.5 m in the core, (b) orthopyroxene melagabbro at 1447.80 m in the core, (c) clinopyroxene melanorite at 1475.43 m in the core, (d) clinopyroxene-bearing olivine melanorite at 1488.90 m in the core, (e) olivine-bearing clinopyroxene melanorite at 1508.15 m in the core, (f) lherzolite at 1514.60 m in the core, (g) clinopyroxene melanorite at 1696.95 m in the core and (h) olivine-bearing clinopyroxene melanorite at 1722.65 m in the core. All photomicrographs were taken with a cross-polarized light source. Abbreviations: Pl = plagioclase, Opx = orthopyroxene, Cpx = clinopyroxene, Ol = olivine.

4.3   Mineral system studies

The mineral system studies focused on Ni–Cu–PGE mineralization, and according to a visual log of the dill core, the mafic part of the core does not contain any indications of sulphide mineralization. The core only includes some trace amounts of Cu–Ni–sulphide minerals, and the Ni–Cu concentrations are therefore relatively low. According to geochemical analyses, the core is not PGE mineralized.

4.4   Geophysical studies

4.4.1   Petrophysical studies

Samples for petrophysical measurements were collected at approximately 1-m intervals from the Koillismaa drill core. The depths of the samples are from 18 m down to 1594 m, with a total of 1227 samples. Petrophysical studies were conducted in the GTK laboratory and included density, magnetic susceptibility, magnitude and direction of magnetic remanence, electric resistivity both with inductive and galvanic measurement and seismic P-wave velocity measurements. Drill core samples were re-classified into 12 main rock classes to facilitate the plotting and utilization of petrophysics in the geological interpretation and geophysical modelling.

In addition to the laboratory measurements of density and seismic P-wave velocity, we also used sonic logging and a Surfer UK1401 hand-held ultrasonic device to measure P-wave velocity at the Koillismaa study site. Sonic logging was conducted by Astrock Oy in autumn 2021 with a 4-channel sonde. A multichannel sonde provides reliable velocity estimates of the rock forming the drillhole wall. At the Koillismaa site, a major fracture zone causes instability of the drillhole at a depth of approximately 1045 m, and it was not possible to perform sonic logging below this depth. The upper part of the drillhole down to the depth of 200 m is cased, preventing velocity measurement of the rock wall with sonic logging.

According to Heinonen et al. (2022), velocities measured in the laboratory are typically higher compared to the values from other methods. For example, the average velocity for granite was 5910 m/s in the laboratory measurement, while sonic logging gave a velocity of 5870 m/s. Sonic logging results are influenced by fracturing of the drillhole site, while samples in the laboratory represent intact rock. The handheld device used for P-wave velocity measurement was a Surfer UK1401, and it gave approximately 85% lower velocity values than laboratory measurements. The Surfer UK1401 is very easy and fast to use, but it requires an intact core with a minimum length of 15 cm (distance between the transmitter and receiver), which can be problematic when the core is fractured, such as in Koillismaa. The UK1401 is also extremely sensitive to small fractures and cracks in the drill core, as well as to the positioning of the device. This results in high variability in velocity values. Each measurement point was repeated three times to achieve a more reliable result.

Petrophysical data are plotted together with lithologies in Figure 10 from 320 m down to 920 m depth. Data for the full length are presented in Appendix 1 (Koillismaa petrophysics.pdf). P-wave velocity is sensitive to fractures and the texture of rocks, which is reflected in highly variable values, especially in sonic measurements. Density has a stable correlation with lithologies, showing increased values in dolerite dykes and mafic intrusives. Furthermore, susceptibility and resistivities measured with galvanic and inductive methods show increased values in mafic rocks. The inclination and
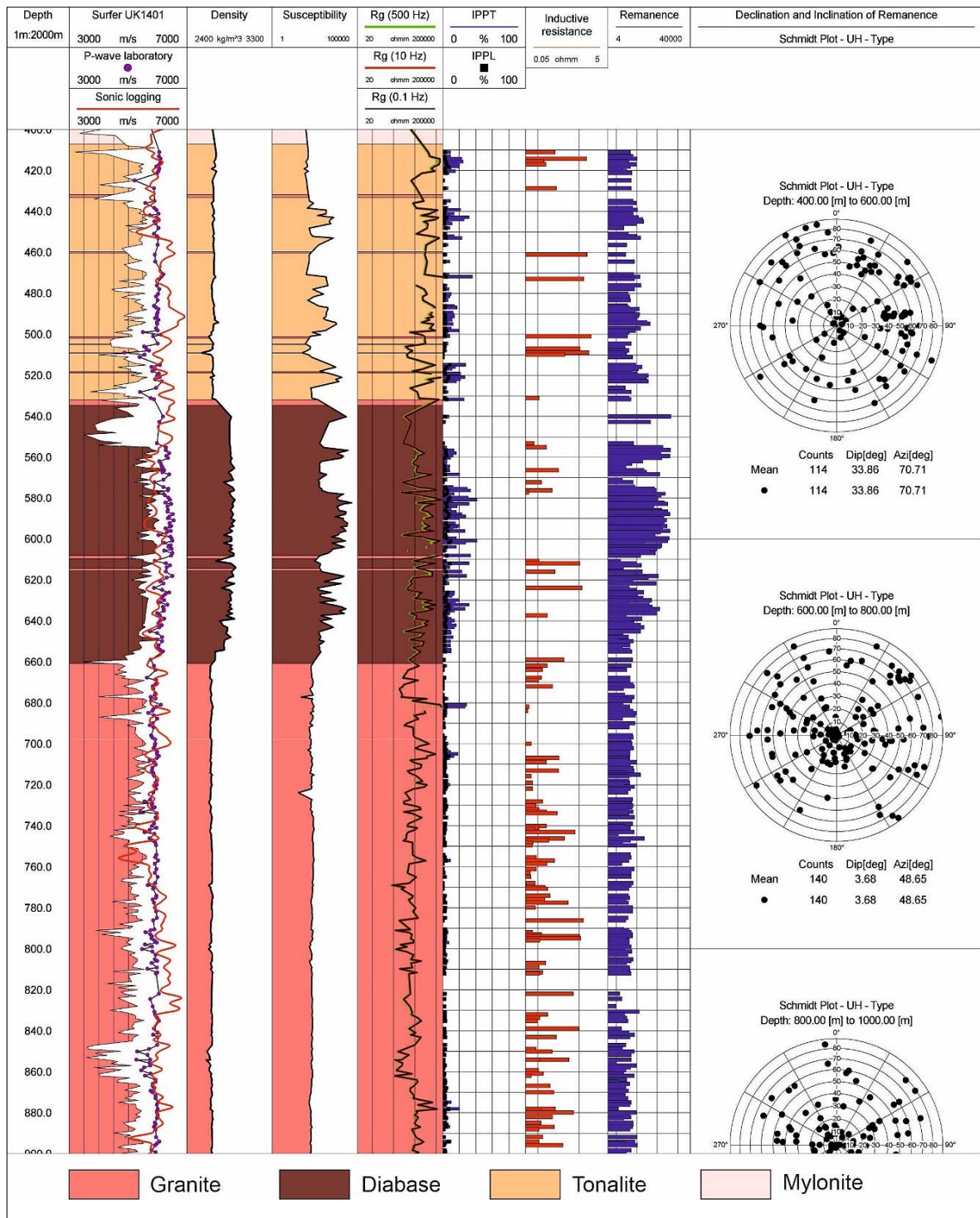
Figure 10. A summary of petrophysical measurements in the Koillismaa drillhole. Seismic P-wave velocity was measured with three methods: using a handheld Surfer UK1401 device, in the laboratory from drill core samples and by sonic logging in the drillhole. Petrophysical measurements in the GTK geophysics laboratory included measurements of density, susceptibility, galvanic resistivity (Rg) with three different frequencies, inductive resistance and the strength, inclination and declination of remanence. The inclination and declination of remanence is presented in a polar and rose diagram.

Based on measured galvanic resistivities, IP chargeability terms PL and PT are determined. The whole drillhole length is visualized in Appendix 1 (Koillismaa_petrophysics.pdf).

declination of remanence have very high variability, and no general direction is possible to estimate with the data presented here. The average values of the main petrophysical parameters are listed in Table 1 and all measured values are available in Appendix 2 (KoillismaaDDH_PetrophysicalData.xlsx).

Table 1. Results of the petrophysical measurements of density, P-wave velocity, susceptibility and remanence for each rock type based on generalized lithological classification and classification from the drill core logging reports. A full listing of the petrophysical measurement results is provided in **Appendix 1** (KoillismaaDDH_PetrophysicalData.xlsx).

Lithological grouping and lithologies	Number of samples	Average of Density	Average of Velocity	Average of Susceptibility	Average of Remanence
Archean basement gneiss	**214**	**2678.46**	**5848.52**	**554.34**	**71.248**
Granodiorite	4	2646.75	5335.33	117.75	68.000
Tonalite	210	2679.07	5855.85	562.66	71.310
Archean basement gneiss (altered)	**12**	**2658.17**	**5510.17**	**109.08**	**42.000**
Granodiorite	12	2658.17	5510.17	109.08	42.000
Archaean basement gneiss (highly altered)	**80**	**2702.45**	**6032.35**	**114.90**	**51.800**
Granite	79	2703.20	6037.90	115.38	51.658
Mylonite	1	2643.00	5594.00	77.00	63.000
Diabase	**109**	**2859.88**	**6247.14**	**5878.00**	**1025.807**
Diabase	106	2855.72	6254.50	6022.58	1053.236
Schist	3	3007.00	5987.00	769.33	56.667
Diabase (altered + sheared)	**1**	**2869.00**		**578.00**	**36.000**
Schist	1	2869.00		578.00	36.000
Gabbronorite (2.44 Ga)	**29**	**2890.00**	**6498.62**	**6049.07**	**2951.448**
Gabbronorite	26	2896.15	6545.50	6695.04	3269.500
Granite	3	2836.67	6092.33	450.67	195.000
Granite dyke (2.44 Ga)	**422**	**2668.20**	**5812.26**	**209.77**	**46.976**
Granite	380	2668.55	5840.77	210.13	43.645
Granodiorite	38	2666.32	5502.63	213.76	80.158
Tonalite	4	2653.25	6044.75	137.25	48.250
Granite dyke (unknown age)	**11**	**2651.45**	**5861.82**	**201.64**	**52.273**
Granite	11	2651.45	5861.82	201.64	52.273
Leucogranite dyke (unknown age)	**8**	**2623.63**	**5672.88**	**61.88**	**43.500**
Granite	8	2623.63	5672.88	61.88	43.500
Peridotite (2.44 Ga)	**66**	**2891.47**	**6075.56**	**59 334.02**	**16 212.485**
Peridotite	66	2891.47	6075.56	59334.02	16 212.485
Pyroxenite (2.44 Ga)	**40**	**3125.80**	**6759.82**	**5175.50**	**1362.800**
Peridotite	4	3151.25	6657.50	22 831.00	9158.000
Pyroxenite	36	3122.97	6771.51	3213.78	496.667
Quartz diorite dyke (2.44 Ga)	**93**	**2776.29**	**5836.69**	**1405.70**	**82.634**
Diorite	80	2765.36	5818.09	1112.96	69.175
Quartz diorite	13	2843.54	5951.15	3207.15	165.462
Grand Total	**1085**	**2737.23**	**5946.31**	**4876.37**	**1262.953**

4.4.2   Seismic studies

In September 2022, a combined surface and borehole seismic survey was performed in the vicinity of the Koillismaa drillhole (Figure 11). A ca. 7.5-km-long seismic profile was acquired, together with a multi-offset multi-azimuth vertical seismic profile (VSP) recorded by the fibre-optic cable deployed in the Koillismaa borehole with distributed acoustic sensing (DAS) technology. Vibroseis and explosive shots dedicated to VSP acquisition were also recorded along the seismic profile, forming a quasi-3D survey layout. The primary objectives of the survey were to (i) provide further constraints on the Koillismaa intrusion and verify the reflectivity present in 2018 seismic data and (ii) test a novel method for acquiring VSP data with a fibre-optic cable and DAS technology.
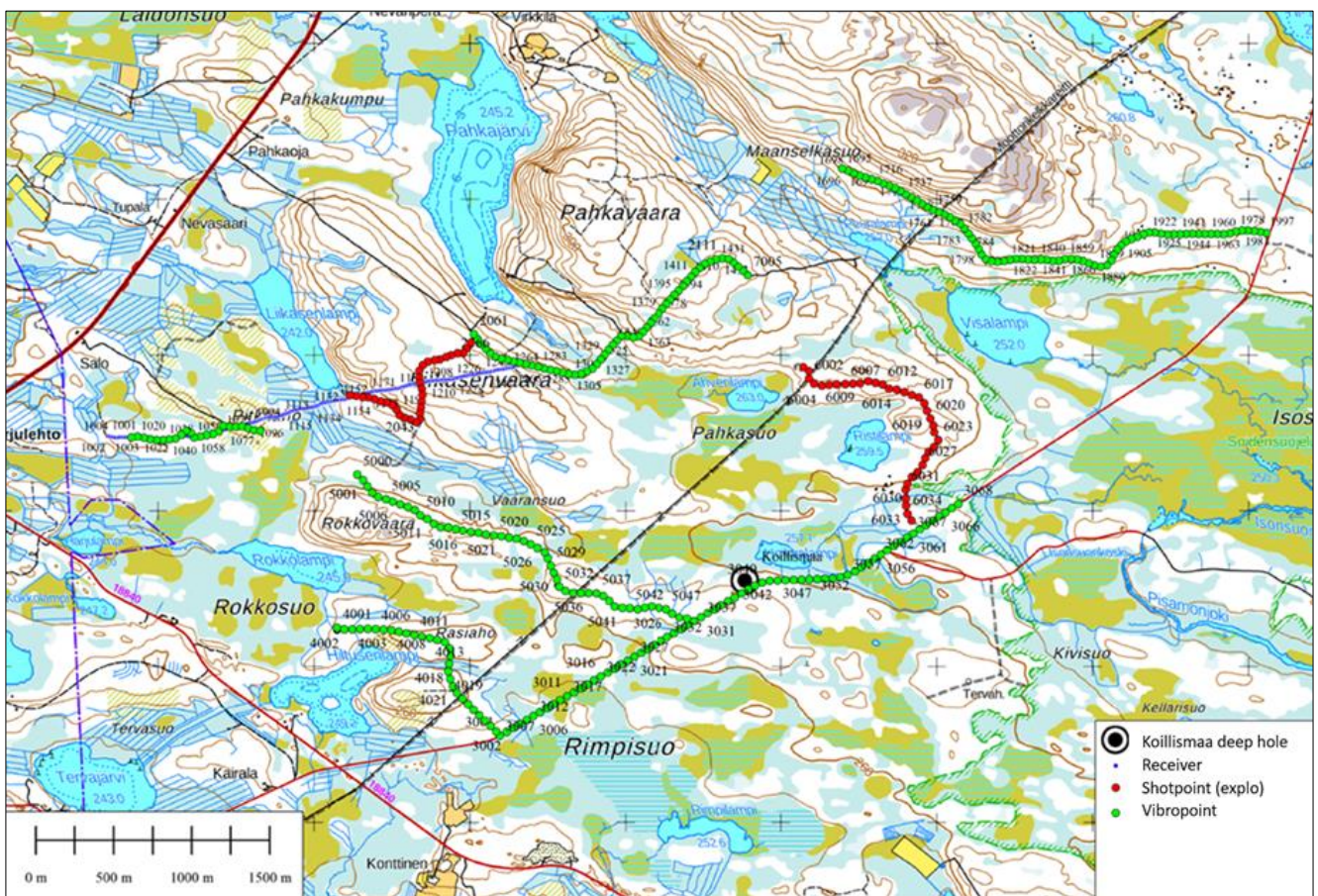

Figure 11. Base map indicating the location of the Koillismaa 2022 seismic project. Green dots = Vibroseis points, red dots = explosives, blue dots = surface seismic receiver positions.

4.4.2.1   2D seismic profile

Recording along the KOSE2022 2D profile was performed using a Flex-EPOS pool of three-component (3C) receivers (GSB nodes) and 3C geophones (https://wiki.helsinki.fi/display/FLEX/Large-N+Devices). A mix of Vibroseis and explosive seismic sources was used. Vibroseis acquisition was conducted with a Failling Y-2400 Vibrator (22 t peak force) mounted on a Mark IV buggy (provided by Geopartner

Geofizyka). For explosive shot points, a small charge (240 g or 120 g) at 2 m depth was used. The 2D receiver profile recorded all shot positions, including those meant for the VSP survey. The acquisition parameters are summarised in Table 2.

Table 2. The main acquisition parameters for the 2022 Koillismaa seismic profile

Receivers	Geospace GSB-3C
Geophones	Single 3C GS-ONE 5Hz, planted with inline towards higher station #
Sample rate	1 ms
Gain	6 dB
Polarity	SEG
Nominal spread	all live
Max. available channels	752
Receiver interval	10 m
Source interval	40 m for 2D or 50 m for VSP
Source	Mark-IV Vibroseis truck (22 t peak force) + explosives (240 / 120 g charge @ 2 m depth)
Sweep parameters	20–160 Hz, 20 s, +1dB per octave
Source polarity	SEG
No. of sweeps per VP	3 (2D) or 6 (VSP)
Record length (s)	6

The quality of the recorded data was very good, especially from the Vibroseis sources, including the offset ones (used for VSP). An example of a shot gather is presented in Figure 12. Initially, data were processed as a crooked-line profile using only inline sources. The processing flow consisted of the following steps: a) a crooked line geometry setup with CDP bins spaced at 5 m, b) matching of dynamite sources to Vibroseis sources, c) refraction statics based on manually picked first breaks, d) coherent noise suppression (median filter, airwave mute), e) bandpass filter, f) AGC scaling, g) dip-moveout (DMO) correction with V = 5800 m/s, h) stacking of DMO-corrected gathers, i) post-stack time migration (Stolt) with V = 6000 m/s, j) post-stack coherency filtration and k) time–depth conversion with V = 6000 m/s.
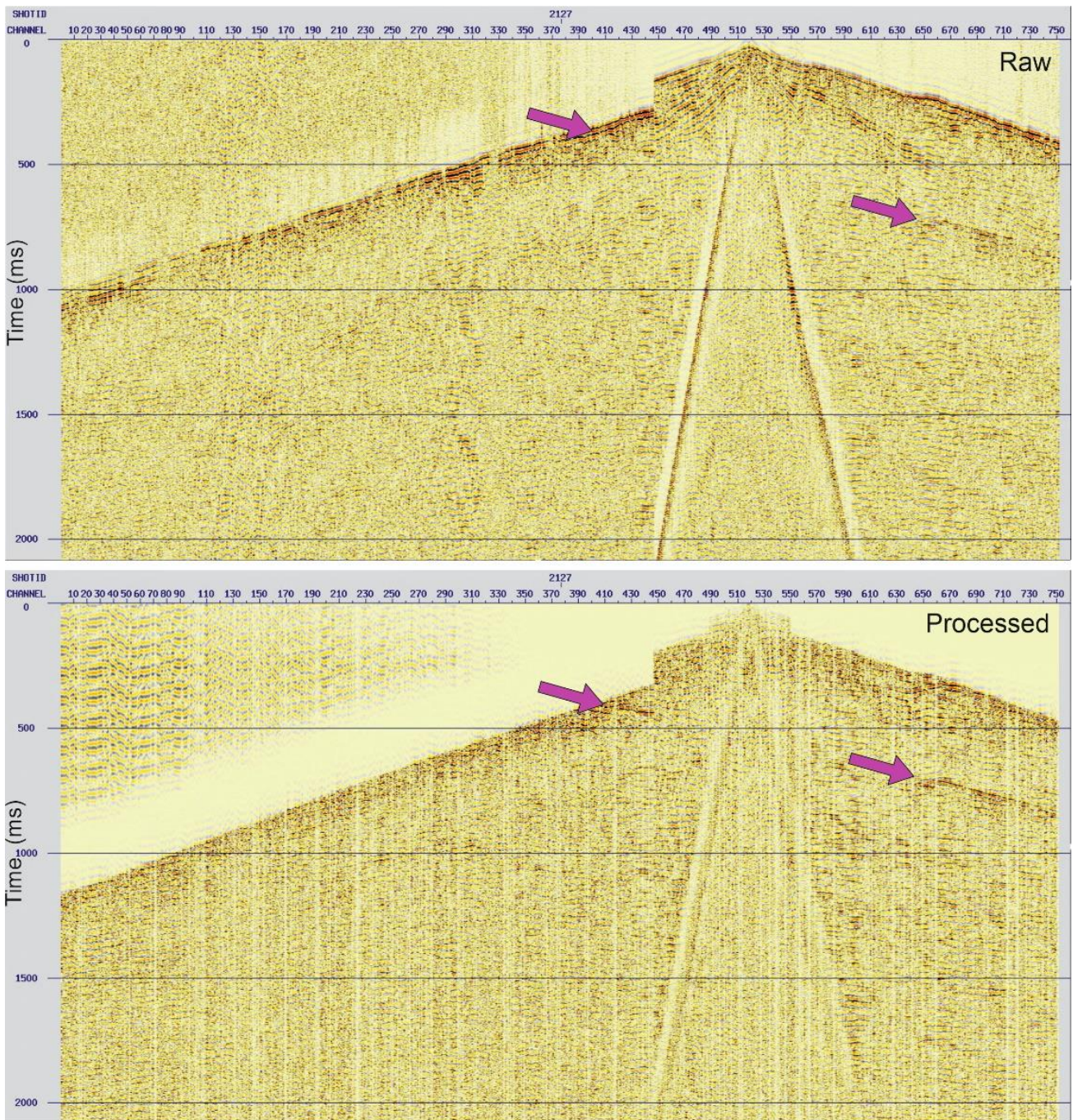
Figure 12. An example of a shot gather: raw data (top) and fully processed data (bottom). Note how the dipping reflector (marked by arrows) is enhanced.

Final stacks in the time domain are presented in Figures 13 and 14. Note the rich sub-horizontal reflectivity and a prominent dipping reflector around CDP 950.
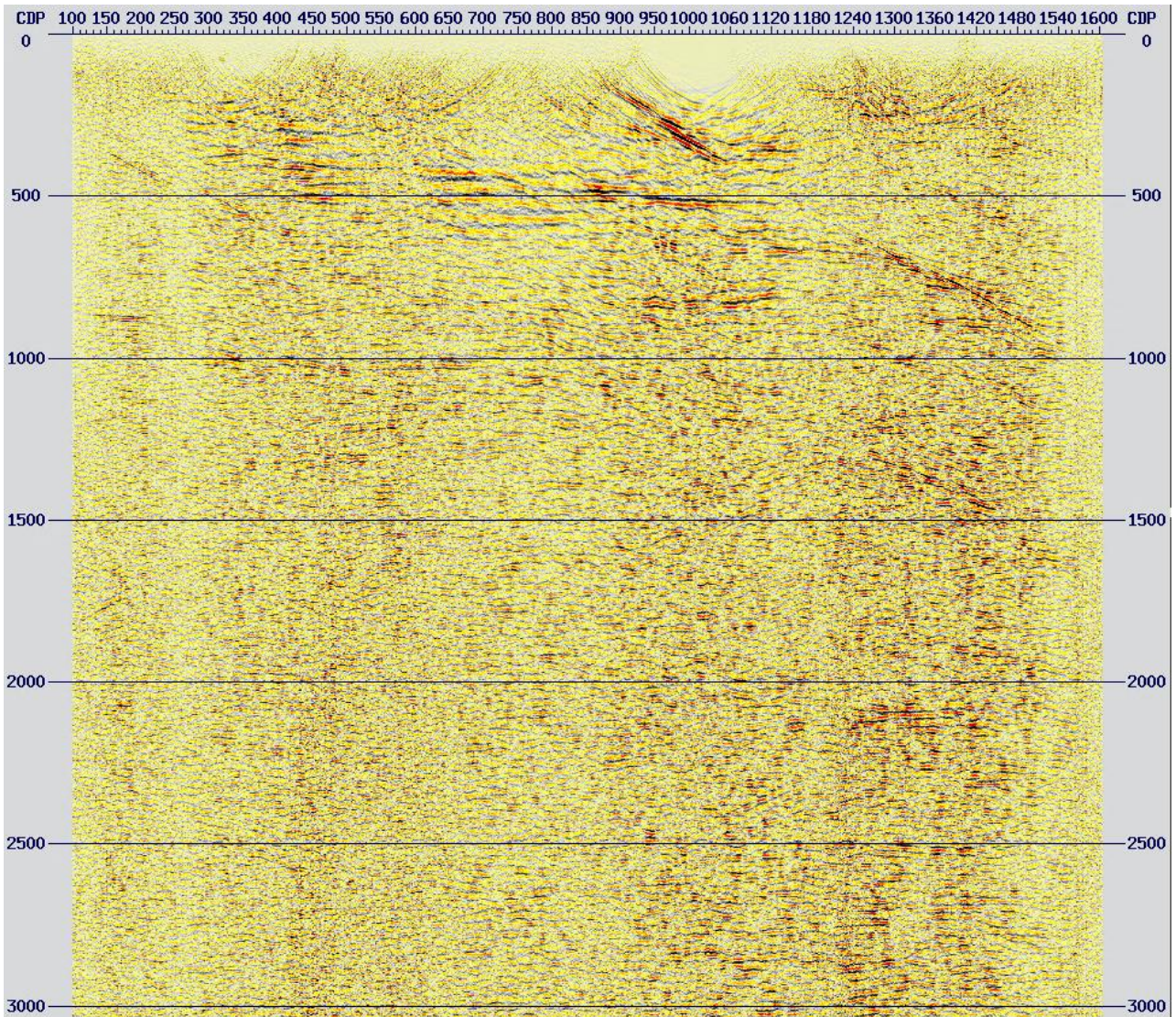
Figure 13. The final DMO stack along the KOSE2022 profile. Vertical scale in milliseconds. 1000 ms translates to ca. 3000 m depth. CDP points increase towards NNE.
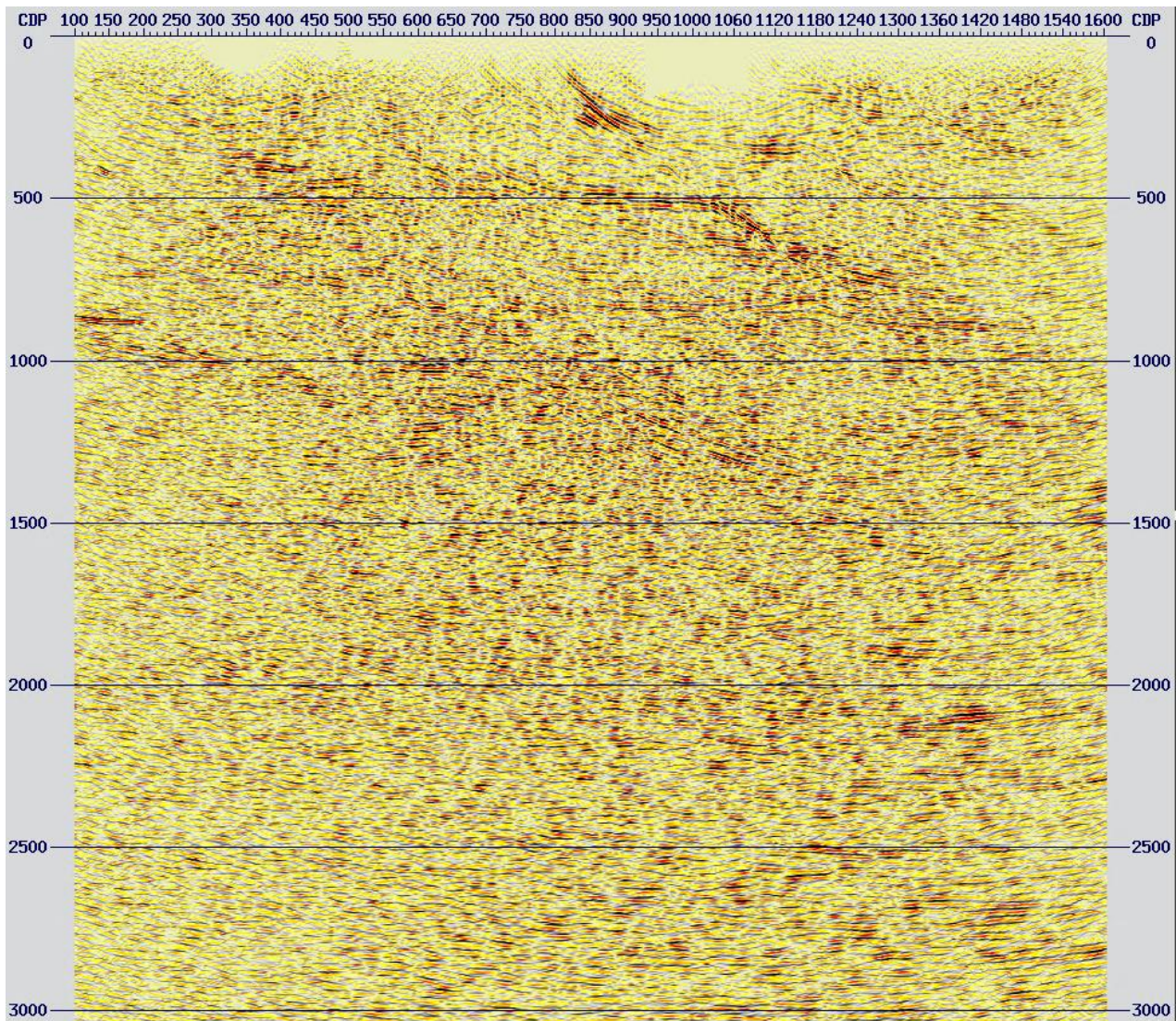
Figure 14. The final post-DMO migrated stack along the KOSE2022 profile. Vertical scale in milliseconds. 1000 ms translates to ca. 3000 m depth. CDP points increase towards NNE. The migration process moves reflections to their true subsurface positions (provided that the migration velocity model is correct). Reflections are moved up dip and shortened.

The new seismic data are much richer in coherent reflections than the pre-drill seismic data acquired in 2018 (Gislason et al. 2019). The KOSE2018 profile (Figure 15) did not image the top of the intrusion, but it captured some deeper reflectors (R1 and R2). In contrast, the KOSE2022 profile revealed coherent reflections that can be associated with the top and bottom of the intrusion (Top_int and Bot_int in Figure 15). It is interesting to note that the top of the intrusion matches well with the inferred intrusion modelled by T. Karinen based on the density model from 3D gravity inversion (Figure 15). The seismic data provide new constraints on the possible bottom of the intrusion (ca. 2500 m depth). The origin of the steeply dipping reflector marked D1 is unknown. Its surface projection matches a weak magnetic anomaly (Figure 15) and could therefore be tentatively interpreted as a dyke.
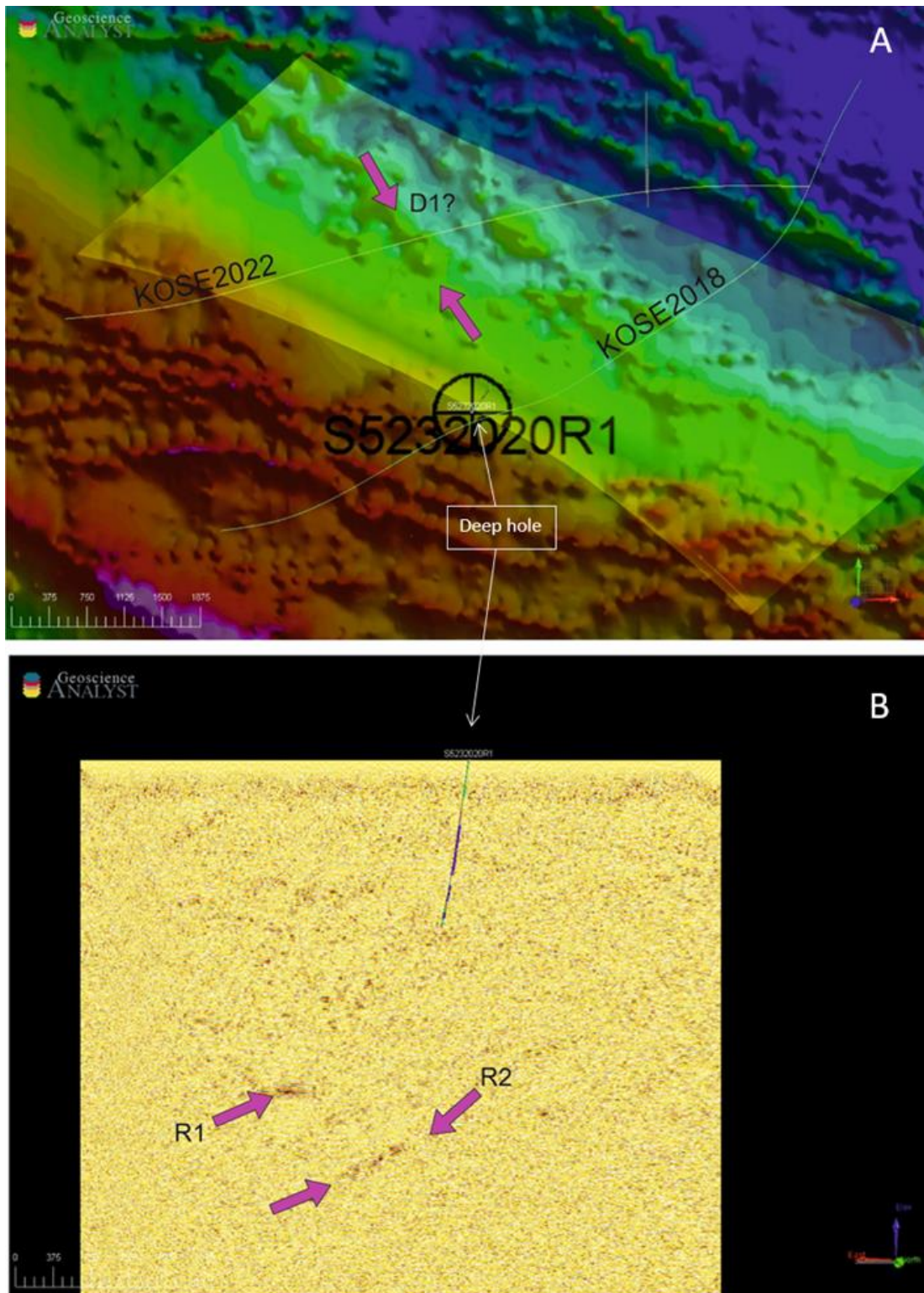
Figure 15. (A) Map view of the KOSE2018 and KOSE2022 seismic profiles together with an RTP magnetic anomaly map. The modelled Koillismaa intrusion (after T. Karinen) is also shown. The arrow points to a magnetic anomaly associated with the reflection D1 seen in the new data (Figure 15). (B) The KOSE2018 seismic section, looking south. Reflectors R1 and R2 were the most prominent features.
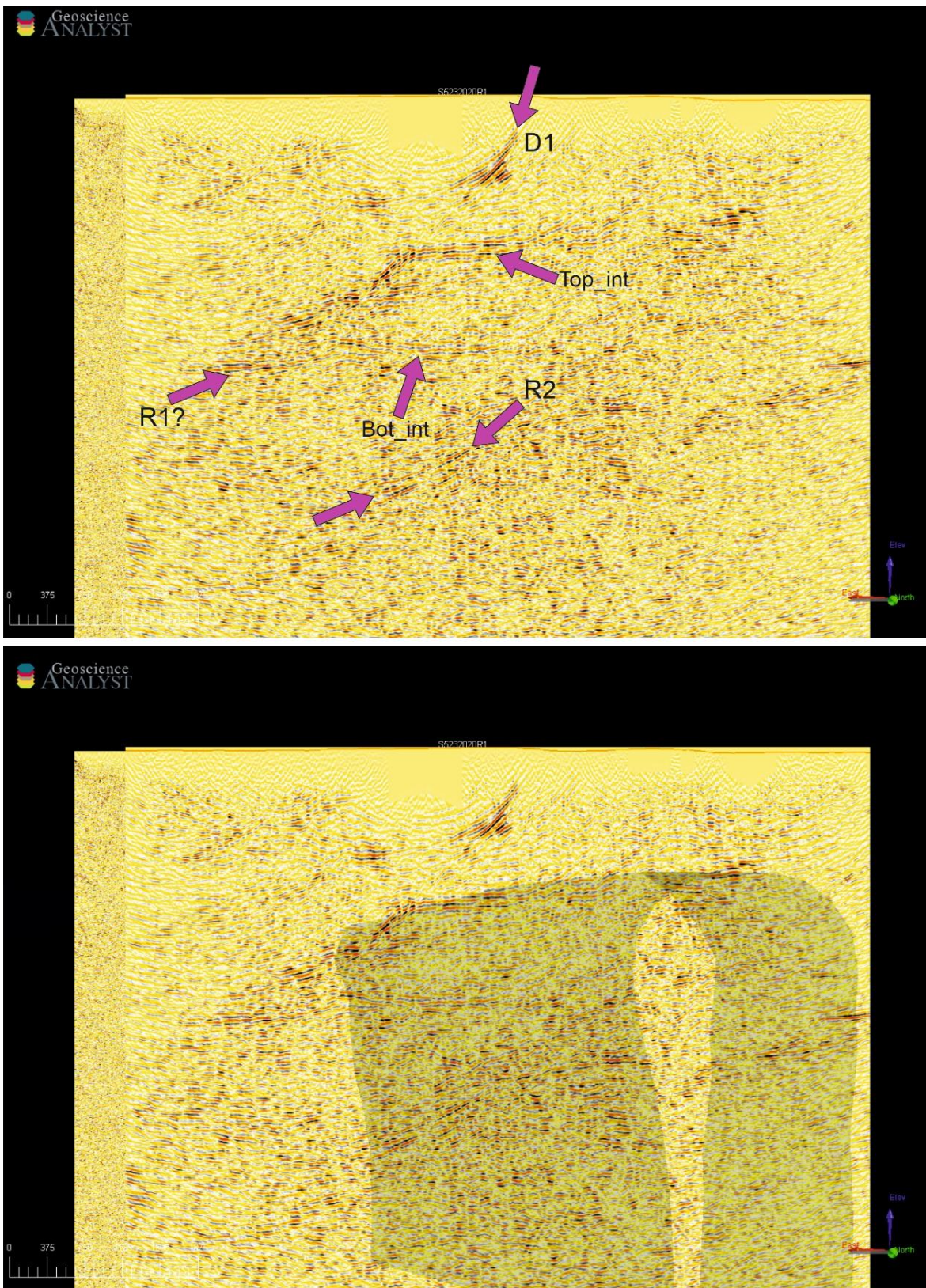
Figure 16. The KOSE2022 final seismic section (top). The arrows point to the reflections discussed in the text. Seismic data overlayed with the modelled Koillismaa intrusion (from T. Karinen) (bottom). Looking south.

4.4.2.2 Distributed acoustic sensing vertical seismic profiling

Distributed acoustic sensing (DAS) is a relatively new tool in several geophysical applications (see recent overview by Li et al. 2022). It allows the recording of seismic signals along tens of kilometres, along fibre-optic cables based on the principle of light backscattering. Most DAS applications so far have focused on downhole measurements, especially vertical seismic profiles (VSP). The main motivation for testing DAS VSP in the Koillismaa drillhole was related to the fact that due to the numerous fracture zones, using a conventional borehole geophone tool for acquiring VSP was too risky.

VSP measurements were performed simultaneously with the surface seismic acquisition. We used a fibre-optic cable manufactured by Solifos (BRUsens DTS) armoured with a stainless-steel loose tube. The cable hosts two multi-mode and two single-mode optical fibres. The cable was deployed using a dummy and reached a maximum depth of ca. 1140 m, which was still deeper than the wireline logging, reaching ca. 1045 m depth. After some testing, it was concluded that a cable under tension provides a better signal-to-noise ratio. For the actual DAS measurements, we used an ASN OptoDAS interrogator provided by NORSAR. During the acquisition, we tested various gauge lengths (GL) (5, 10, 15 m) with different energy sources (Vibroseis and dynamite) and finally used 10 m GL for the dynamite shots and 15 m GL for Vibroseis. DAS channel spacing was set to 1 m. During the acquisition, we noted that the maximum distance at which we observed a seismic signal was ca. 1.5 km. Eventually, we recorded about 90 sources with clear seismic energy (Figure 17).
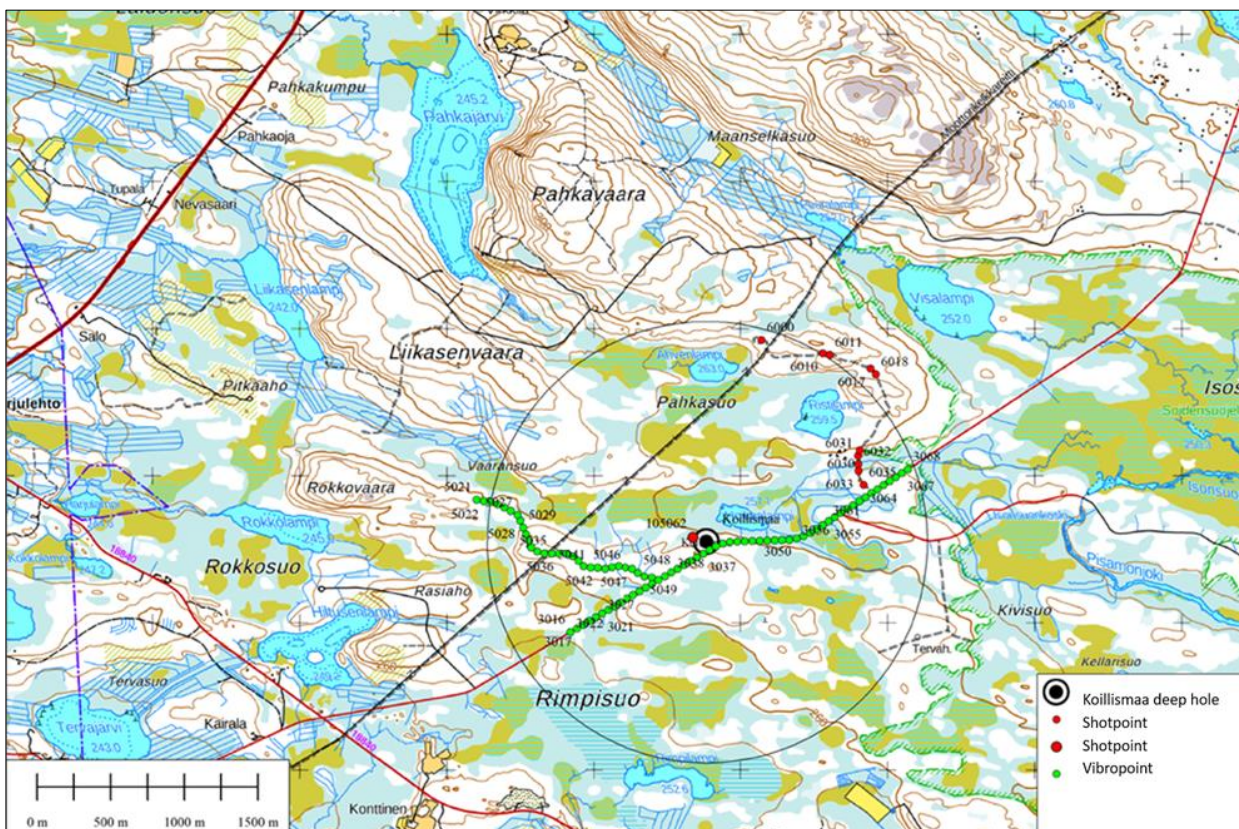

Figure 17. A basemap showing shot points recorded by the DAS system. The circle with a radius of 1.5 km is centred on the Koillismaa borehole.

The data quality is good on average (see an example offset shot gather in Figure 18 a). We can see clear P-wave down-going energy, as well as the S-wave arrivals (which are attenuated beyond the cemented portion of the borehole at > ca. 900 m depth) and some upgoing energy in the raw data. Even though the dynamite records resulted in a very broad band response (300–400 Hz), the data quality was far inferior to Vibroseis shots, which we attribute to the small charges and shot depths.

Prior to imaging, offset Vibroseis shots were processed using standard tools: integration along the time axis to obtain geophone-like records, median filtering to remove down-going waves, bandpass filtering, coherency enhancement of upgoing energy and muting of first arrivals (see an example of a processed gather in Figure 18 b). Data were then migrated using Kirchhoff pre-stack depth migration code into a 1470 x 560 x 2000 m (crossline x inline x depth) volume with a constant velocity of 6000 m/s.
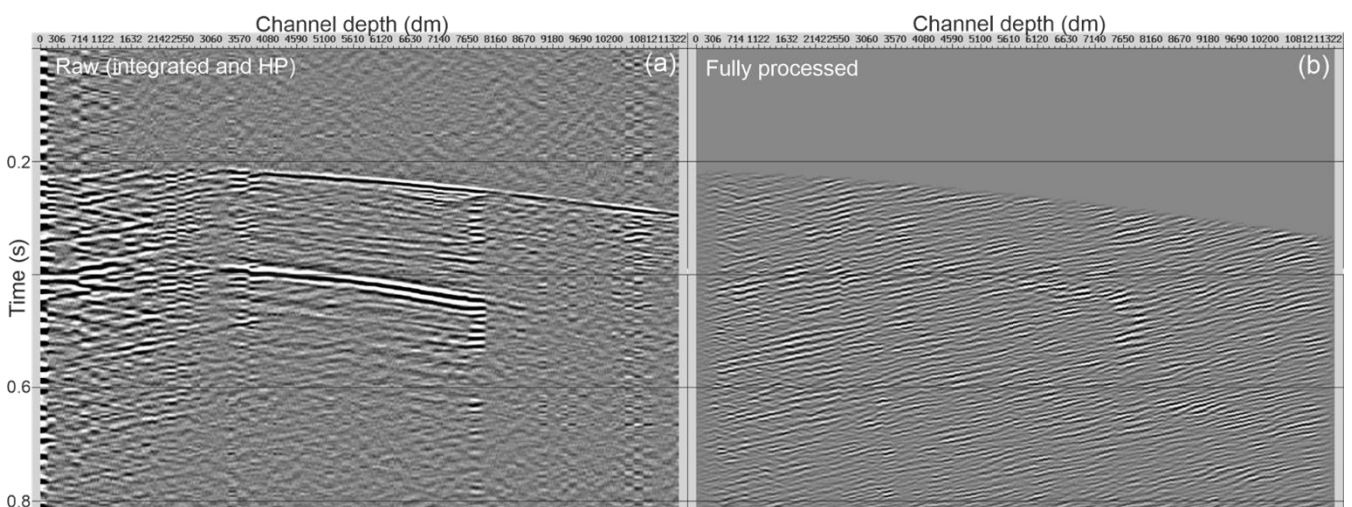

Figure 18. Example of a Vibroseis shot gather recorded in the Koillismaa drillhole: (a) raw, (b) fully processed. The shot is located ca. 1 km from the drillhole collar.

First, we analysed the zero-offset shot records. We followed a standard zero-offset VSP processing and down/up-going wavefield separation by median filtering. Figure 19 displays a comparison of a logging-based acoustic impedance plot with the two-way time-shifted upgoing wavefield from the Vibroseis shot. We can note the correlation of the reflections marked by arrows with the changes in lithology/rock properties.
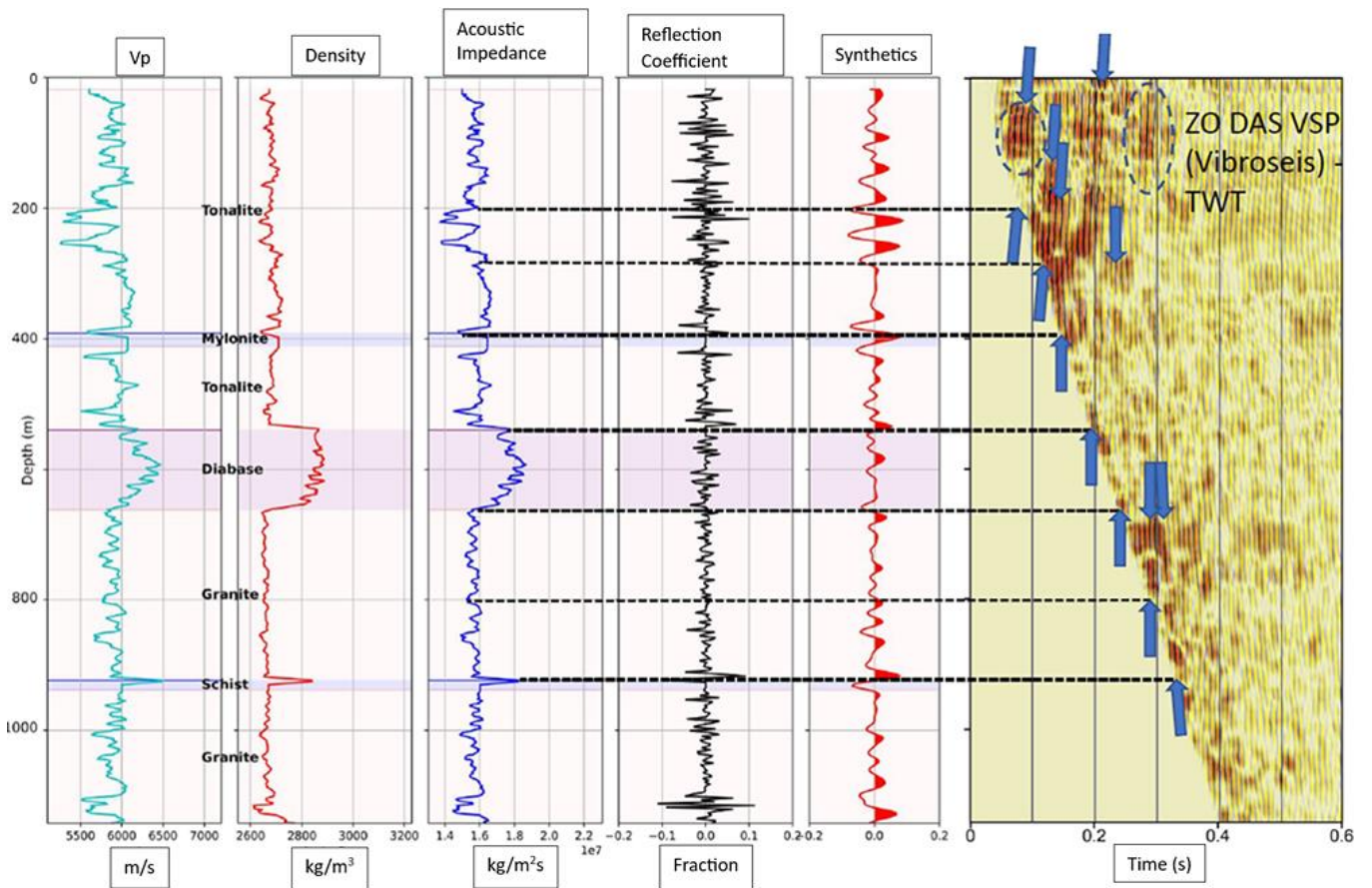
Figure 19. P-wave velocities and densities from the laboratory measurements on the core samples from the Koillismaa drillhole (Heinonen et al. 2022) and the derived properties (acoustic impedance, reflection coefficient and synthetic seismogram) vs a processed zero-offset VSP section from a Vibroseis shot point (shifted to a two-way time).

Some of the reflections identified in the zero-offset VSP section might also be related to fracture zones, as indicated in Figure 20, in which the VSP data are compared with full-waveform sonic data.
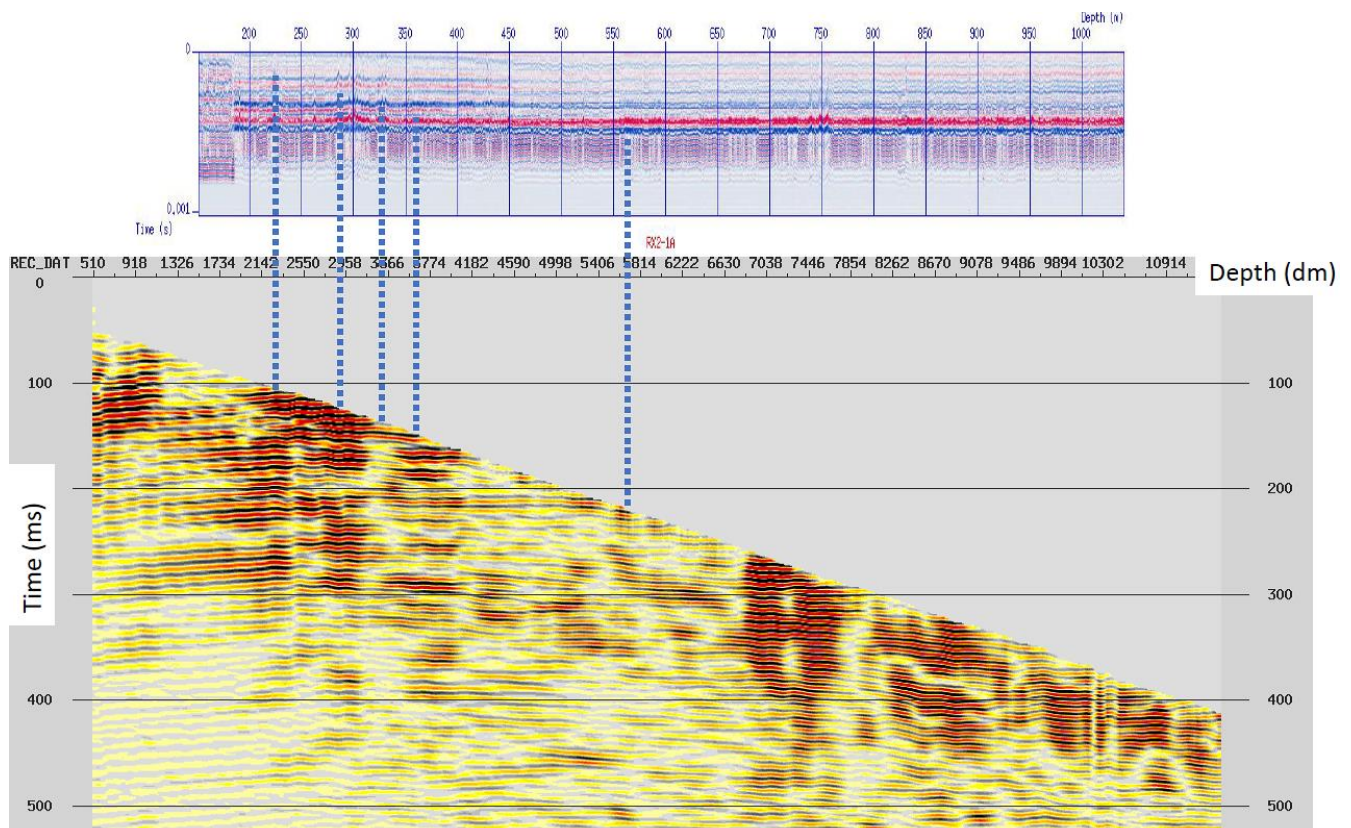
Figure 20. A processed Vibroseis zero-offset VSP section and a plot of the full-waveform sonic data (mid-receiver), indicating possible correlations between reflectivity and fracture zones (identified as diming of the amplitudes).

Figure 21 presents a comparison of surface seismic data (KOSE2018 profile, Gislason et al. 2019) acquired prior to drilling with the inline extracted from the migrated DAS-VSP volume. The KOSE2018 profile imaged reflector correlating with the schist (altered diabase) or major open fracture beneath this contact as intersected by the Koillismaa drillhole (marked F1). Otherwise, reflectivity is increased below the extent of the drillhole and probably represents the intrusion. The same feature (F1) is also observed in the DAS VSP section (Figure 21 b). Below event F1, we additionally observe reflection F2, which probably corresponds to other fractures identified in the borehole image log (1016–1021 m). Some other reflections could be linked with changes in lithology: D1 marks the contact of thick diabase dyke with the granite. L1 probably originates from the diorite–granite contact. The latter is found below the extent of the fibre-optic cable. The interval of the Koillismaa intrusion is characterised by increased reflectivity in the DAS-VSP section, which is compatible with the changes in lithology (pyroxenite, peridotite, gabbronorite and granite dykes).
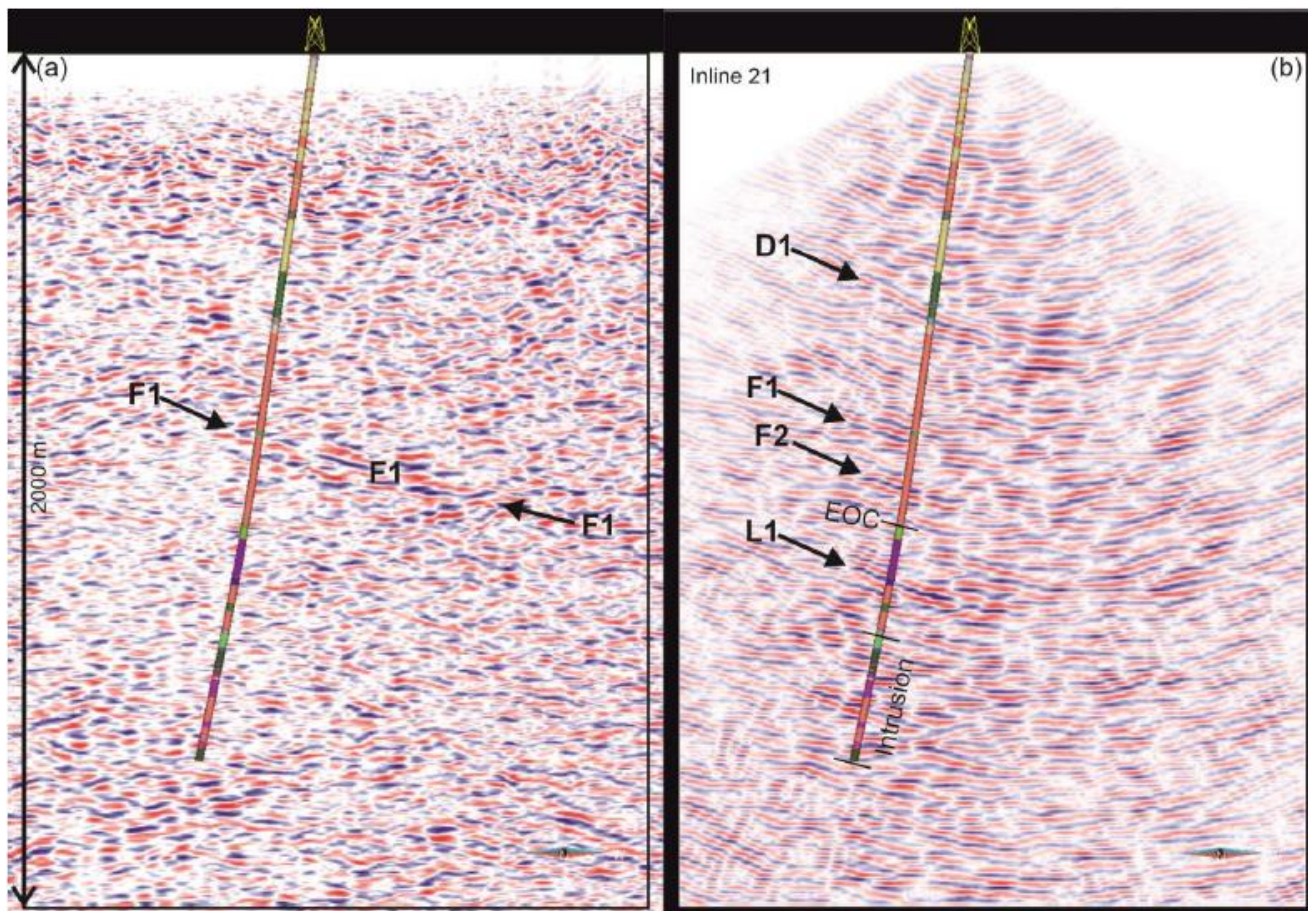
Figure 21. Part of the KOSE2018 seismic profile (Gislason et al. 2019) with the projected Koillismaa drillhole path and lithology log (a). Inline from the migrated DAS-VSP volume (b). View from the north. Marked events are discussed in the text. EOC = end of cable.

4.4.3   Audiomagnetotelluric (AMT) studies

In 2019, before the Koillismaa Deep Hole project, a sparse audiomagnetotelluric (AMT) profile consisting of four sites was measured across the Koillismaa gravity anomaly (Figure 22). These original data appeared anomalous, and the derived 2D inversion model included a feature more conducting than its surroundings at depth, which was thought to be related to the mafic dyke, i.e., the source of the gravity anomaly. It turns out, however, that the new and much larger AMT data set (Figure 22) acquired in 2022 complicates the original interpretation. The data cannot be explained by a single conductive body at depth; rather, the AMT data appear to indicate anomalous conductivity even in areas outside of the gravity anomaly. Furthermore, it is doubtful whether the mafic dyke itself is conductive at all or whether the anomalous conductivity arises from some other parts of the bedrock instead.

AMT data from 70 new sites were acquired in 2022 (Figure 22). Denser site spacing was used near the deep hole, where controlled source EM data were also acquired using the same receivers (see section 4.4.4). The distribution of sites is such that both 2D and 3D modelling could be performed.

ADU08e data loggers were used together with MFS-07e induction coils and nonpolarizing electrodes (50–100 m dipole size). Two-, 4- and 5-channel setups were used, where the 2-channel setup only measures horizontal electric fields and requires simultaneous horizontal magnetic field recording from a nearby 4- or 5-channel site to process the data. In the 5-channel setup, the vertical magnetic field is also measured so that the tipper transfer function can be extracted. Overnight recordings were made so that high-quality data in the period range of ca. 0.0039–100 s (256–0.01 Hz) could be obtained. Matlab-based GTK inhouse processing code was used, which uses a standard M-estimate algorithm. Remote reference data from a site located in Tiskivaara, Rovaniemi, were mostly available. For some sites, fixed remote reference data were not available due to technical issues, but in such cases, 'local' remote reference data from the measurement area could be used, since two sites equipped with induction coils were typically recording simultaneously.

The most prominent feature in the whole AMT data set is a phase split between the TE and TM modes in the period range 0.01–1 s. An example sounding curve is presented in Figure 23. Phase tensor ellipses for one period from the AMT data are displayed in Figure 22 and for all periods as a pseudo section in Figure 24. The orientation of the ellipses represents the geoelectric strike, and it matches well with the direction of the gravity and magnetic anomalies (Figure 22). 3D effects in the data are relatively small, indicated by the low phase tensor skew (β) values. A summarized estimation of a geoelectric strike is presented in Figure 25. It shows a clearly defined geoelectrical strike angle for periods between 0.001 s (1000 Hz) and 1 s (1 Hz). For the lowest periods (0.001–0.1 s), the strike is -60° and changes to -35° between 0.1–1 s.
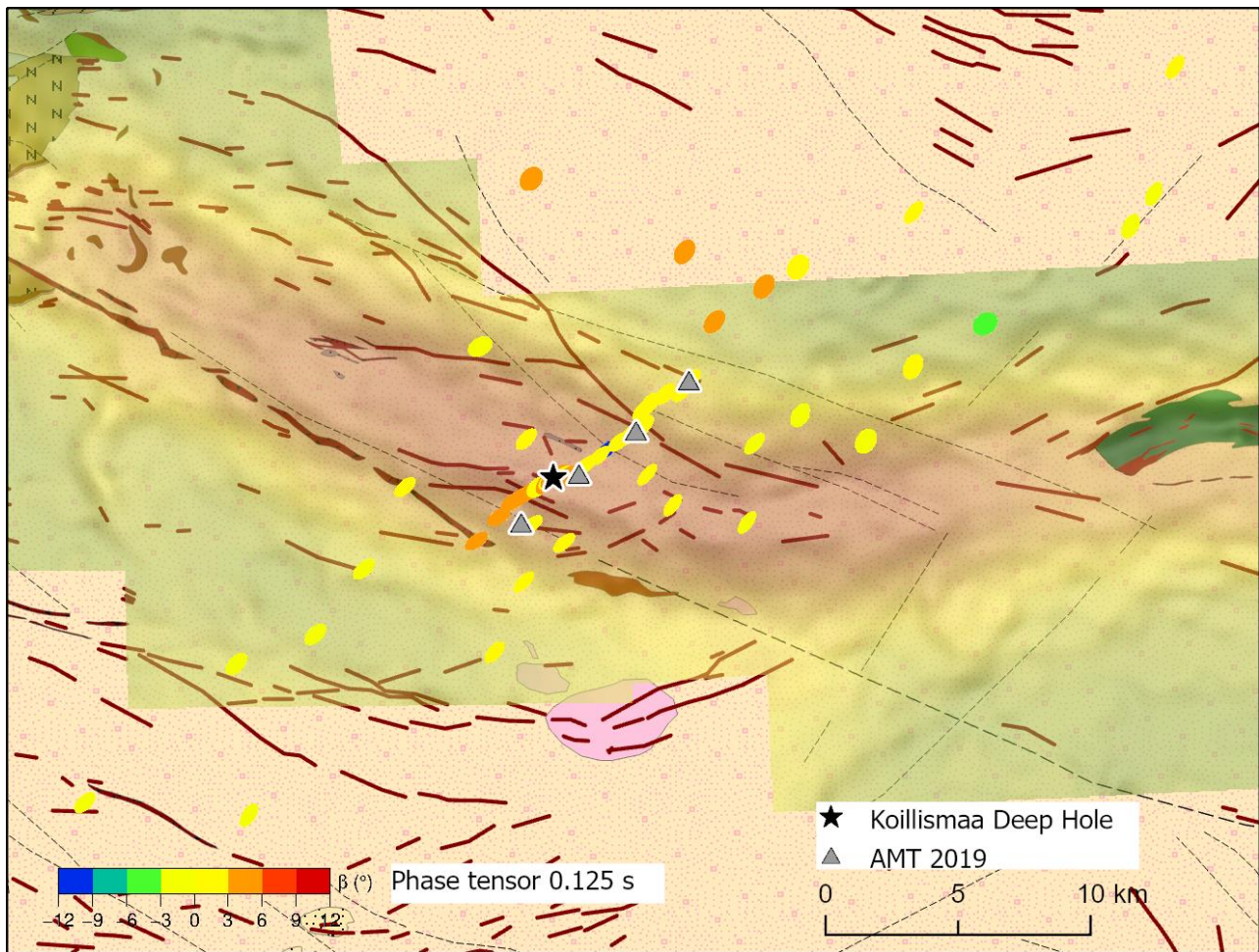
Figure 22. Phase tensor ellipses from the 2022 survey shown at each AMT site in the period of 0.125 s. The geoelectric strike is interpreted as the common direction of the ellipse minor axes, matching with the direction of the gravity anomaly shown in the background on the geological map. Ellipse colours represent the strength of 3D effects in the data. Low values (yellow) indicate minor 3D effects. Grey triangles denote 2019 AMT site locations. The black star marks the location of the deep hole.

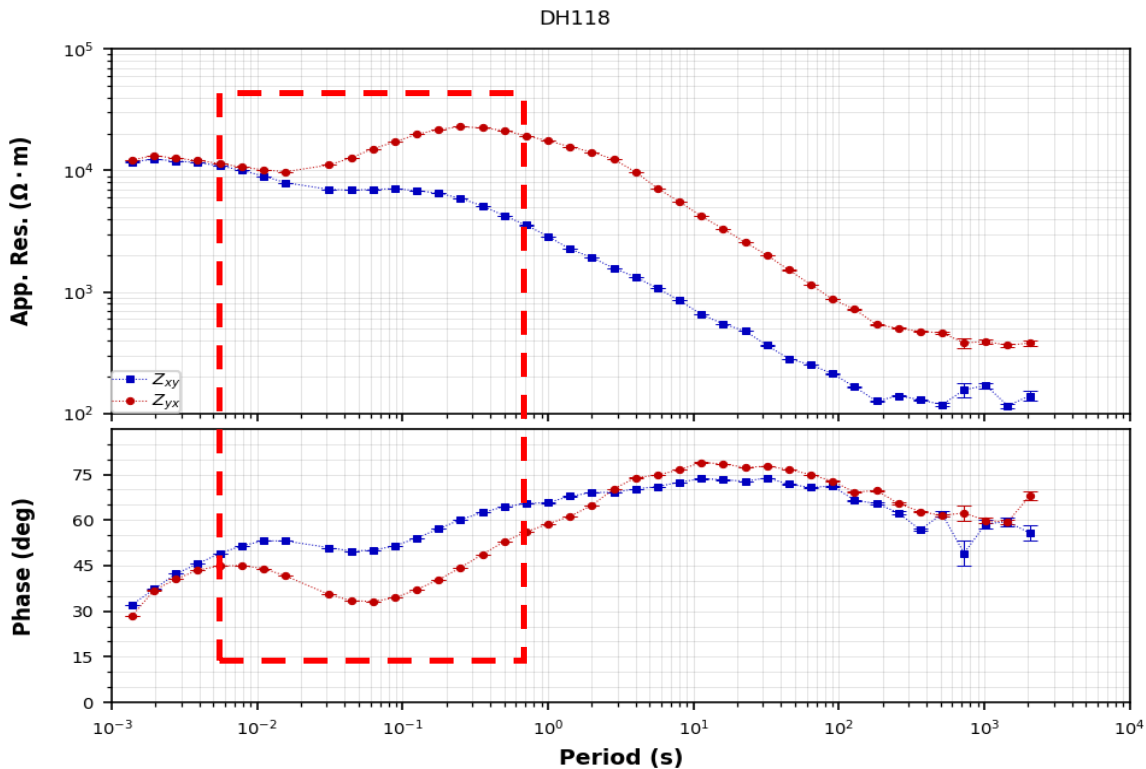**Figure 23.** A typical AMT sounding curve from the deep hole area (Site DH118, located 100 m from the deep hole). The red rectangle emphasizes the period range of the anomalous data, i.e., the phase split between the TE (blue) and TM (red) modes (data rotation 45°).

We used different modelling and inversion software to obtain 2D and 3D conductivity models. 2D models were obtained using WinGLink (Rodi and Mackie, 2001) and Mare2DEM (Key, 2016). For 3D inversions, we used the open-source finite difference modelling and inversion software ModEM (Kelbert et al., 2014). Modelling of the AMT data has proven challenging, despite the relatively simple data behaviour. It is easy to find various models that agree equally well with the measured data. 2D inversions tend to produce models with multiple parallel conductive features separated by resistive parts. However, the horizontal locations of the conductive features vary between different inversion models, and the features are therefore not well resolved by the AMT data. The depths to the top of the conductive features range from one to a few kilometres. 3D inversions lead to somewhat similar results, and obtaining a stable 3D inversion model has been equally challenging, partially due to the highly irregular station layout and lack of aperture in data coverage in the NW–SE direction. One possible 3D result is presented in Figure 26. Here, we describe the main stable features. It generally shows a very resistive environment (more than 10 000 Ωm) in the upper 2 km. This is followed by a more conductive zone between 2–4 km depth and again a more resistive zone below. At the location of the deep hole and hence the ultramafic intrusion, the conductive zone is cut by a resistive anomaly. This contradicts the results from the 2019 sparse AMT survey. The strike of the resistive anomaly correlates with the strike analysis and the orientation of main geological structures and faults in the area. Figure 26 illustrates that the flanks of the resistive anomaly (marked by the red box) are bounded on both sides by more conductive structures. The southern conductor correlates with the maximum on the aeromagnetic map.

The exact source for the anomalous AMT data in the deep hole area is currently not well understood. The data set displays consistent behaviour over the whole area, with phase split between the TE and TM modes, and the geoelectric strike matches with the direction of the gravity anomaly and the main trends in the surrounding bedrock (Figure 22). One explanation for the 3D inversion model presented in Figure 26 may be that the ultramafic rocks intruded into a pre-existing conductive structure, and its core is now indicated by the resistive structure. It is known that serpentinization may lead to elevated conductivities (e.g., Falcon-Suarez et al. 2017). Conductive serpentinite rocks are known from Näränkävaara. Thus, it could be speculated whether the conductive flanks of the resistive intrusion may be caused by serpentinization of the ultramafic rocks. This could also explain the offset in magnetic maximum compared to the gravity. However, it is emphasized that, without further evidence, any particular resistivity model should be viewed with some scepticism, since several different models explaining the measured AMT data equally well have been found. Furthermore, it cannot even be ruled out that the anomalous AMT data could originate from widespread (possibly deeper) electrical anisotropy. Based on preliminary analysis, AMT data acquired further north in the BatCircle2.0 project appear to display a very similar anomalous signature to the deep hole AMT data, which could indicate that the observed data behaviour is the result of some larger scale process and not directly related to the Koillismaa intrusion. In the Seems Deep project, extensive EM and seismic measurements were completed in the deep hole area in 2023, and it is hoped that combining all the data will lead to a more conclusive model and interpretation.
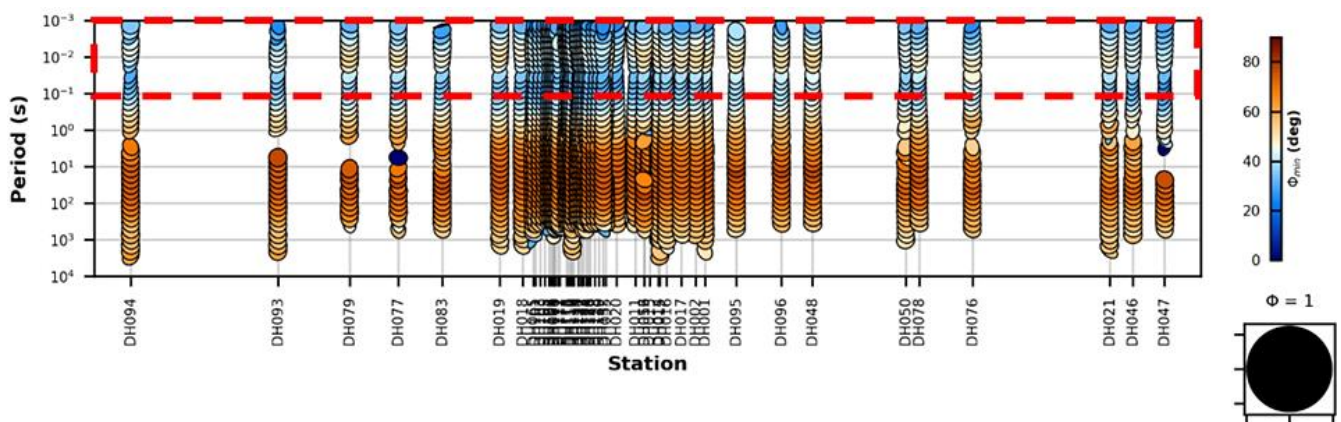

Figure 24. Phase tensor ellipses of the measured AMT sites shown as a pseudo section. The red rectangle indicates the anomalous period range.
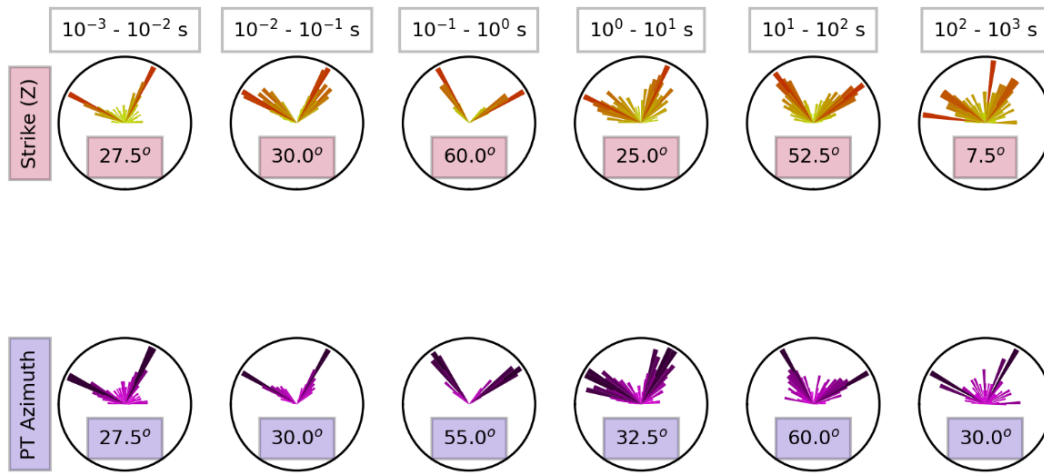
Figure 25. Geoelectric strike analysis for all sites for different period (and thus depth) ranges. Note the 90° ambiguity.
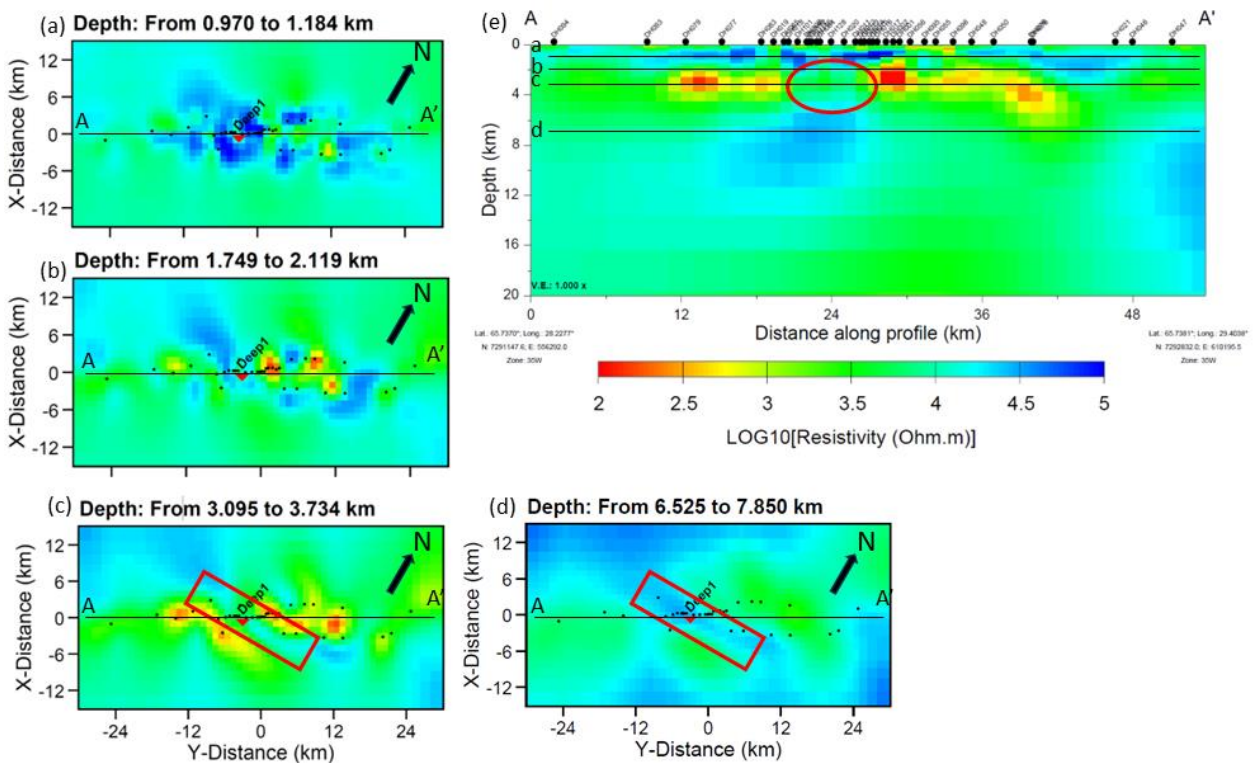
Figure 26. Horizontal and vertical slices through a 3D inversion model. (a–d) Depth slices at different depths. Depths are indicated by black lines in e. The red rectangle shows the location and orientation of the main anomaly correlating with the location and orientation of the gravity maximum. (e) A vertical slice along the main profile. The location is marked by a black line in a–d. The red ellipse indicates the location of the Deep A hole and ultramafic intrusion. Note: The main profile direction is not in an E–W direction, but for numerical reasons, the modelling grid has been rotated by 30°.

4.4.4 Controlled source EM experiment

Partially overlapping with the AMT work, a controlled source EM experiment was conducted in September 2022 (Figure 27). This was the first field test using the Phoenix TXU-30A electromagnetic transmitter acquired by GTK in 2020. The high-power (20 kW) transmitter enables investigation to a depth of up to a few kilometres. While there are a range of possibilities, the operation mode of this test was to improve AMT (natural source) data quality using the strong signal generated by the transmitter (artificial source) in the period range of the so-called AMT dead band (ca. 1–10 kHz). Such a method is called controlled-source AMT (CSAMT). Data processing and modelling tools needed for controlled source measurements are also being developed within GTK (Geke2 project).
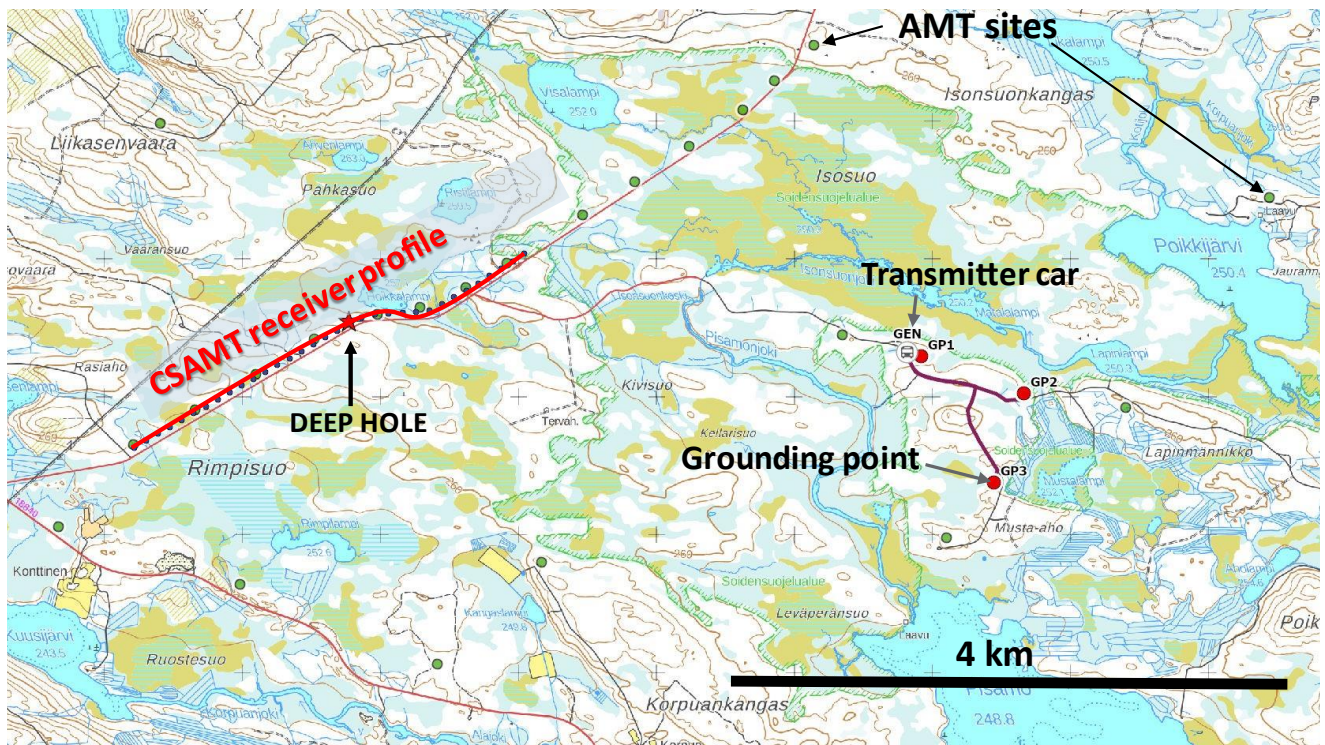

Figure 27. The transmitter and receiver layout of the CSAMT experiment. The receiver part consists of 27 AMT receivers installed along a profile (red line) crossing the deep hole location. The site spacing is ca. 100 m. The transmitter is offset from the receiver line by ca. 4 kilometres and consists of two separate transmitter dipoles (GP1–GP2 and GP1–GP3).

A schematic of the transmitter gear is presented in Figure 28. The instrumentation consists of the transmitter and a transformer installed in a van, a power supply (a generator) and transmitter cable lines connected to grounding points. The grounding points are located on swamps to ensure good electrical coupling. Good grounding is achieved by several steel rods pushed into the swamp. In the test, a grounding resistance of 170 Ω was achieved, which allowed ca. 6 A to be injected into the ground using the maximum transmitter voltage of 1000 V. Due to the high voltage, electrical safety must be considered. For example, the grounding points were guarded and fenced with high-visibility tape and warning signs.
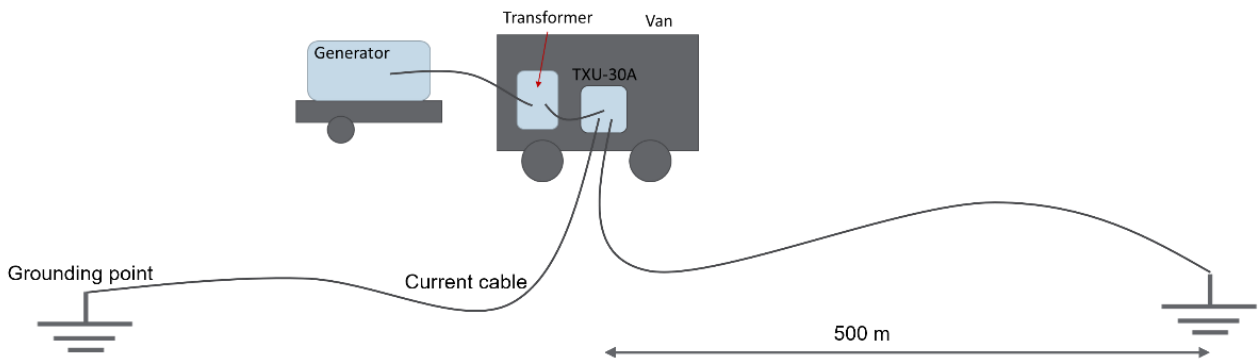
Figure 28. Schematic diagram of the transmitter components and typical configuration during field work employing a grounded source.

Figure 29 presents an example of the acquired CSAMT data compared with AMT data from the same receiver location (southernmost site on the CSAMT profile, see Figure 27). It is observed that the controlled source CSAMT data (black) are of better quality compared to the natural source AMT (red) at high frequencies, especially within the AMT dead band. This was therefore a successful demonstration that CSAMT can be used to extend the usable frequency range of AMT. Towards the low frequency end of the CSAMT data, however, the so-called source effect is noticeable, as the CSAMT data deviate from the AMT data. To prevent this, the transmitter should be installed even further away from the receiver site to ensure the plane wave condition.

Figure 29. Apparent resistivity (top) and impedance phase compared from AMT (red and blue) and CSAMT (black) surveys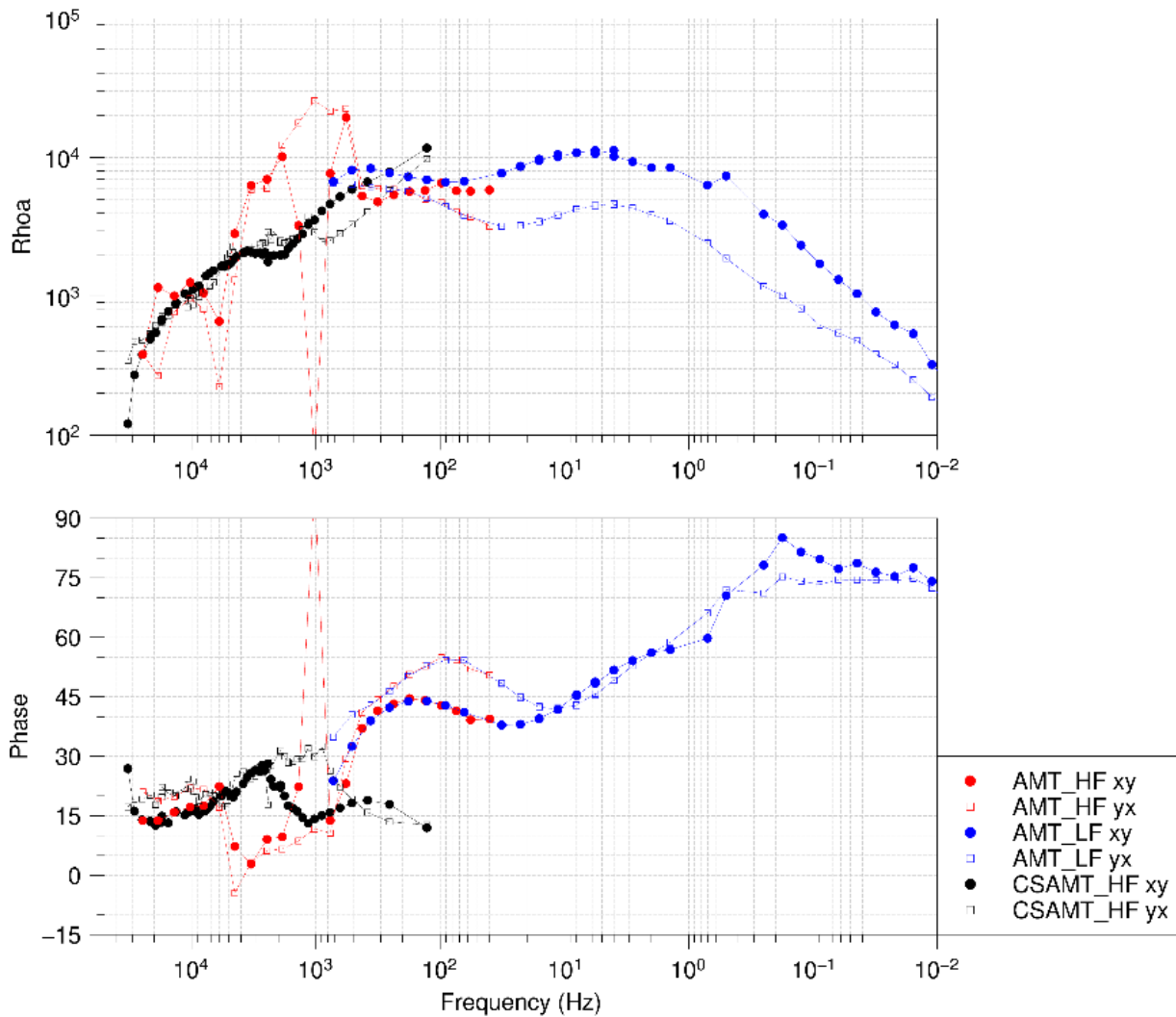. The CSAMT data are of considerably higher quality compared to the high frequency part of the AMT data, which are typically of low quality in the AMT dead band (ca. 1–10 kHz). A source effect is evident at the low frequency end of the CSAMT data, where they deviate from the AMT data.

4.5   Geothermal energy studies

Exploring deep geothermal resources in crystalline settings offers a promising solution for near-unlimited clean energy across multiple spheres of our society, including direct space heating, industrial applications, and electricity generation. However, geothermal exploration in deep crystalline settings presents unique challenges, particularly due to the typically low porosity and low permeability of crystalline rocks.

In this study, a novel perspective on the formation of crystalline reservoirs was presented, shedding light on the interplay between brittle deformation and mineral alteration mechanisms that shape the pore network of granitic rocks. This work did not aim to address the challenges associated with the development of Hot Dry Rock (HDR) reservoirs, or the complex thermo-mechanical aspects of

enhanced geothermal systems (EGS), which have been extensively discussed in previous studies (e.g., Brown et al. 1999; Breede et al. 2013; Jolie et al. 2021; Frey et al. 2022; Kukkonen et al. 2023). Instead, we focused on laying out critical geological processes that will enable the identification of novel opportunities for geothermal exploration in deep crystalline settings, particularly in challenging low-enthalpy areas where volcanic and rifting activity is absent. Furthermore, this study assessed the permeability variation of a suite of granitic reservoirs under increasing confining pressure, providing insights into their suitability as deep geothermal targets. Ultimately, these findings will help to expand geothermal energy exploration and production in crystalline settings worldwide, contributing significantly to our ongoing transition to cleaner and more reliable energy resources.

Geothermal energy studies on cores from the Koillismaa deep hole were conducted from December 2021 to October 2023 and are presented here in three parts: (i) reservoir and thermal assessment of drill core samples, aiming at the geothermal characterization of crystalline rocks perforated by the Koillismaa Deep Hole, (ii) *in situ* geothermal assessment, measuring the thermal properties of the bedrock at the location of the drillhole, and (iii) finite element modelling to test the geothermal performance of diverse reservoir types.

4.5.1   Reservoir and thermal assessment of drill core samples

This study focused on the lower section of the Koillismaa Deep Drillhole, where multiple intervals of granitic and ultramafic rocks are highly fractured. The lowest 472 m section (1250–1722 m) of the drill core was mapped at a centimetre scale, recording information on the texture, structure, composition, and mineral alteration aspects of key rock types. As core recovery was typically above 90%, nearly continuous observation was possible. Thirty-two representative samples were collected from ultramafic and granitic lithologies as full-core samples 50 mm in diameter and with lengths varying from 2–15 cm. Furthermore, petrographic, petrophysical, and mineral analytical characterization was carried out on selected samples, focusing on a subset of 25 granitic samples selected for detailed tests. From this granitic subset, 20 samples were selected for petrophysical tests, 10 for optical microscopy, 8 for micro-XRF analysis and 7 for CT scan imaging (Appendix 3).

The methods used in the work included (i) drill core description, (ii) optical microscopy, (iii) hyperspectral imaging (HSI), (iv) computed tomography (CT) scanning, (v) micro-X-ray fluorescence spectrometry (micro-XRF) and (vi) petrophysical laboratory experiments (i.e., porosity, permeability, density, elastic wave velocity and thermal conductivity). These complementary methods helped us to determine the main petrophysical and thermal trends of crystalline rocks and assess their reservoir performance at progressive depths. This study was published in a peer-reviewed scientific journal (Bischoff et al. 2023).

4.5.1.1   Structural analysis

Regional lineament interpretation was performed using a highly accurate low-altitude airborne LiDAR-based topographical digital elevation model (DEM) collected by the National Land Survey of Finland. GTK processed this high-resolution LiDAR point cloud database into a DEM that represents the bare earth surface, meaning that it does not account for vegetation. The point density for the cloud data was set at 0.5 points per square metre, resulting in an elevation accuracy of 0.3 metres. The interpretation was performed according to procedures defined in Nordbäck et al. (2023). The points were then triangulated to form a terrain surface mesh and subsequently interpolated with the

GTK

natural neighbour algorithm into a 2-metre grid size DEM raster. Lineament interpretation was performed at a single scale of observation with a representative fraction of 1:200.000. This interpretation was used to produce rose diagrams that represent the spatial orientation of regional structures near the drillhole site (Figure 30).
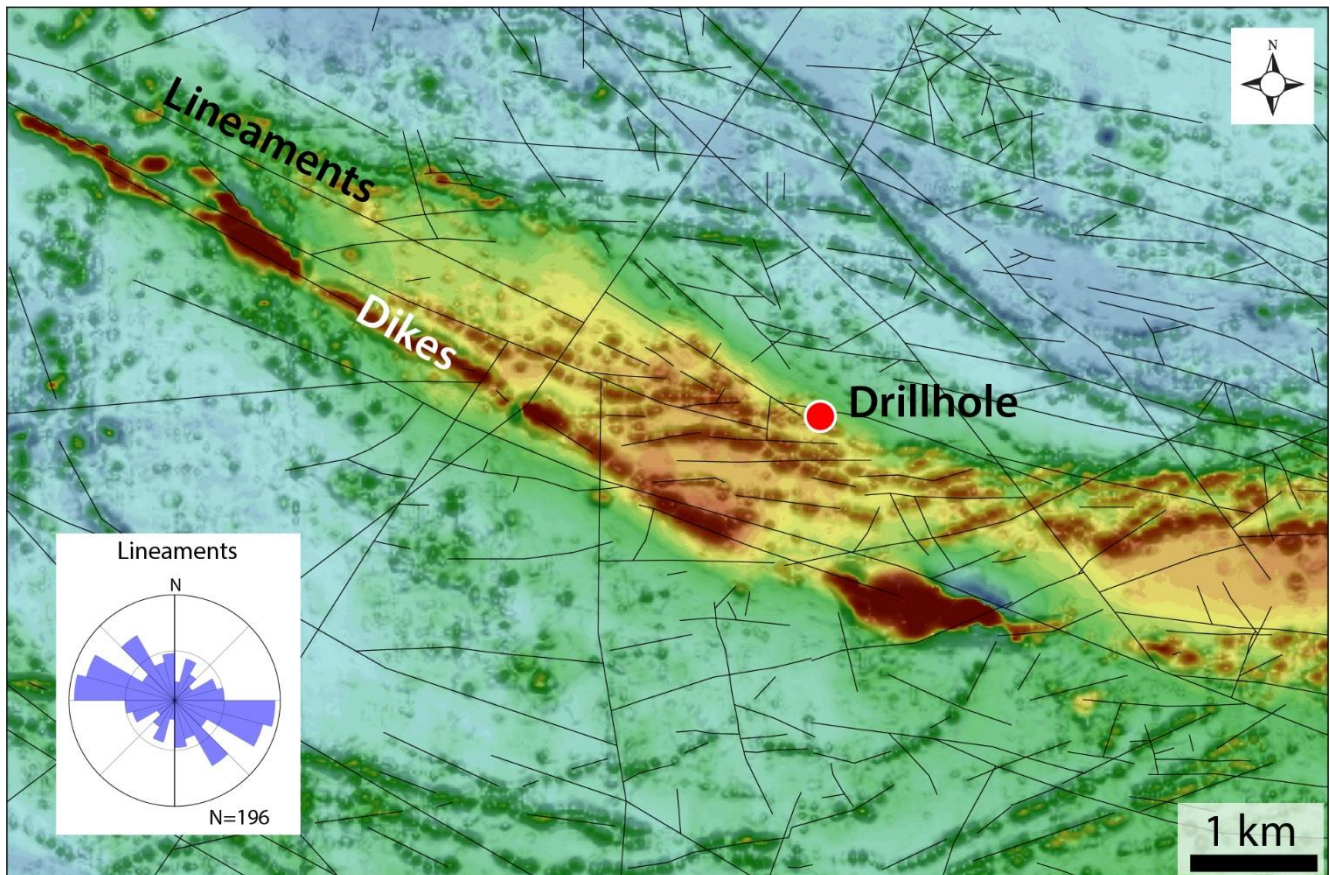

Figure 30. Regional lineament interpretation overprinted on the aeromagnetic map of the studied area. The red dot marks the drillhole location. The rose diagram displays the trend of lineaments in the area.

In addition to regional lineament interpretation, structural data were collected from the oriented core by (i) manual extraction using standard internal core angle measurements and (ii) a Reflex IQ logger device (Figure 31). The handheld Reflex IQ logger measures the orientation of the structures using a laser. Some sections of the core were intensely fractured, making it impossible to obtain a reliable orientation of the core, particularly in the ultramafic interval. Due to this limitation, at certain depths, our drill core observations can only provide an approximation of the main fault trends, which did not impact our first-order structural interpretation across the studied interval.

Rock quality designation (RQD) data were collected from the entire borehole length over 1-m length intervals. RQD data measure the percentage of intact drill core sections of 10 cm or longer, and 100% RQD thus indicates an intact drill core interval. The value provides a simple and efficient way to estimate the overall intactness of the rock, indicating the degree of joints, faults and fractures within the drill core (Figure 34).
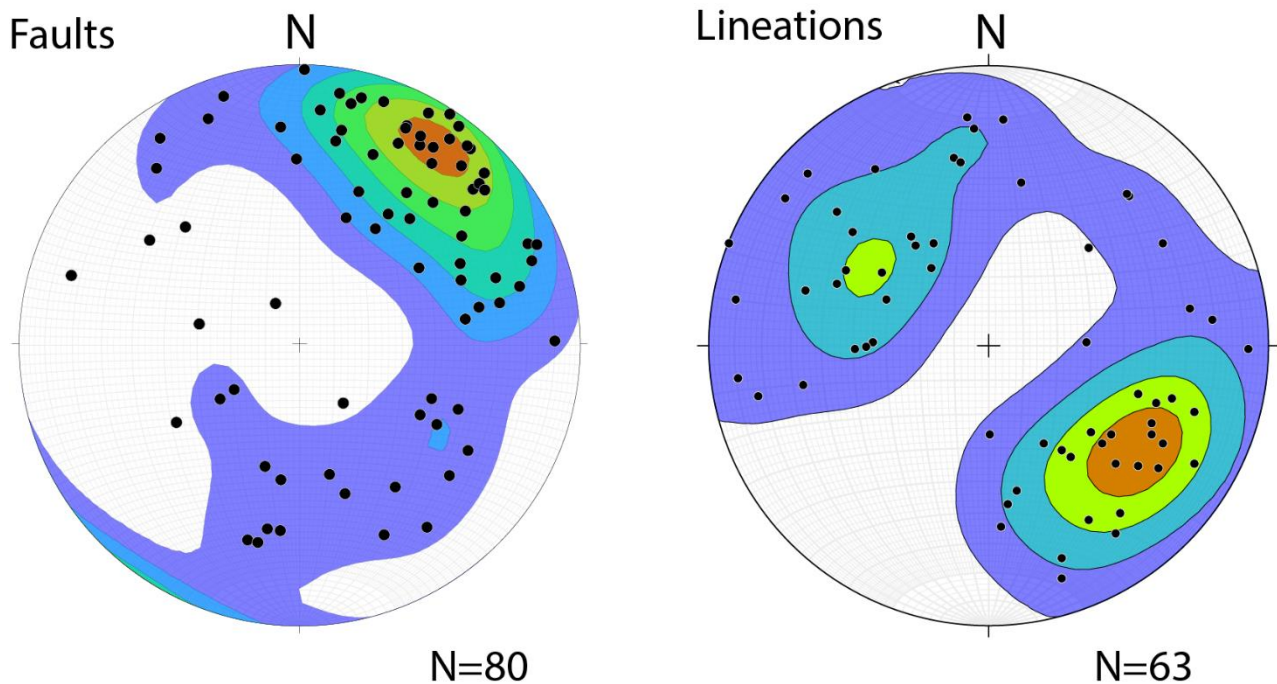
Figure 31. Stereonets showing the pole of plains of faults and lineations identified in the studied interval (1250–1722 m) of the Koillismaa drillhole.

4.5.1.2   Optical microscopy and petrography

Detailed petrographic descriptions were performed, aiming to assess the main mineralogical, textural and structural aspects of representative rock. In addition, key petrographic features, such as mineral shapes and intergrowth, secondary mineral replacement and cataclastic grain-size reduction, helped to identify critical syn- and post-emplacement processes, including the magmatic crystallization series, hydrothermal alteration processes and brittle deformation courses. Seventeen thin sections were prepared at the University of Turku rock laboratory (10 from granites and 7 from ultramafic rocks). The rock samples were immersed in a solvent-free adhesive (Araldite) to avoid rock fragmentation and desegregation during cutting and thin-sectioning preparation. The Araldite adhesive was impregnated with yellow-fluorescent pigment to facilitate the identification and description of diverse pore types. Thin-section descriptions were performed using a Leitz Laborlux 11 POL microscope with 40× maximum amplification coupled with a Euromex VC.3036 Ultra Color camera set to collect high-definition photographs of 3264 × 1836 pixel size.

Optical microscopy also supported the pore morphology characterization of the igneous rocks and their formation processes. The pore morphology classification was adapted and expanded from schemes proposed by Choquette and Pray (1970) and Sruoga and Rubinstein (2007) for sedimentary and volcanic rocks. It highlights nine fundamental pore types of granitic rocks including (i) moldic, (ii) sieve, (iii) interparticle, (iv) intracrystal and (v) vug pores, (vi) open regular fractures, (vii) open irregular fractures, (viii) closed disconnected fractures and (ix) microfractures, the last of these defined as fractures <0.5 mm in aperture. This petrographic dataset was then recorded and compared with complementary results from micro-XRF, hyperspectral analysis and CT scan imaging.
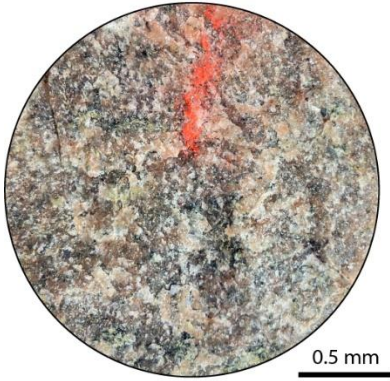
The granites were classified into four groups based on their reservoir properties: (1) massive, (2) fractured, (3) brecciated and (4) altered granites. The fractured granites were subdivided into three sub-groups based on the morphology of their fractures: (2a) open regular, (2b) open irregular and (2c) closed disconnected fractures (Figure 32).

The massive granites represent the original rock formed through the crystallization of felsic magma, with its initial structure and composition remaining largely unaffected by post-emplacement processes. The main minerals comprise quartz, plagioclase (albite and oligoclase) and K-feldspar. Mafic phases account for ~10% of the rock and include biotite and minor occurrences of hornblende and pyroxene that are occasionally partially replaced by chlorite. Accessory minerals such as titanite, apatite, allanite and zircon are also present (Figure 33).
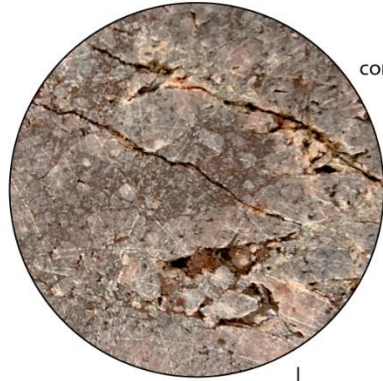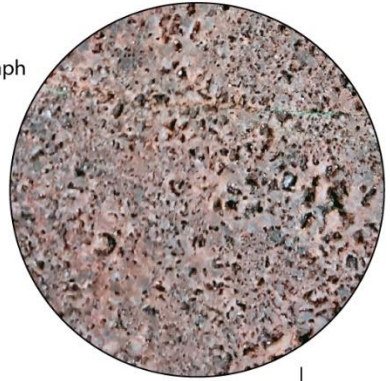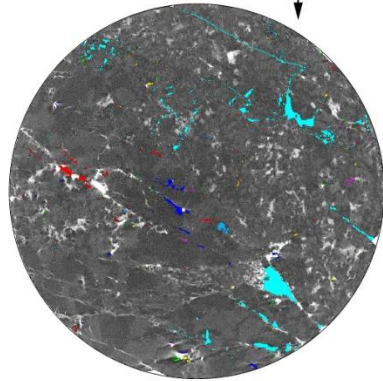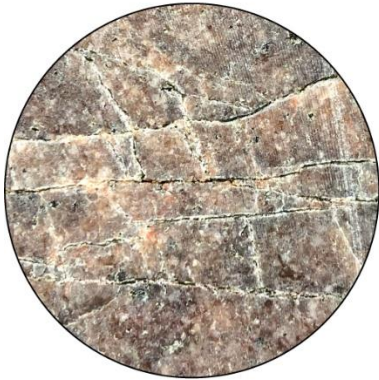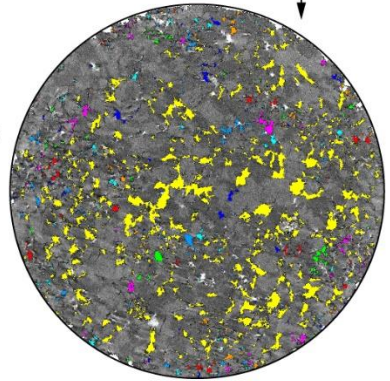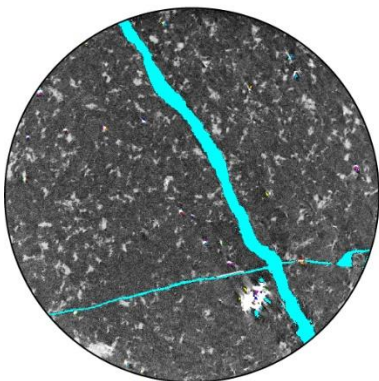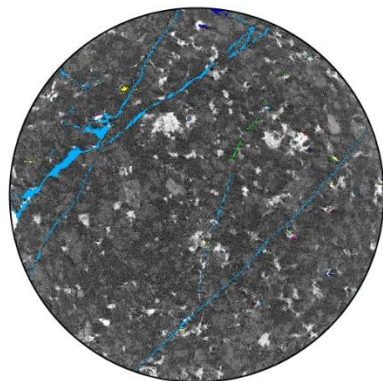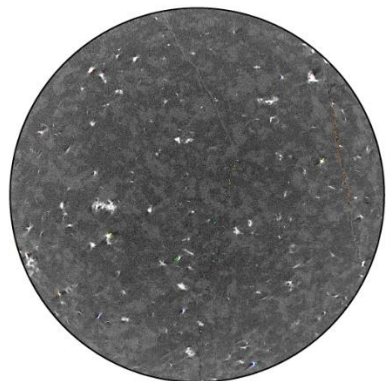
Figure 32. Pore network classification of the main granitic rock types within our dataset. Granites were classified into (1) massive, (2) fractured, (3) brecciated and (4) altered. Fractured granites were further divided into (2a) open regular, (2b) open irregular and (2c) closed disconnected. CT scan pore segmentation is highlighted in colours, while the mineral density is displayed in grey shades.

Fractured granite

Brecciated/cataclastic granite
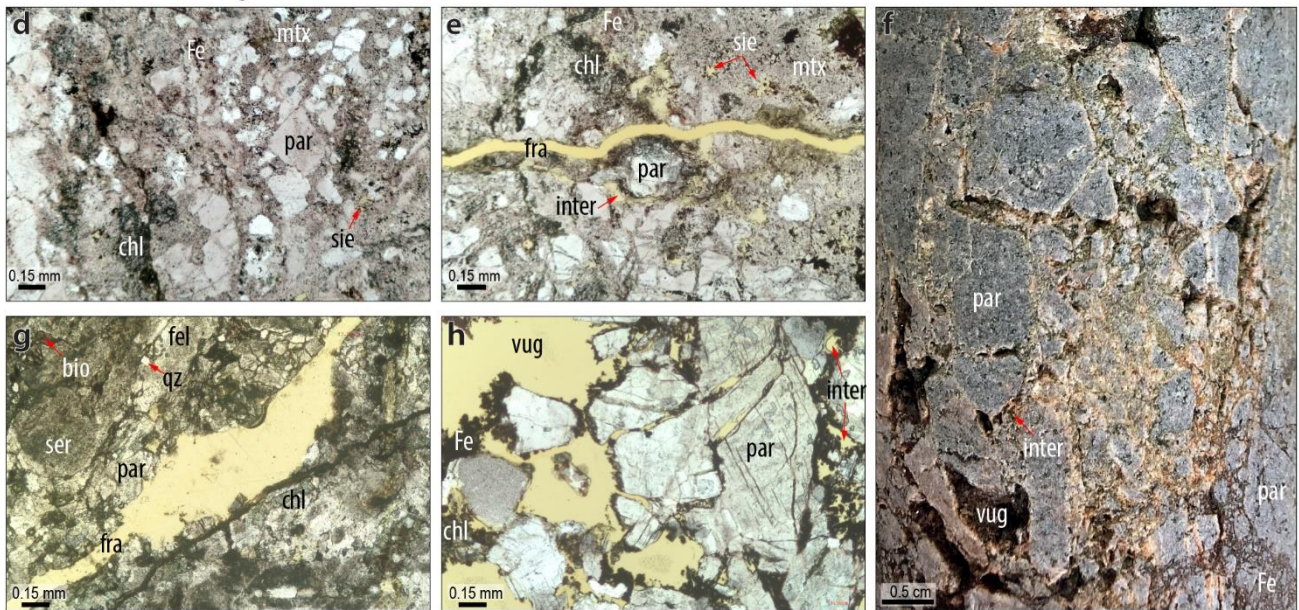
Altered granite
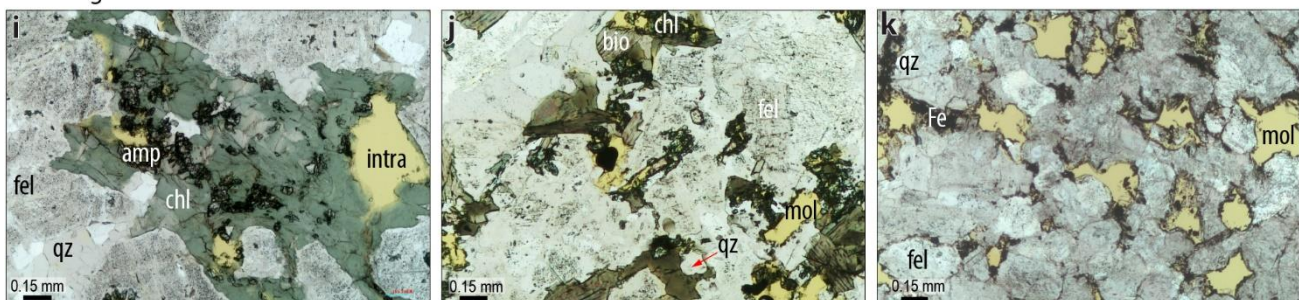
Figure 33. Drill core photographs (b, c, and f) and thin-section images in plain polarized light (a, d, e, g, h, i, j, k) showing the minerals, textures, structures, and pore types of the granitic reservoirs identified in this study. Abbreviations are: fel (feldspar), qz (quartz), amp (amphibole), bio (biotite), chl (chlorite), epi (epidote), ser (sericite), Fe (iron oxides, including magnetite, hematite and ilmenite), py (pyrite), par (particles, referring to cataclastic grains >1 mm in size), mtx (matrix, referring to cataclastic grains <1 mm), fra (fracture pore), inter (interparticle pore), intra (intracrystal pore), sie (sieve pore), vug (vug pore) and mol (moldic pore). Rock porosity is highlighted in yellow.

4.5.1.3 Hyperspectral analysis

Hyperspectral imaging is a non-invasive method that provides information on the mineralogical, mineral chemical composition and structural aspects of rocks. This method records different wavelengths of the electromagnetic spectrum of the samples in tens to hundreds of bands. GTK acquired hyperspectral data from the Koillismaa Deep Drillhole in 2021–2022 using a SisuROCK drill core scanner with Specim RGB, FENIX and OWL hyperspectral cameras. The data were acquired from air-dried samples at room temperature with a resolution of ~1.5 mm pixel size in the visible (480–700 nm), near-infrared (700–1300 nm), short-wave infrared (1300–2500 nm) and long-wave infrared (7500–12 000 nm) wavelength regions. In addition, high-resolution (0.15 mm) RGB (red, green, blue) data were acquired from the drill cores. Here, only RGB and FENIX data were used.

For the purposes of this work, the focus was placed on chlorite abundance using scalar D2250 (e.g., McLeod et al. 1987) extracted using IntelliCore® software by Terracore, only evaluating the spectra of the granitic rocks. Scalars are extracted in IntelliCore® by applying a continuum removal to the spectral signatures (hull quotient from 1300 nm to 2450 nm) before defining the depth of the spectral minima (D). The defined window for searching D2250 minima in the spectra is from 2232 nm to 2285 nm. Numerical values for scalars are generated by taking a mean value across each 10-cm interval of the image dataset. D2250 is also developed for biotite and epidote, although to a lesser degree than for chlorite (Laukamp et al. 2021). Since biotite is also absent from the best-developed reservoirs in our dataset, the absence of D2250 can be used as a proxy for exploring areas of potential porosity, as well as opened versus mineralized fractures, and rock structures such as brecciation (Figure 34). As the hyperspectral images are collected from drill cores, the method cannot distinguish natural fractures from those caused by drilling. Thus, interpretation from hyperspectral imaging must be validated by complementary information from drill core description, petrography, and analytical techniques (e.g., micro-XRF). Overall, granitic rocks displaying hot colours highlight the presence of secondary mineralization, closed fractures and massive rocks, while cold colours show rock fragmentation, pores, and open fractures (Figure 34).

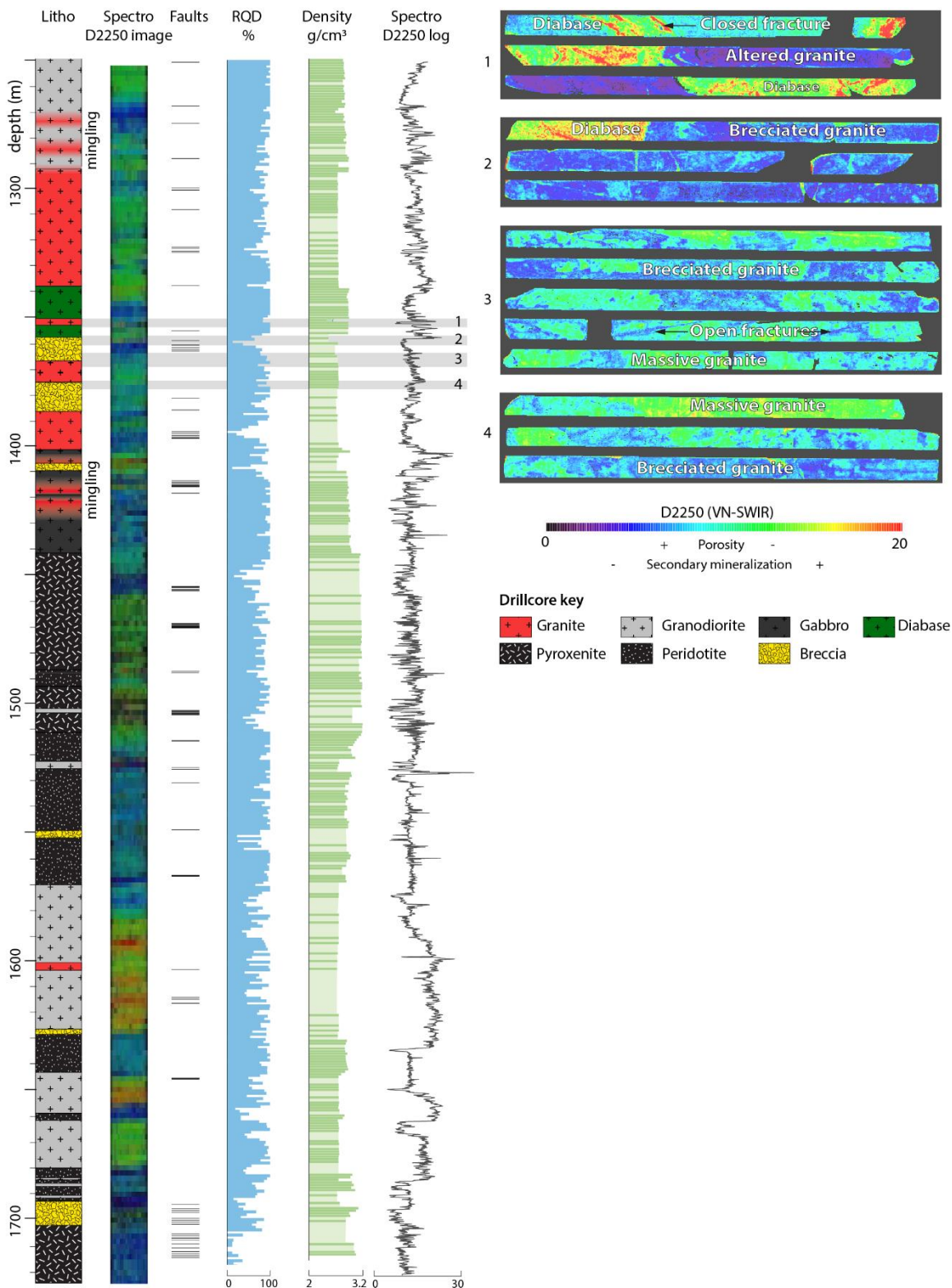**Figure 34.** Composite borehole data displaying the lithology, D2250 scalar based on hyperspectral data, location of faults, RQD and rock density of the studied interval. For the granitic rocks, hot colours in the D2250 hyperspectral image highlight the presence of secondary minerals, closed fractures and massive rocks, while cold colours show textures such as rock fragmentation, open fractures and pores.

4.5.1.4 Micro-XRF quantification

Micro-XRF analysis of seven samples was obtained at the GTK Research Laboratory in Espoo. Micro-XRF is a non-destructive analytical technique used to determine the elemental composition of a sample at a microscopic scale. It is based on the principle of X-ray fluorescence, where a material is irradiated with X-rays. By measuring the energy and intensity of the emitted X-rays, the elements present in the sample can be detected and quantified. We primarily aimed to analyse the mineral phases and alterations, textures, and compositions of samples. Secondarily, we tested the performance of micro-XRF data coupled with AMICS quantification (Advanced Mineral Identification and Characterization System) to verify the pore space distribution of our samples. These data were compared with deterministic results from CT scans and petrophysical measurements, including gas pycnometry and drill core water saturation tests.

The instrument used was a Bruker Micro-XRF M4 Tornado Plus with AMICS, equipped with a 30-Watt rhodium (Rh) anode X-ray tube and two 30 mm^2 silicon drift detectors (SDDs) with a resolution of <145 eV (MnKα) at 275 kcps (kilo counts per second). The Rh X-ray source was operated at maximum energy settings (50 kV, 600 μA) and a polycapillary lens focused the beam on a fixed spot size of 20 μm under a 2-mbar vacuum. Elemental mapping of the samples was performed using a step size of 20 μm and a pixel dwell time of 20 ms. Qualitative elemental maps were generated for all samples using the Bruker M4 software equipped with the AMICS package. Bruker AMICS offers automated mineralogical analysis and image processing tools for quantitative mineral identification, grain boundary detection, particle size analysis and mineral mapping. We utilized techniques such as image segmentation, pattern recognition and statistical analysis to extract meaningful information from digital images of samples obtained through micro-XRF analysis. By using χ2 fingerprinting for a best-match mineral classification, we compared our collected micro-XRF datasets with a reference list of known mineral spectra embedded into the AMICS software. This initial comparison guided our mineral recognition and classification, which was further refined using various clustering techniques and manual manipulation of XRF spectral attributes. The data were repeatedly reclassified to resolve X-ray points that were initially unclassified (i.e., determined as unknown elements), following methods presented in Bruker (2018).

The final micro-XRF quantification product was a series of mineral and pore-class maps presenting a single class label or class mixtures per 20 μm pixel resolution, not exciting 2% of unknown points (Figure 35). These maps allow us to quantify the relative mineral and pore distribution within the samples, which aided rock classification using QAP (quartz vs. alkali feldspar vs. plagioclase) and feldspar type (albite vs. anorthite vs. orthoclase) diagrams. This method was particularly important to determine the primary mineral composition of the rock samples and to assess the post-emplacement processes that have created pore-type variations within the rock dataset. Most granitoids were mineralogically classified as classic granites, although minor granodiorite and quartz-monzonite variations also occur. For this study, these granitoids are simply referred to as 'granites'.

Micro-XRF elemental map
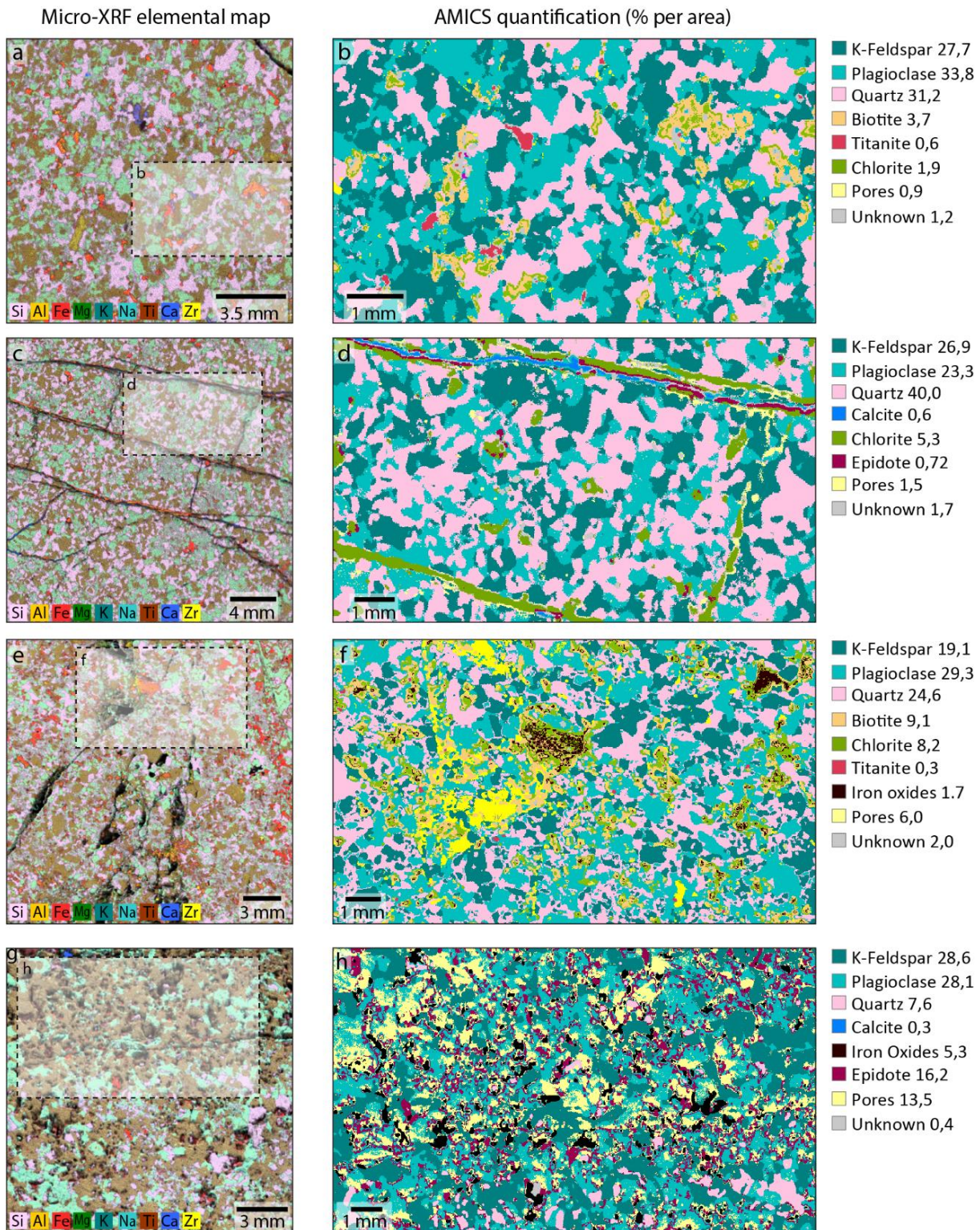
AMICS quantification (% per area)

Figure 35. Micro-XRF results showing the chemistry, mineral composition, and pore quantification of selected representative samples: massive granite (a and b), fractured granite with closed and disconnected fractures (c and d), brecciated granite (e and f) and altered granite (g and h).
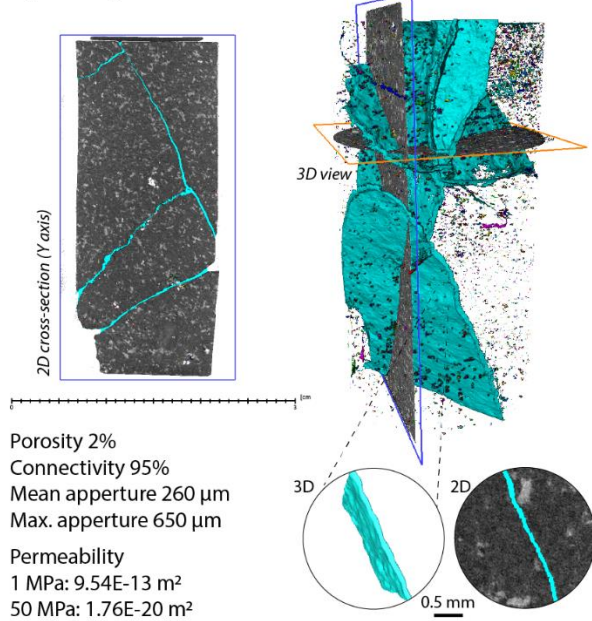
4.5.1.5 CT Scanning

CT scans provide information on the internal structure, composition, and density variations of rock samples. The technique uses X-rays to create detailed 3D reconstructions of the interior of the rocks. In this study, tomography analysis of the rock drill cores was used to characterize and quantify parameters such as pore morphology, distribution, and connectivity. In addition to the pore network data, the tomographic images helped to assess critical minerals and their altered variations. CT scans were collected at GTK's X-ray Computed Tomography Laboratory in Espoo using a GE Phoenix v|tome|x scanner. The samples were scanned using a helical trajectory in which the sample rises while it rotates. For the first set of lower-resolution scans, seven rock cylinders of various lengths and 50 mm in diameter were scanned using an accelerating voltage of 150 kV and a tube current of 225 μA, resulting in a total power of 33.75 W. Copper and aluminium sections of 0.5 mm were used as beam filters, and the obtained spatial resolution of the images was 30 μm. At each angle, the detector waited for a single exposure time and then took an average of 2–3 exposures. The single exposure time was set as 1 s, and 4647–7386 projections were taken, resulting in a total scanning time of 310–388 min per sample.

From these initial lower-resolution scans, zones of interest were selected for further assessment. After a preliminary analysis of the pore distribution and potential weak parts of the rocks that could be damaged during rock preparation, seven smaller rock cylinders measuring 40 mm in length by 19.8 mm in diameter were cut. The CT scanning parameters were set as per the lower-resolution dataset, except that the tube current was changed to 75 μA and the power to 11.25 W, now using 0.1 mm of copper as a beam filter. The spatial resolution was 11 μm, averaging 3 exposures each time, with a single exposure time of 0.5 s, obtaining 4691–5695 projections for a total scan time of 156–190 min. From this higher-resolution dataset, the images were segmented using the Mask Segmentation and 2-Phase Watershed Segmentation recipes of ThermoFisher PerGeos 2020.2. Low-density regions corresponding to void volumes within the rock cylinders were coloured to facilitate the visualization of the pores. Pore connectivity was then studied using the Labeling tool to assign a different label/value to each connected pore body, resulting in images where all pores of the same colour are connected at a limit of 11 μm in diverse zones of the rock sample (Figure 36).

Open regular fracture

Porosity 2%
Connectivity 95%
Mean apperture 260 µm
Max. apperture 650 µm

Permeability
1 MPa: 9.54E-13 m²
50 MPa: 1.76E-20 m²

Open irregular fracture

Porosity 4%
Connectivity 80%
Mean apperture 200 µm
Max. apperture 1230 µm

Permeability
1 MPa: 2.84E-14 m²
50 MPa: 1.84E-16 m²

Brecciated granite

Porosity 7%
Connectivity 75%
Mean apperture 180 µm
Max. apperture 1200 µm

Permeability
1 MPa: 1.91E-15 m²
50 MPa: 1.79E-16 m²

Altered granite

Porosity 17%
Connectivity 75%
Mean apperture 150 µm
Max. apperture 735 µm

Permeability
1 MPa: 5.49E-14 m²
50 MPa: 3.97E-14 m²
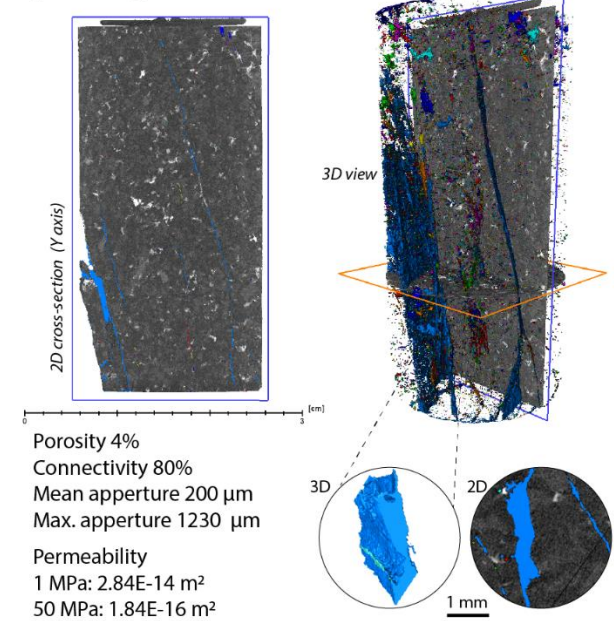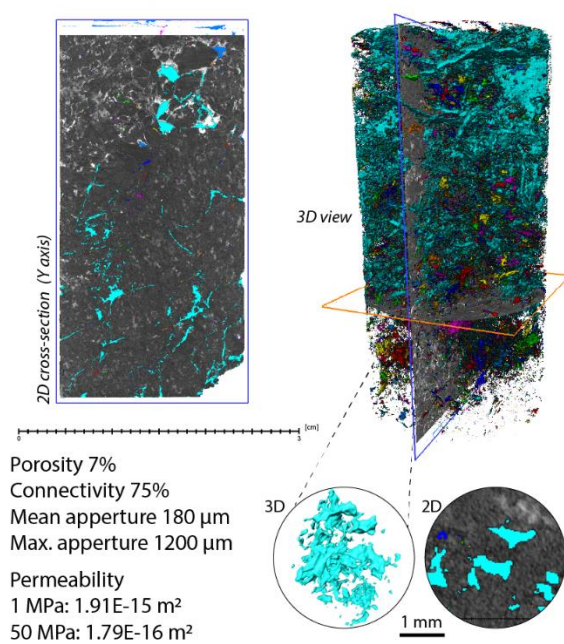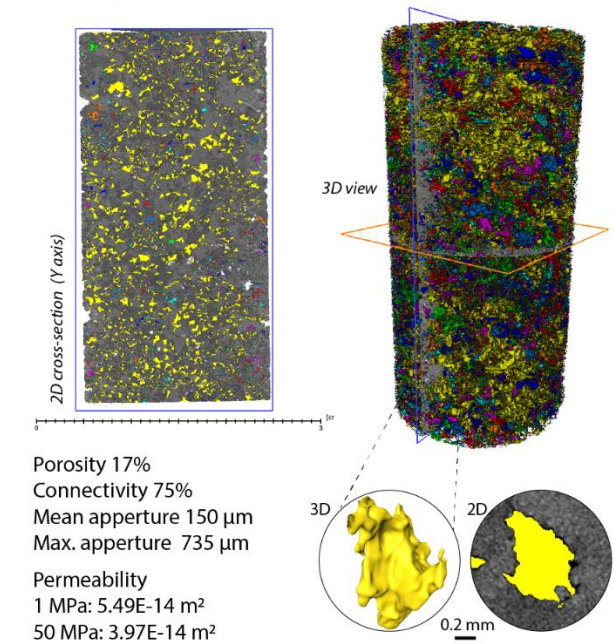
Figure 36. CT scan images highlight the pore morphology and connectivity of four types of granitic reservoirs found within the samples. Low-density regions that correspond to void volumes were coloured to facilitate the visualization of the pores. Porosity values are from gas pycnometer measurements, whereas the permeability values are from steady-state and pulse decay measurements at increasing confining pressures. Pores of the same colour are connected at a limit of 11 µm resolution (connectivity label displayed as a percentual value). CT scan videos are provided as part of the supplementary material.

4.5.1.6   Petrophysical measurements

Density, connected porosity, P-wave velocity and thermal conductivity were measured at the University of Strasbourg and GTK laboratories, while measurements of sample porosity and permeability as a function of confining pressure were performed at the University of Strasbourg (Figure 37). Appendix 3 presents a detailed compilation of the methods and tests applied for each sample and their respective results. Minimal variations in the data measured in the two institutions (in France and Finland) were observed among samples belonging to the same lithofacies group. Therefore, we conclude that the application of different methods at the two institutions did not significantly impact the first order petrophysical and thermal interpretation of crystalline reservoirs.

Experiments performed at the Strasbourg Institute of Earth & Environment (University of Strasbourg, France)

All the samples measured in Strasbourg were 19.8-mm-diameter cylinders with a nominal length of 40 mm. Samples containing large fractures were wrapped in adhesive tape for the measurements of P-wave velocity, thermal conductivity, and permeability.

The samples were first vacuum-dried in a vacuum oven at 40 °C for at least 48 hours. The bulk density of the samples measured in Strasbourg was determined using the dry mass, measured using a digital balance (accuracy of 0.001 g), and the sample dimensions, measured using digital callipers (accuracy of 0.01 mm). The connected porosity was measured using the bulk sample volume (calculated using the sample dimensions) and the skeletal volume was measured using a helium pycnometer (Micromeritics AccuPyc II; accuracy of 0.0001 cm^3). P-wave velocity was measured on dry samples using two piezoelectric sensors, a function generator (Agilent Technologies 33210A, 10 MHz function/waveform generator), a signal amplifier and an oscilloscope (Agilent Technologies DSO5012A digital storage oscilloscope). A schematic diagram of the device can be found in Heap et al. (2014). P-wave velocity was measured along the axis of each of the samples (using a frequency of 700 kHz) under ambient laboratory pressure and temperature. To ensure a good connection between the sample and the endcaps, we applied an axial force of 300 N. Thermal conductivity was measured using a Hot Disk® 500 Thermal Constants Analyzer using the transient plane source method (Gustafsson 1991; Heap et al. 2020). The TPS method uses a resistive sensor (the transient plane source) sandwiched between two samples to measure the increase in resistance as it heats the samples using an electrical current pulse. In this setup, the resistive sensor consists of two 10-µm-thick nickel foil spirals (radius of 3.189 mm) that are encased and insulated by 30-µm-thick Kapton. Measurements were taken by sandwiching the sensor between the cylindrical sample to be measured and a piece of high-porosity foam with a very low thermal conductivity. A good contact between the sensor and the surface of the sample was ensured by tightening a screw positioned at the top of the sample jig. The standard error for the thermal conductivity measured using our Hot Disk® TPS 500 Thermal Constants Analyzer, assessed by measuring the same sandstone sample 100 times, was found to be 0.007 W·m^{-1}·K^{-1} (Heap et al. 2023).

Permeability measurements were performed at the ITES Rock Physics laboratory on five samples that were submitted to increasing confining pressure from 1 to 50 MPa. Confining pressures are commonly used to simulate the conditions deep within Earth's crust. Here, confining pressure was applied to simulate the permeability of the rocks at increasing depths from 0 to ~2 km, considering a constant crustal density of 2.6 kg/cm^3, typical of crystalline terrains. Gas (argon) permeability

measurements were performed in a high-pressure vessel (50 MPa) at room temperature on cores 40 mm long and 19.8 mm in diameter. Samples were vacuum-dried at 40 °C for 12 hours, and then jacketed in a Viton sleeve and placed inside the pressure vessel. The confining pressure was then increased to 1 MPa and left for 24 hours at this pressure to allow for microstructural equilibration. Argon permeability was measured using either the steady-state method or the pulse-decay method, depending on the permeability of the sample. For the steady-state method (high permeability of >10–16 m^2), a constant pressure gradient was imposed across the sample and the outlet flow rate was measured using a flowmeter. Permeability was then derived from a modified Darcy's law designed to estimate the flow rate of compressible fluids (Scheidegger 1974). For the pulse-decay method (used for the lower permeability samples; <10–16 m^2), the decay of the initial pressure gradient was monitored after the closure of the upstream pore fluid inlet, the downstream pressure being in all cases the atmospheric pressure. A local application of Darcy's law to the interface between the upstream gas reservoir and the sample thus leads to the permeability of the sample (Brace et al. 1968). When Darcy's law was no longer valid, a correction was introduced to the measured values because either inertial effects appear at high flow rates (Forchheimer correction) or gas slippage appears along the pore walls at low permeability (Klinkenberg correction). The process was repeated for each confining pressure level by respecting the 12-hour equilibration period, resulting in a total experiment time of ~240 hours per sample.

The porosity of the 19.8-mm-diameter sample of the altered granite (Koi-01b) was measured as a function of confining pressure in a hydrostatic pressure vessel (a type of experiment often referred to as a 'hydrostat'). This sample was first vacuum-saturated with deionized water, inserted into a Viton sleeve, and placed inside the pressure vessel. The confining and pore fluid pressure was then increased to 2 and 1 MPa, respectively, using servo-controlled pumps, and the sample was left overnight to ensure microstructural equilibration. The following morning, the confining and pore fluid pressure was slowly increased to 12 and 10 MPa, respectively, and the sample was again left to equilibrate. The volume of deionized water in the sample was monitored during the experiment using an encoder incorporated into the servo-controlled pore fluid pressure pump. Once the volume of water within the sample was constant for a protracted duration, the sample was considered to have fully equilibrated to the starting effective pressure of 2 MPa (we assume here a simple effective pressure law in which the effective pressure is equal to the confining pressure minus the pore fluid pressure). The confining pressure was then increased at a constant rate of ~10 MPa/h to a maximum of 50 MPa. During pressurization, the change in the volume of water within the sample, converted to a porosity change using the sample dimensions, was monitored, and recorded. This experiment therefore provides the porosity reduction as a function of effective confining pressure.

Experiments performed at the GTK laboratory (Finland)

At the GTK laboratory, 14 polished discs of 7 × 50 mm and 2 cylindrical samples of 30 × 50 mm were prepared for density, connected porosity, P-wave velocity, and thermal conductivity measurements. Initially, the samples were washed and oven-dried for 72 hours at a temperature of 40 °C. Due to the fragility of fractured and altered samples, they were wrapped in adhesive tape before the measurements of P-wave velocity and thermal conductivity.

The bulk density of the samples was determined using the Archimedean principle by measuring the mass of the samples in the air and water. These measurements were conducted at a temperature of

approximately 20 °C using a precision scale with an accuracy of 0.01 g. The connected porosity of the samples was also determined using the Archimedean principle, using the 'triple-weight' water-saturation method. To do so, the samples were first immersed in water for 72 h and their wet mass was measured in air and suspended underwater using a precision scale with an accuracy of 0.01 g. The samples were then dried for 48 hours at a temperature of 105 °C and their dry mass was measured using the same precision scale. The connected porosities of the samples were then calculated using Archimedes' principle. P-wave velocity was measured under wet conditions using a device developed by GTK. This device operates by measuring the propagation time of a high-frequency (1 MHz) acoustic pulse across the samples. The pulse generator emits an acoustic pulse that traverses the sample, and the travel time is precisely measured with a pulse counter. The accuracy of the method is approximately 10 m/s, ensuring reliable results. Finally, the samples were soaked in water for a duration of 14 days, and thermal conductivity tests were conducted under wet conditions using the divided bar method (Beck 1988). In this method, the sample is positioned at the centre of a vertical column consisting of alternating quartz and copper discs. Initially, the top and bottom of the column were maintained at constant temperatures, and subsequently, a differential temperature of 10 °C was applied. This temperature difference generates a heat flux through both the column and the sample. Temperature variations are recorded from the quartz and copper materials and the sample itself. The thermal conductivity of the samples is then calculated using Fourier's law. The samples were then air-dried at room temperature for approximately 90 days and their thermal conductivity was determined under dry conditions using the same method.

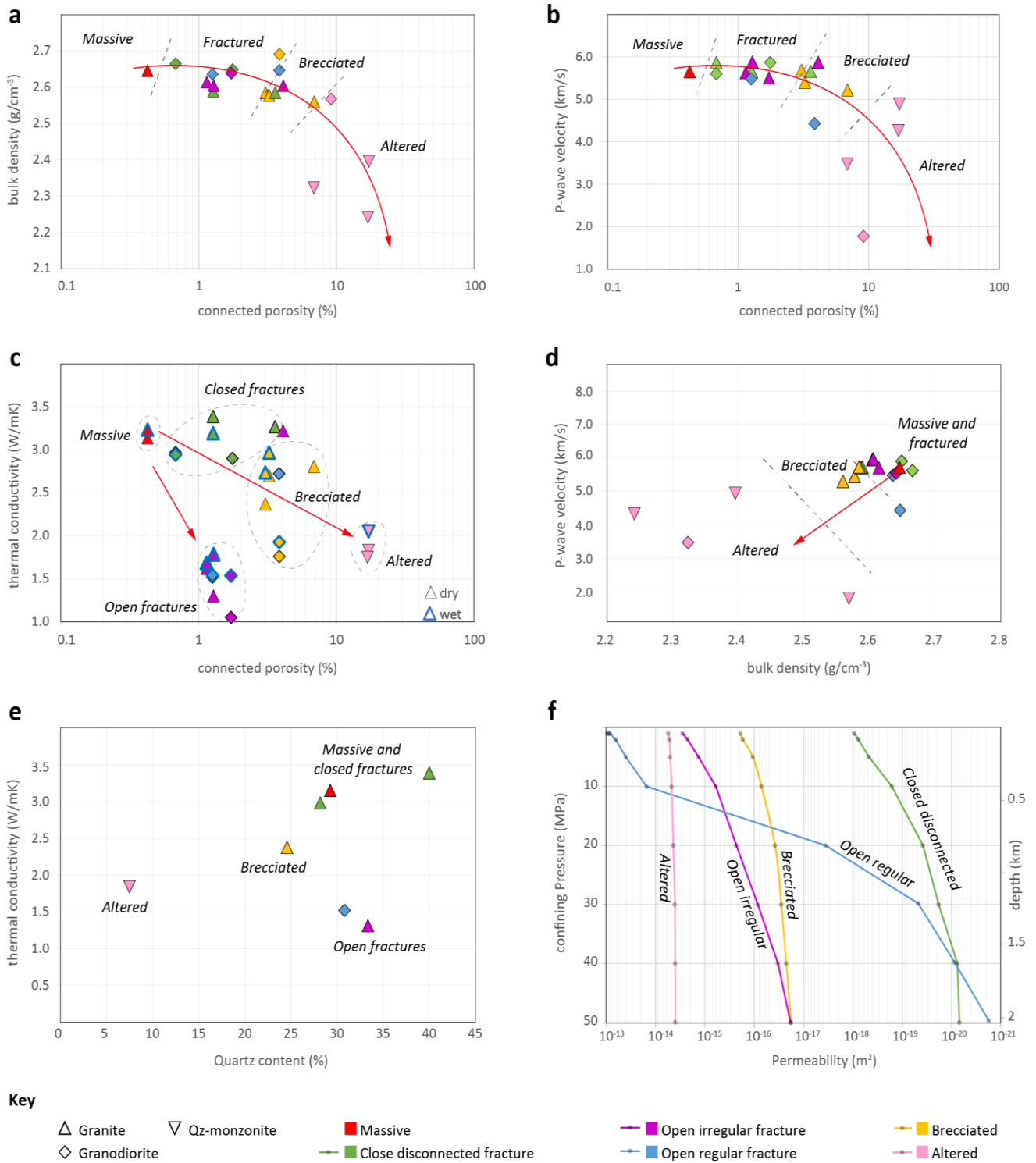**Figure 37.** Petrophysical and thermal data on the granitic rocks investigated in this study. The observed heterogeneity of these rocks is mainly controlled by their distinctive pore network, which, in turn, is determined by brittle deformation (fracturing and brecciations) and mineral alteration processes. Depth estimation in (f) considers a crystalline setting in which the lithostatic load is 2.6 kg/cm^3.

4.5.1.7 Conclusions

The vast potential of fault and shear zones as deep geothermal reservoirs in crystalline settings remains largely untapped in crystalline settings. While fracture permeability is recognized as a critical factor in creating prolific crystalline reservoirs within these zones, the effects of processes such as brecciation and mineral alteration have received limited attention. Our study revealed the presence of granitic reservoirs occurring at depths of nearly 2 km within the Fennoscandian Shield. At a confining pressure of 50 MPa (simulating their present depths), these granitic reservoirs exhibit a high porosity of nearly 20% and a high permeability of ~5 × 10−14 m^2 (50 mD). Brecciation, cataclasis, fracturing and mineral dissolution collectively contribute to the creation of these exceptional reservoir properties, which are rarely encountered in deep and ancient (over a billion years) crystalline rocks. Our study demonstrates that brittle shearing and high-temperature (200–300 °C) hydrothermal alteration are key factors in the formation of granitic reservoirs. These processes are typical of brittle shear zones, which have the potential to create extensive (>100 m) interconnected crystalline reservoirs. Our findings unveil a new reservoir play for expanding geothermal energy production in crystalline terrains globally: brittle shear zones that have undergone propylitic alteration. Developing geothermal resources associated with these altered shear zones stands to make a substantial contribution to our ongoing shift towards cleaner and more reliable energy sources.

4.5.2 *In situ* geothermal assessment

The temperature profile of the bedrock was measured with a fibre-optic cable providing a precise description of the temperature at intervals of 0.5 metres along the entire length of the cable. The fibre-optic cable was successfully installed into the drillhole to a hole length of approximately 1162 metres. While we had more cable available, there was an obstruction in the hole, preventing the cable from being installed any deeper. The measurement depth was sufficient for us to estimate the temperature gradient.

Temperature measurements with distributed temperature sensing (DTS) are based on Raman scattering. Monochromatic light pulses are forwarded from the DTS device (Silixa XT) to the single- or multimode optical fibres. The ratio between Stokes and anti-Stokes intensities is used for the calculation of temperature in the scattering point.

In the measurement, cable manufactured by Solifos was used, which includes both single- and multimode optical fibres, meaning that the same cable can be utilized for both DTS and distributed acoustic sensing (DAS) measurement.

We conducted DTS measurement with a single-ended configuration, meaning that a light pulse is emitted in a forward direction. Calibration of the DTS data then requires that we know the true temperature value at two points of the fibre-optic cable. At the other end of the cable (drillhole bottom), we attached an Antares Datensysteme point temperature sensor, and at the ground level, we used an RBRSolo sensor. With the precise point temperature readings from these sensors, an offset correction was applied to the DTS data. This correction is typically very small. Figure 38 presents the DTS profile of the drillhole and its temperature gradient along depth. The bottom temperature at the depth of 1162 m was only 12.0 °C and temperature gradient was found to vary between 0.7–0.81 °C/100 m, being lower in the upper parts of the bedrock. The bedrock was coldest at depths of 10 and 60 m, the temperature being 4.0 °C.
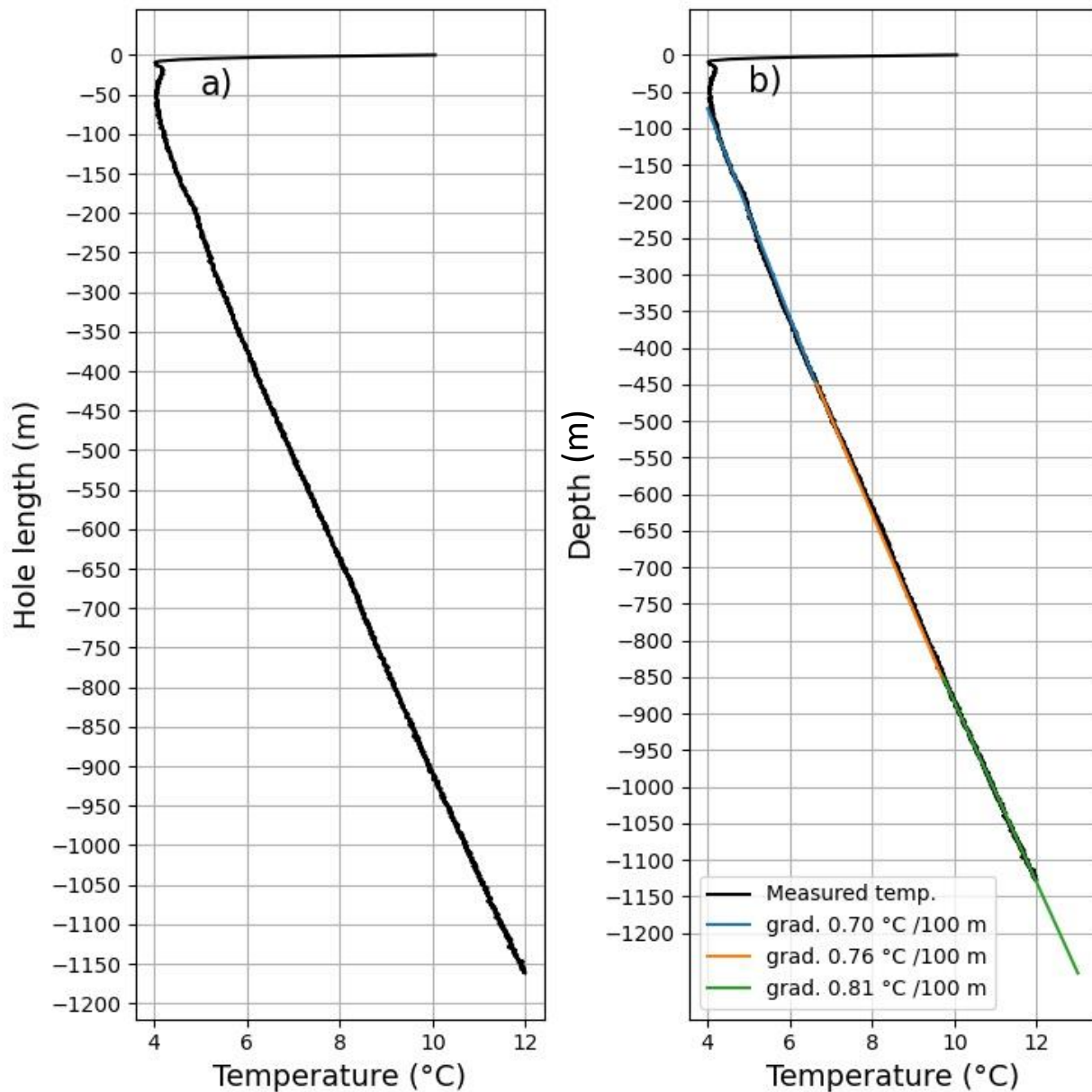
Figure 38. DTS measured temperature profile of the drillhole as a function of a) length and b) depth.

If in addition to the temperature gradient, being aware of the heat flux in the bedrock, it was also possible to estimate the effective thermal conductivity. Distributed temperature measurements with fibre optics can be divided into passive and active methods. While a passive method, such as the one conducted in the Koillismaa drillhole, can only provide information on the natural non-changed temperature conditions of the bedrock, the active method can reveal possible fracture zones with depth and provide a means to determine the effective thermal conductivity of the bedrock with depth. This is possible because in the active method the surrounding rock volume is heated up. If some layer contains water-conducting zones, this depth heats up less than the intact rock. Active distributed temperature sensing (ADTS) measurement can be conducted in both drillholes and borehole heat exchangers but was not tested in Koillismaa.

4.5.3 Finite element modelling

The modelling work involved conducting a series of numerical simulations to test the performance of hypothetical geothermal reservoirs under diverse exploitation scenarios, utilizing the petrophysical results and findings outlined in section 4.5.1 (Reservoir and thermal assessment of drill core samples). To create these models, we opted for a doublet geothermal system consisting of injection and production wells strategically positioned 500 metres apart from each other and across the hypothetical reservoirs. The numerical modelling was conducted using a finite element method (FEM) to simulate heat and fluid transfer across the reservoirs considering two scenarios: (i) a doublet geothermal system with the production well positioned at a depth of 1 km and (ii) a system with the production well at a depth of 3 km. Models were constructed and solved using Comsol Multiphysics® software.
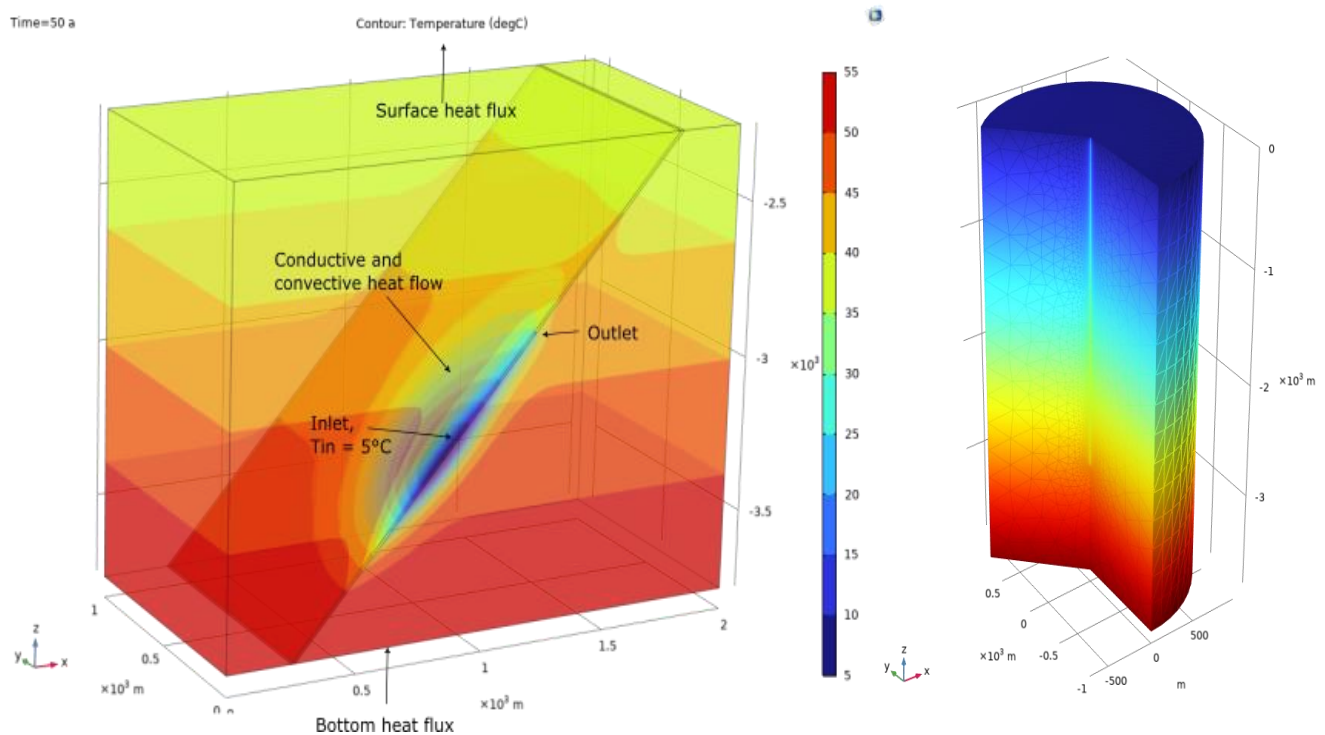
Figure 39. Model geometries. Left: the doublet model with a tilted reservoir in the middle. The side facing the viewer is a symmetry edge. Right: the cylinder symmetric pipe model with a pipe flow in the middle.

Calculations were performed considering a 3D block of homogeneous impermeable rock intersected by an inclined reservoir layer of 10 m in thickness and tabular geometry and varying porosity, permeability, and thermal properties (Table 3). The model has one symmetry axis, so it is cut in the middle for computation purposes. The reservoir is considered infinite in other two dimensions, e.g., its boundaries are set in a way that it is not limited by the model geometry. Considering the extent of the thermal plume between the wells, the rock mass volume interacting with the doublet system is approximately 0.01 km³.

Geological parameters of the reservoir were defined as per three reservoir facies as (i) altered granite (based on laboratory and experimental data from sample Koi-01), (ii) brecciated granite (based on data from sample Koi-02) and (iii) open irregular fractured granite (based on data from sample Koi-03). The reservoir section included injection and production wells that circulate water across the porous medium. Due to the reservoir inclination, the bottom of the injection well is 350 metres deeper than the bottom of the production well. Additionally, a separate 2D model calculated heat losses in the pipe bringing the heated fluid to the surface. The model geometries are illustrated in Figure 39 and the model parameters are listed in Table 3.

4.5.3.1 Governing equations

Pressure in the matrix for a single-phased incompressible fluid is calculated from mass balance as

$$\frac{\delta}{\delta t}\,\theta\rho + \nabla\cdot\rho\boldsymbol{u} = Q, \tag{1}$$

where ϑ is matrix porosity, ρ is density and Q is a source term. Fluid velocity $\boldsymbol{u}$ in the rock matrix is calculated with Darcy's law:

$$\boldsymbol{u} = -\frac{\kappa}{\mu}(\nabla p + \rho_f g), \tag{2}$$

where κ is matrix hydraulic permeability, μ fluid viscosity and g is acceleration due to gravity. Subscripts r and f stand for rock and fluid, respectively. A fracture is included in the model as a boundary with higher hydraulic permeability κ_f.

The three-dimensional heat transfer equation used to describe the temperature field T is

$$\rho_r C_p \frac{\partial T}{\partial t} - k_r \nabla^2 T + \rho_f C_p \boldsymbol{u}\cdot\nabla T = 0, \tag{6}$$

where the first term is for the transient temperature change (t is time, C_p is the specific heat capacity), the second term is for conductive heat transfer (k is thermal conductivity) and the third term is convective heat transfer. The initial temperature in the rock matrix and fractures is calculated with the geological properties of the rock:

$$T_{initial} = T_{surf} - q\,z/k_r, \tag{7}$$

where T_{surf} is surface temperature, q is geothermal heat flux at the surface and z is depth (in a negative direction).

A fracture is coupled to the rock matrix and simplified in the model as a 2D boundary with an aperture a. Heat transfer in the fracture is calculated with

$$a\rho_r C_p \frac{\partial T}{\partial t} - k_{eff}\nabla^2 T + a\,\rho_f C_p \boldsymbol{u}\cdot\nabla T + aQ_s = 0, \tag{8}$$

$$k_{eff} = (1-\theta)k_f + \theta k_r,$$

where Q$_s$ is the heat source/sink, which, in our case, is the temperature at the borehole boundary, and k_{eff} is effective thermal conductivity, calculated with fluid and rock thermal conductivities weighted by the rock matrix porosity ϑ.

The power from the well is defined with

$$P = \rho C_p Q \Delta T, \tag{9}$$

where ΔT is the difference between the well inlet and outlet temperatures, and annual energy considering constant production is obtained by multiplying power with hours in a year:

$$E = P * 8766$$

The thermal energy value is purely heat extracted from the ground, and no heat pumps or surface structures are assumed in the model.

Table 3: Model parameters. Permeability variation measured under confining pressure conditions is presented in Figure 40.

Thermogeological parameters			
Mean annual ground temperature	5 °C		
Geothermal heat flux density	40 mW/m^2		
Reservoir variables	Altered granite	Brecciated granite	Open irregular fractures
Thermal conductivity	2.0 W/(m·K)	2.8 W/(m·K)	1.7 W/(m·K)
Density	2400 kg/m^3	2580 kg/m^3	2600 kg/m^3
Porosity	0.169	0.068	0.04
Simulation parameters			
Reservoir depth	1000 m and 3000 m		
Well lengths (injection/production)	1184 m / 830 m and 3184 m / 2830 m		
Reservoir thickness	10 m		
Well diameter	200 mm		
Well distance	500 m		
Simulation time	50 years		

Injection fluid temperature	5 °C
Fluid volumetric flow rate	20 kg/s
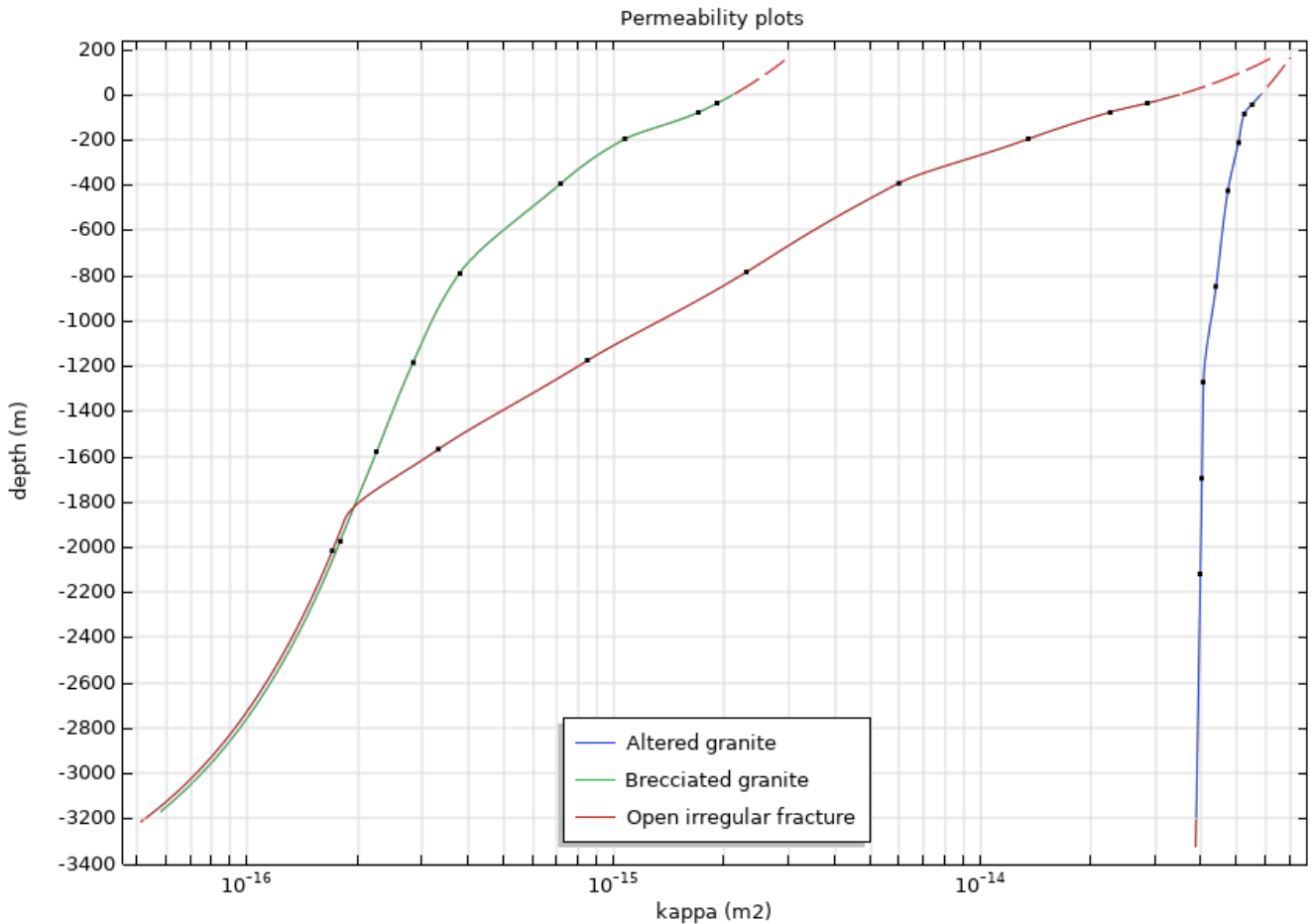
Figure 40. Extrapolated permeability of the three samples. Depth values are obtained from the confining pressure values and sample densities.

4.5.3.2 **Modelling results**

The results of the doublet production are presented as the production temperature and thermal energy values across a 50-year production timeline (Figure 39). The production temperature of a 1-km-deep reservoir starts at 16 °C, ascends to 16.7–16.9 °C at 4 years, when all geothermal fluids of the reservoir are utilized, and then gradually decreases to 12–12.5 °C after a total of 50 years of production. The respective thermal energy extraction values are 8 GWh/a at the beginning, peaking at 8.6–8.7 GWh/a and declining to 5.1–5.5 GWh/a after 50 years. Brecciated granite accounts for the highest peak value and lowest values after 50 years of production. The reservoir with open irregular fractures

accounts for smallest peak value, and altered granite produces the highest temperatures at the end of the production cycle of 50 years.

The production temperature of a 3-km-deep reservoir starts at 42.7 °C (27.3 GWh/a), ascends to 43.4 °C (27.9 GWh/a) at 2.6 years in the case of brecciated granite and to 42.8 °C (27.4 GWh/a) in the case of altered granite, and does not ascend at all in the case of open irregular fractures. The temperatures of brecciate granite decrease most drastically to 32.7 °C (18.8 GWh/a) after the total of 50 years of production, and to 35–35.2 °C (21.9–22 GWh/a) in the case of open irregular fractures and altered granite, respectively.

The temperature curves of the pipe across the length of the well show that injection fluid of 5 °C heats up by 0.3 °C in a 1.2-km-long well and 2.5 °C in a 3.2-km-long well (Figure 41). In the ascending fluid there are barely any heat losses in the 1-km reservoir well, but from the 3-km well, heat losses can be 1–2 °C.

It is important to note that these models only represent a working hypothesis used to evaluate the performance of various types of reservoirs that could potentially exist within a hydrothermally altered shear zone (Bischoff et al. 2023). The energy yields calculated here are unlikely to correspond to the geothermal resources at the Koillismaa location. They are solely used as a comparison tool to understand distinctive production scenarios across the studied reservoirs.
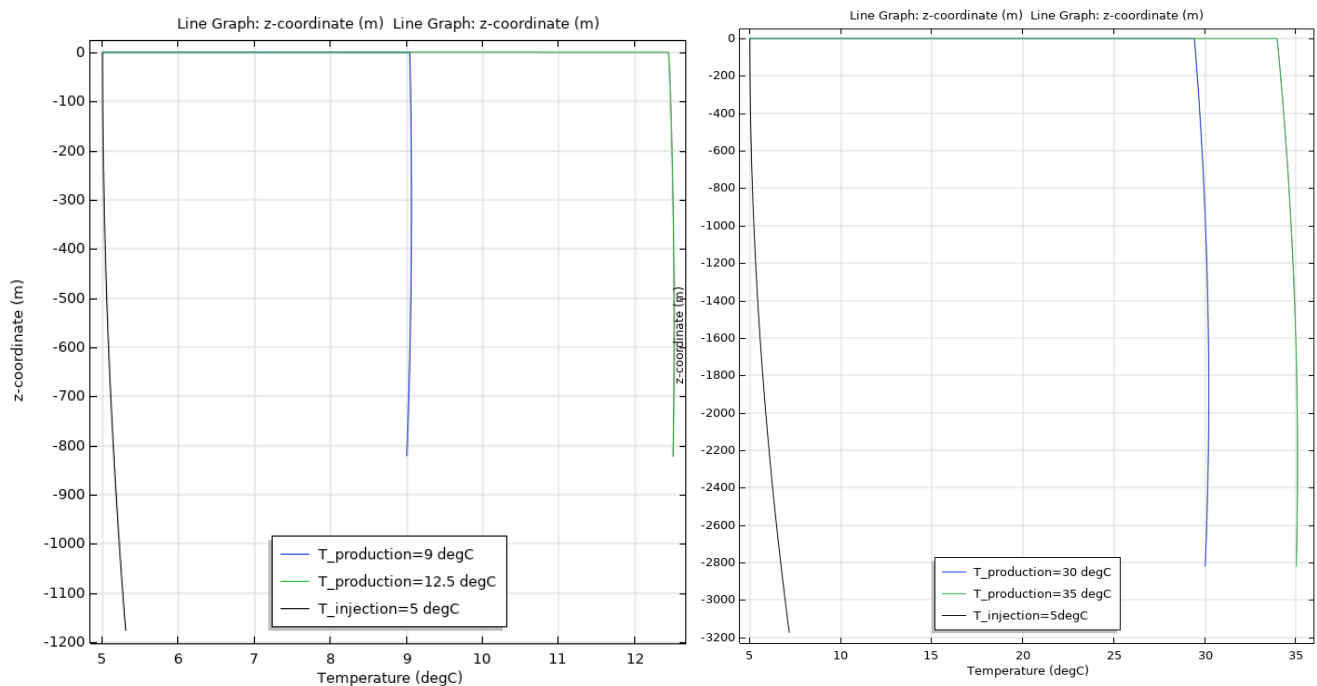

Figure 41. Pipe heat loss models for 1 km and 3 km pipes.

4.5.3.3 Conclusions

This study demonstrated that diverse reservoir types can exhibit pronounced differences in geothermal yields over a 50-year production timeline, particularly in a scenario where the production well is positioned at a depth of 3 km. In the 1-km-deep scenario, all reservoirs exhibit an initial ~5-year thermal ascension stage followed by a gradual descent. Conversely, in the 3-km-deep scenario, only the brecciated granite exhibits the initial ascension stage, while geothermal production from altered granites and open irregular fractures gradually decreases over time. Although the brecciated granite may yield higher outputs in the initial 15 years of production, over a 50-year period, its thermal power production is anticipated to decline more significantly compared to the altered and irregular fractured reservoirs. This phenomenon may be attributed to the higher thermal conductivity of brecciated granites compared to their altered and fractured counterparts; however, further studies are necessary to fully assess this phenomenon. In both the 1 km and 3 km scenarios, geothermal doublet systems extracting heat from altered granitic reservoirs are expected to outperform brecciated and fractured granites over a 50-year span.
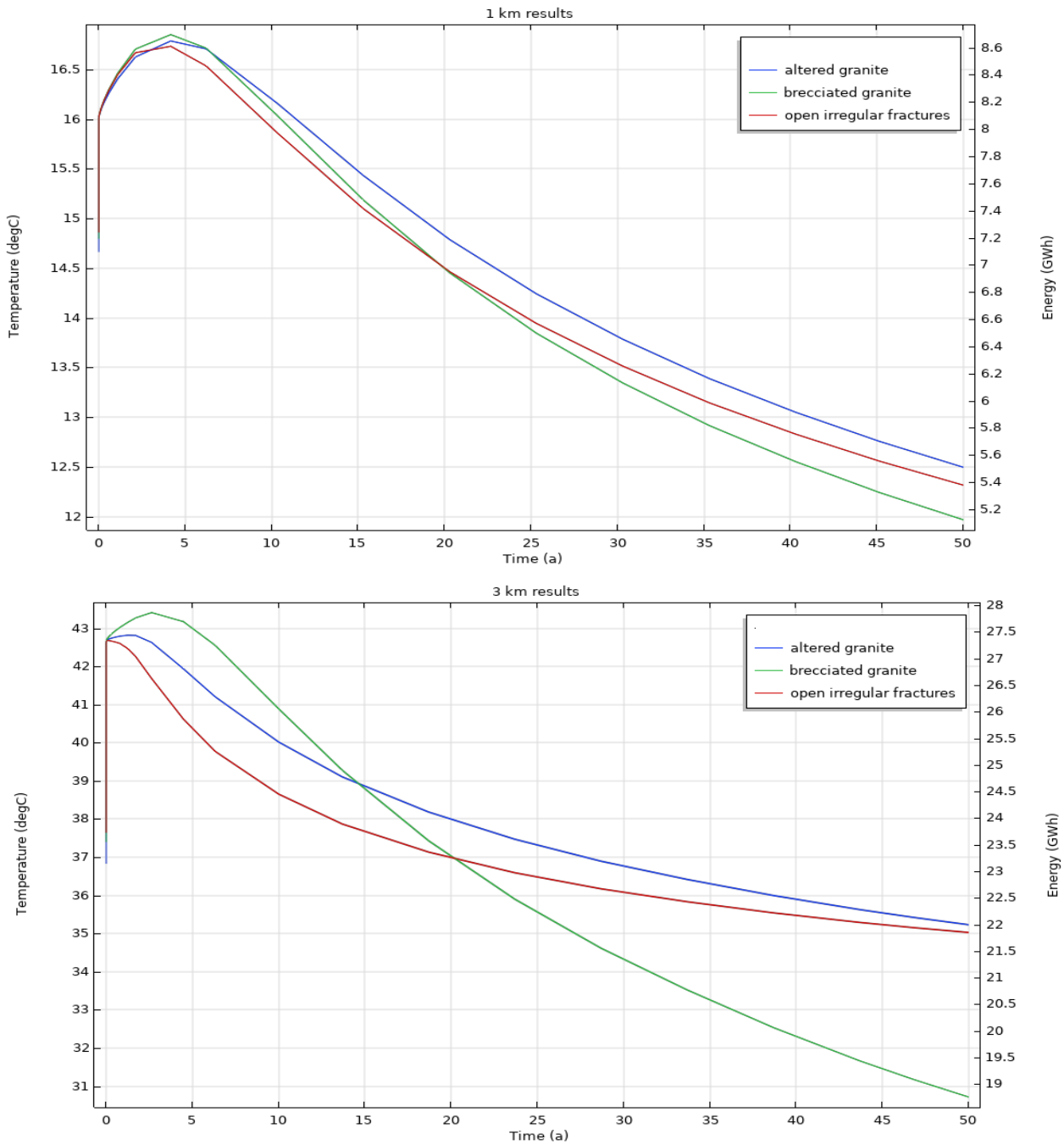
Figure 42. Doublet production temperatures and thermal energy curves.

4.6   Environmental studies

Environmental studies were conducted with the aim of observing the environmental impacts of diamond drilling at the site. The environmental studies consisted of a background study conducted prior to drilling, environmental monitoring of surface waters, stream sediments and stream benthos, and a bedrock groundwater study from the drilled borehole. Here, only a brief overview of the

studies is presented, since the background studies, environmental study methods and their results are further discussed in detail in reports by Lukkarinen et al. 2024 (in preparation) and Hatakka (2023).

4.6.1   Background study

Prior to drilling in autumn 2020, 39 soil samples, 7 humus samples and 9 surface water samples were collected from the surroundings of the planned drill site. All soil samples collected were from till. All metal concentrations were relatively low and below PIMA threshold values. The metal concentrations of the humus samples were above the average in Finland. Only lead, molybdenum and zinc were below average. Compared to the average concentrations in Finland, surface water samples also had higher concentrations of arsenic, cobalt, iron, and manganese (Hatakka 2023).

4.6.2   Environmental monitoring

Environmental monitoring was conducted during drilling in February 2021 and continued annually after drilling in summer and late autumn during 2021–2023. The monitoring sites are presented in Figure 43. Visaoja was used as a reference sampling site for benthos samples, as it is not connected to the water bodies in the vicinity of the drillhole.
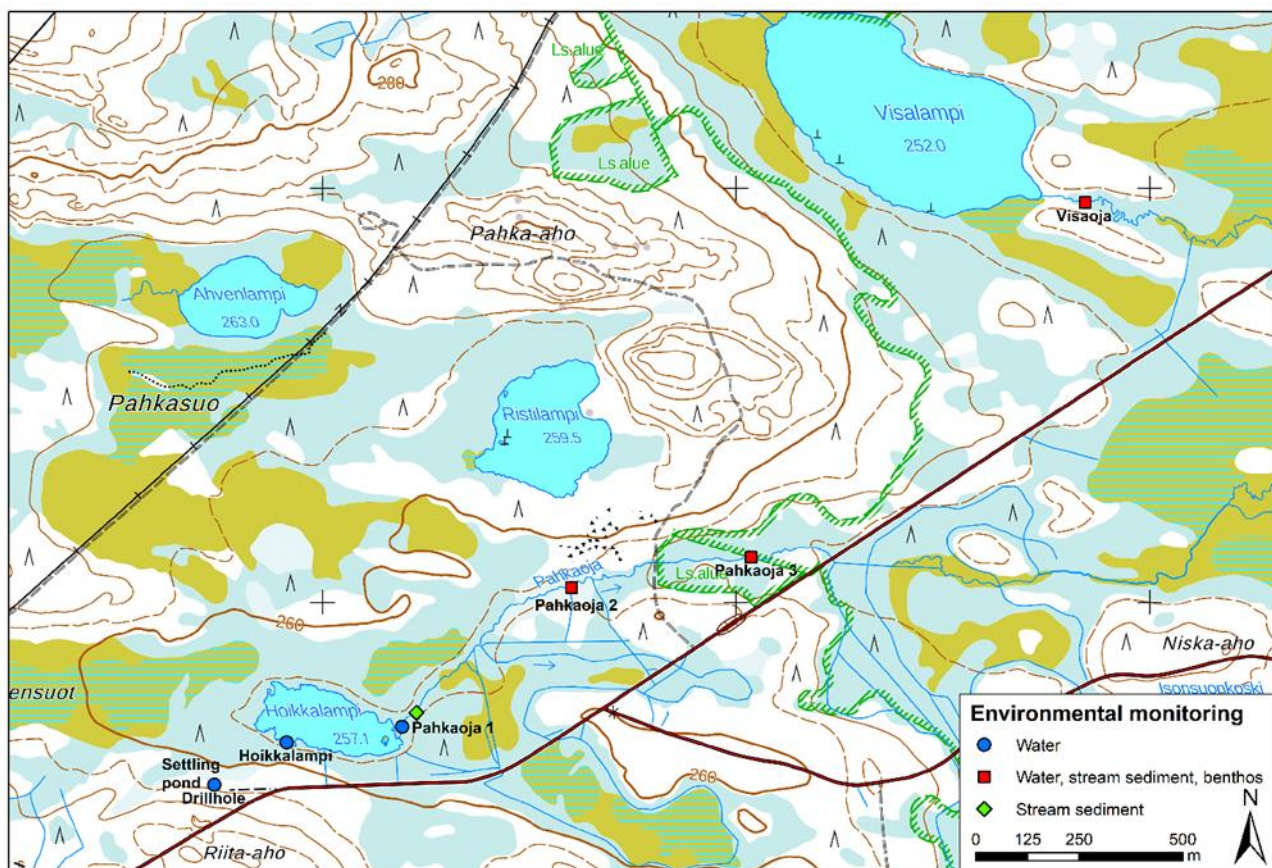

Figure 43. Map of environmental monitoring sites. The deep drillhole and settling pond are in the same location and point (blue).

4.6.2.1 Deep groundwater

In July 2021, the water from the borehole was sampled with a tube sampler (Figure 44). The tube was slowly lowered into the drillhole. The sampler hit an obstacle at the depth of 1155 m, where it was left to equalize overnight. The next day, the tube was lifted from the drillhole and water samples were collected every 100 m. Field measurements (oxygen, pH, EC, redox) were taken every 50 m with a YSI ProDSS multiparameter probe. The nearby shallow drillhole was sampled with a bailer for comparison, but only one sample, from 100 m depth, was obtained due to the bailer becoming stuck when attempting to collect deeper samples.

Dissolved and total cations, anions, TOC and DOC were analysed in the laboratory of Eurofins. Stable isotopes of oxygen and hydrogen were analysed in the GTK isotope laboratory. The drillhole was cemented down to 900 m depth, and the results of the tube sampling were therefore quite uniform. The effects of the cementing can presumably also be seen in the results for pH (8.3–9.5).

In July 2022, a second attempt at tube sampling of the deep drillhole was planned, but the sampler became stuck at the depth of 330 m. The sampler was successfully retrieved later in August/September. Sampling was not attempted again, as the risk of equipment becoming stuck was high. As a result, plans for further sampling of the drillhole and the waters in fractures with packers were also abandoned, and the deep groundwater studies were left inconclusive.

Figure 441. The head of the tube sampler (left). Lowering the tube into the drillhole (right).

4.6.2.2 Surface water

Surface waters were sampled in February, July, and November in 2021, and in June/August and October in 2022 and 2023. Samples were taken from the settling pond (only in 2021), Lake Hoikkalampi, three sites along the stream of Pahkaoja and a reference stream, Visaoja (only late autumn sampling) (Figure 44). Samples were taken by submerging the sample bottle into the lake or stream. Field measurements (oxygen, pH, EC, redox) were taken at each sampling point with a YSI ProDSS multiparameter probe. Alkalinity was titrated in the field. The samples were analysed for total and dissolved cations, anions, TOC, DOC and TSS (Eurofins) and for stable isotopes of oxygen and hydrogen (GTK). To estimate the amount of organic compounds originating from the drilling fluids, water samples were collected in February 2021 (while drilling was ongoing) from the mixture of water and drilling fluid going into the drillhole, coming out of the drillhole, from the settling ponds and from Pahkaoja 2. The samples were sent to the University of Eastern Finland for NMR spectroscopy.

There were some raised cation and anion concentrations compared to the background levels of the area (Lahermo et al. 1998, Tenhola and Tarvainen 2008) while drilling was ongoing and later in

summer 2021 after drilling had ended. However, concentrations had decreased to background levels by the next summer. Phosphorous spikes were detected in analysed water samples in summer 2021 and 2023. The drilling fluids did not contain phosphorous; therefore, the origin of the sporadic phosphorous loads could not be explained. Summer samples of 2023 had higher concentrations of Cr and Ni than during other samplings. During the project, all concentrations remained below the environmental quality standard.

NMR spectroscopy revealed that there were some polymers, amines/amides, carbonyls and hydrocarbons in the water rising from the drillhole during drilling. However, the settling ponds were efficient in removing the organic compounds, and only small concentrations of carbonyls were therefore eventually detected in Pahkaoja 2.

4.6.2.3   Stream sediments

Stream sediment samples were collected from 3 sites along Pahkaoja stream and one from Visaoja stream (Figure 44). The sediment samples were collected from the bottom of the stream using a sediment net. The samples were analysed for main elements and loss on ignition by Eurofins.

Pahkaoja 2, 3 and the Visaoja reference site had raised concentrations of aluminium, arsenic, boron, cobalt, iron, manganese, molybdenum and zinc. Since the reference site also had raised concentrations, it can be assumed that they are characteristic of the area. Otherwise, concentrations were mainly the same or less than the median in the area (Lahermo et al. 1996, Tenhola and Tarvainen 2008).

4.6.2.4   Benthos

Benthos samples were collected from Pahkaoja 2 and Pahkaoja 3, and from Visaoja for reference (Figure 44). The samples were taken by kicking the stream bottom so that detritus and benthos flowed into a kick net. The samples were immediately sieved and preserved in Etax-A ethanol. The benthos were identified and reported by Probenthos Oy.

On a scale of poor to excellent, the conditions of the benthos in Pahkaoja 2 and 3 in 2021 were excellent and in 2022 were good (Pahkaoja 3) and satisfactory (Pahkaoja 2). The differences in species composition were small and the change is assumed to represent normal annual variation. The benthos conditions in Visaoja were good in both years. The results for 2023 are still pending and will be further discussed in the report by Lukkarinen et al. 2024 (in preparation).

4.7   Structural geology studies

Structural geology studies were conducted from August 2021 to April 2022. The work consisted of logging the optical borehole images (OBI) and traditional structural core logging from the Koillismaa Deep Hole.

4.7.1   Optical borehole image logging
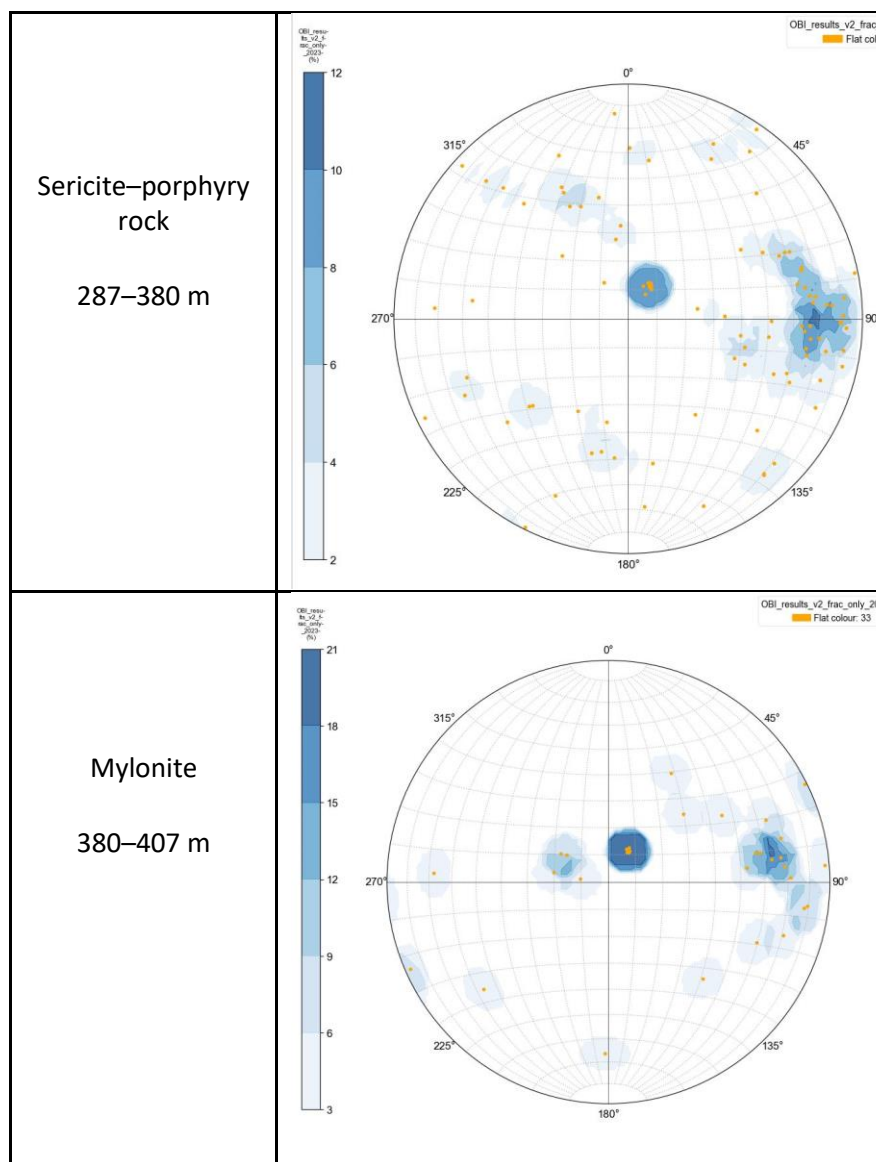
Optical borehole imaging was performed in the deep hole in August 2021 by Astrock oy. The OBIs were used to log fractures, foliations and lithological contacts. Fractures were further divided into three groups: closed/filled fractures, partially filled fractures and open fractures, with the latter having the aperture recorded in addition to the orientation. Structural logging began from 287

metres depth, because the drillhole is cased down to that depth, and continued to a depth of 1149 metres, where the drillhole had apparently collapsed and the OBI instruments could not be lowered further.

Altogether, 2470 total structural measurements were mapped from the deep hole, starting from 287 metres downhole to 1149 metres. Structural data from the 863 metres of the borehole included 1730 filled fractures, 483 partially filled fractures, 122 open fractures, 98 foliations and 37 lithological boundaries. Table 4 illustrates how the joint sets differ by depth and rock type.

Table 4. Stereo plots from fractures logged from OBI for each major rock type interval in the drillhole.

Tonalite gneiss 407–533 m	
Diabase 533–660 m	
Granite 660–920 m	

Diabase / Chlorite schist 920–928 m	
Granite 928–1145 m	
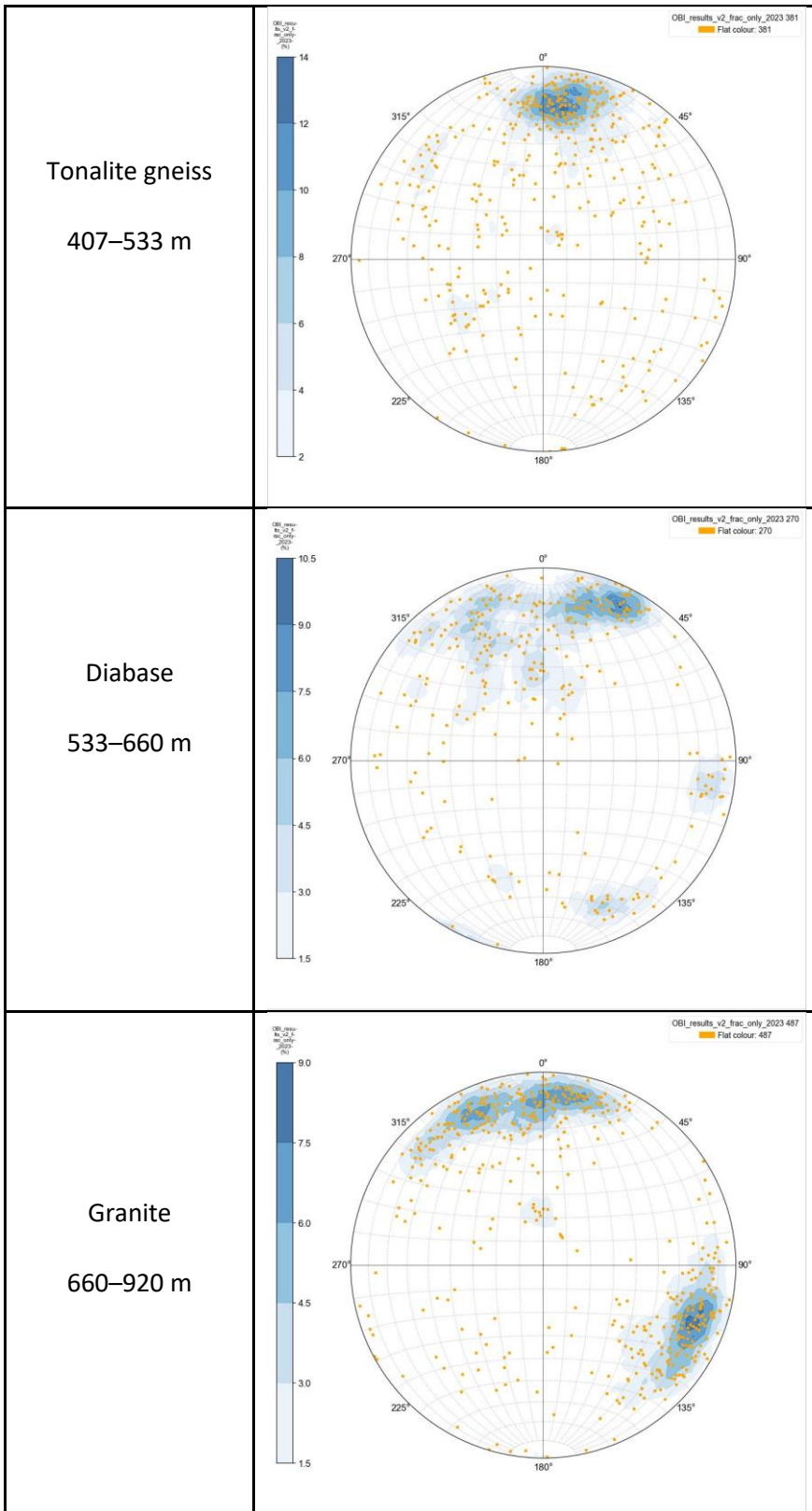
4.7.2   Structural drill core logging

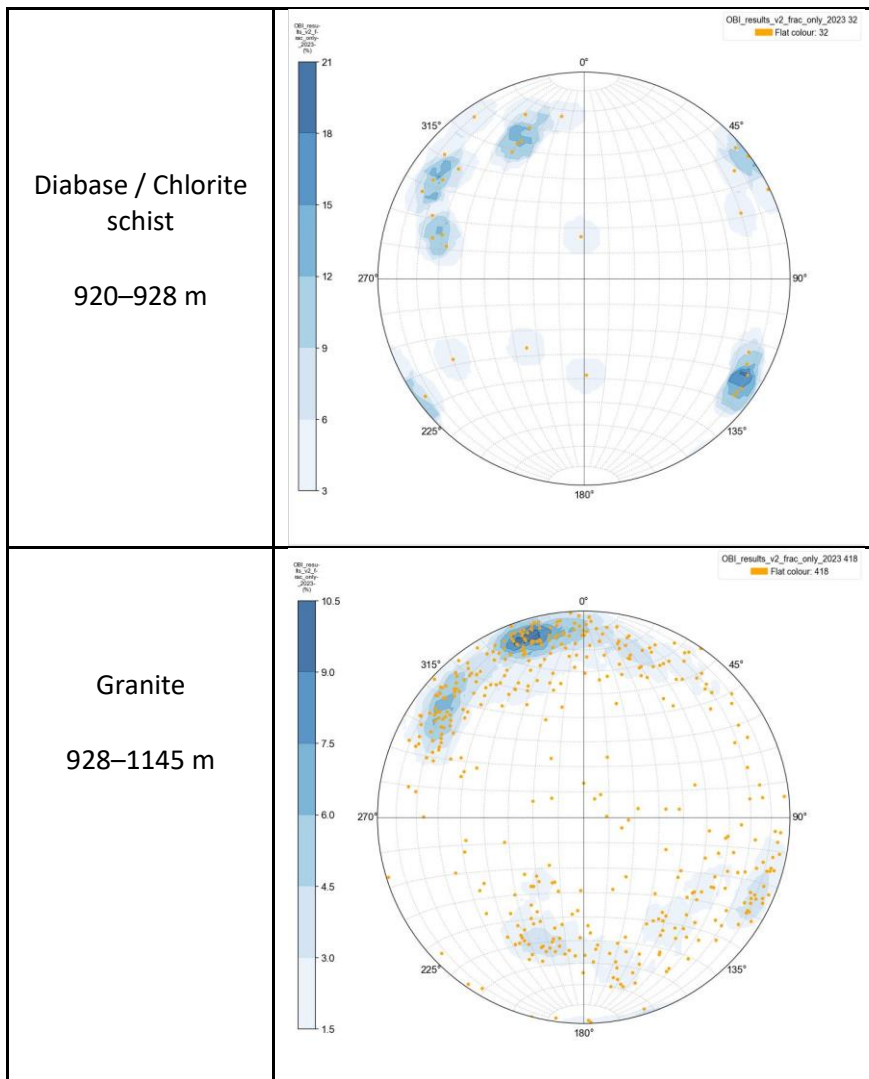Altogether, 417 structures were logged from the core in the core boxes in person, starting from a depth of 564 metres down to 1701 metres down hole, particularly focusing on sections below 1150 metres, where the optical borehole imaging instruments could not be lowered. According to current QA/QC standards, structures can only be logged from sections of the core where orientation marks can be connected, which means in the case of the deep hole that only 11.5% of the core was reliable. Most of the reliable sections were above the ultramafic units, which begin from 1407 metres depth. Additional structural measurements were still taken from sections that had a single orientation mark. Information logged from each fracture included depth, alpha and beta angles, the fracture surface colour, fracture filling mineral, filling mineral thickness, fracture openness, shape, and roughness. The gamma angle and movement direction were recorded from lineations on slickenside surfaces from faults. Accordingly, the interpretations of movement along the faults were made from slickenside surfaces (Figure 45).
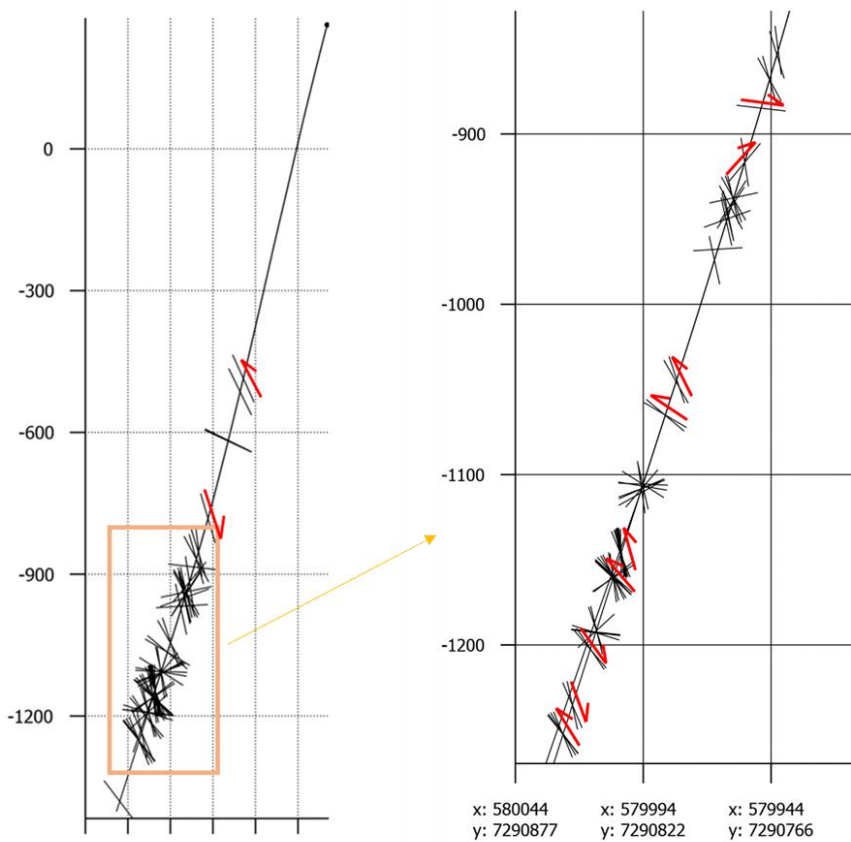
Figure 45. Left: Cross-section with joints that have lineation recorded visualized along the deep hole. View perpendicular to the drillhole, azimuth: 312. Right: Section of the drillhole from 1150 m to 1600 m, view perpendicular to the drillhole, azimuth: 312. Fault movement interpreted from slickenside lineations and visualized with red arrows. Joints with no sense of movement in the figure either had movement both up and down dip recorded, or the movement direction was unclear.

4.7.3   Method comparison

The OBI results were compared with the results from traditional core logging, which was also performed in two different ways: with an IQ logger and with the manual core angle technique (Leskelä, 2023). Logging from OBIs was found to be the superior method for joint logging, as it allows work to be conducted throughout the drill core, whereas the other methods are only applicable where the orientation marks on the core can be connected. The manual core angle technique is recommended alongside OBI logging to validate the results, and for measuring lineations.

5   PLANS AND PUBLICATIONS

Authors	Title	Type	Status
Alan Bischoff, Michael John Heap, Perttu Mikkola, Jukka Kuva, Thierry Reuschlé, Ester M Jolis, Jon Engström, Heini Reijonen, Tuomas Leskelä	Hydrothermally altered shear zones: a new reservoir play for the expansion of deep geothermal exploration in crystalline settings	Peer reviewed (joint work with the Deep-HEAT-Flows project)	Accepted for publication on 10.12.2023 DOI:10.2139/ssrn.4612277

Teemu Anttilainen	Koillismaan syväreiän happamien kivilajien iänmääritys sekä geokemiallinen ja petrografinen luokittelu	MSc Thesis	Published
Noora Thurman, Tuomo Karinen, Heikki Salmirinne & Jonna Tirroniemi	Koillismaan Pintamon kerrosintruusiolohkon potentiaalikenttäaineiston mallinnus ja geologinen 3D-malli	GTK Open File Work Report	Published
Tuomas Leskelä	Fracture measurement method comparison from the Koillismaa deep drillhole	GTK Open File Work Report	Published
Uula Autio and Cedric Patzer	Koillismaa Deep Hole controlled source AMT experiment and EM modelling developments	GTK Open File Work Report	Published
Tuomo Karinen, Matti Kurhila, Jukka Konnunaho, Marko Moilanen	The Koillismaa Deep Intrusion: Insights into the parental magmas of the 2.45 Ga Koillismaa-Näränkävaara Layered Igneous Complex	Peer reviewed	In preparation
Esa Heilimo, Perttu Mikkola, Teemu Anttilainen, Matti Kurhila, Jussi Heinonen	Koillismaa 2.45 Ga A-type granitoids, new additions to the story from depth	Peer Reviewed	In preparation
Michal Malinowski, Bojan Brodic, Ilkka Martinkauppi, Elina Koskela, and Viveka Laakso	Distributed acoustic sensing walkaway vertical seismic profiling in Koillismaa deep drillhole	Extended abstract	Published
Michal Malinowski, B. Brodic, Ilkka Martinkauppi, Elina Koskela, and Viveka Laakso	Distributed acoustic sensing vertical seismic profiling in hardrock environment: case study from Koillismaa drillhole, Finland	Extended abstract	Published
Suvi Heinonen, Maarit Nousiainen, Tuomo Karinen and Tuulia Häkkinen	Are Seismic P-Wave Velocities Capable of Revealing the Deep-Seated Prospective Intrusion?	Extended abstract (joint work with the SEEMS DEEP project)	Published
Maarit Nousiainen, Suvi Heinonen and Tuomo Karinen	Petrophysics of the Koillismaa drill hole	Extended abstract (joint work with the SEEMS DEEP project)	Published
Tuomo Karinen, Suvi Heinonen, Jukka Konnunaho, Heikki Salmirinne, Ilkka Lahti, and Aleksi Salo	Koillismaa Deep Hole – solving the mystery of a geophysical anomaly	Extended abstract	Published
Tarja Hatakka	Maaperän geokemialliset taustapitoisuudet Koillismaan syväreiän ympäristössä	GTK Open File Work Report	Published

Vaula Lukkarinen	Environmental monitoring and impacts of drilling in the Koillismaa deep hole site	GTK Open File Work Report	In preparation
Matti Kinnunen	Snow and soil geochemical studies of Koillismaa	GTK Open File Work Report	In preparation
Matti Kurhila, Teemu Anttilainen, Tuomo Karinen, Perttu Mikkola	Geochronology of the unexposed crust within the Finnish Archean – insights from the Koillismaa Deep Hole in Kuusamo, northeastern Finland	Extended abstract	Published

6   REFERENCES

Alapieti, T. 1982. The Koillismaa layered igneous complex, Finland – its structure, mineralogy, and geochemistry, with emphasis on the distribution of chromium. Geological Survey of Finland, Bulletin 319, 116 p.

Alapieti, T. T., Filén, B. A., Lahtinen, J. J., Lavrov, M. M., Smolkin & V. F., Voitsekhovsky, S. N. 1990. Early Proterozoic Layered Intrusions in the Northeastern Part of the Fennoscandian Shield. Mineralogy and Petrology 42, p. 1–22. https://doi.org/10.1007/BF01162681

Anttilainen, T. 2023. Koillismaan syväreiän happamien kivilajien iänmääritys sekä geokemiallinen ja petrografinen luokittelu. University of Turku, M.Sc. thesis, 69 p. In Finnish with English abstract. https://urn.fi/URN:NBN:fi-fe2023032032543

Bayanova T., Korchagin A., Mitrofanov, A., Serov, P., Ekimova, N., Nitikina, E., Kamensky, I., Elizarov, D. & Huber, M. 2019. Long-Lived Mantle Plume and Polyphase Evolution of Palaeoproterozoic PGE Intrusions in the Fennoscandian Shield. Minerals 9, 22 p. https://doi.org/10.3390/min9010059

Beck, AE. 1988. Methods for determining thermal conductivity and thermal diffusivity. In: Hanel, R., Rybach, L., and Stegena, L. (eds.), Handbook of Terrestrial Heat Flow Density Determination. Dordrecht: Kluwer, p. 87-124.

Bischoff, A., Heap, MJ., Mikkola, P., Kuva, J., Reuschlé, T., Jolis, E.M. Engström, J., Reijonen, H., Leskelä, T. 2023. Hydrothermally Altered Shear Zones: A New Reservoir Play for the Expansion of Deep Geothermal Exploration in Crystalline Settings. Available at SSRN: https://ssrn.com/abstract=4612277 or http://dx.doi.org/10.2139/ssrn.4612277

Brace W., Walsh J.B., Frangos W.T. 1968. Permeability of granite under high pressure. Journal of Geophysical Research, 73, 2225–2236. https://doi.org/10.1029/JB073i006p02225

Breede, K., Dzebisashvili, K., Liu, X. et al. 2013. A systematic review of enhanced (or engineered) geothermal systems: past, present, and future. Geotherm Energy 1, 4. https://doi.org/10.1186/2195-9706-1-4

Brown, D., DuTeaux, R., Kruger, P., et al. 1999. Fluid Circulation and Heat Extraction from Engineered Geothermal Reservoirs. Geothermics, 28, p. 553–572. https://doi.org/10.1016/S0375-6505(99)00028-0

Bruker. 2018. Mineral composition analysis using the M4 TornadoAmics. Lab report XRF 469, Micro-XRF-Application-Note-XRF-469-Mineral-composition-analysis-using-M4-TORNADO-AMICS-EN-BRUKER.pdf

Choquette, PW., Pray, L. 1970. Geologic nomenclature and classification of porosity in sedimentary carbonates. American Association of Petroleum Geologists. Bulletin, 54, p. 207–250.

Falcon-Suarez, I., Bayrackci, G., Minshull, T.A., North, L.J., Best, A.I., Rouméjon. 2017. Elastic and electrical properties, and permeability of serpentinites from Atlantis Massif, Mid-Atlantic Ridge 2017. Geophysical Journal International, Vol. 211, No. 2 Oxford University Press (OUP) p. 686-699.

Frey, M., Bär, K., Stober, I. et al. 2022. Assessment of deep geothermal research and development in the Upper Rhine Graben. Geotherm Energy 10, 18 (2022). https://doi.org/10.1186/s40517-022-00226-2

Gislason, G., Heinonen, S., Salmirinne, H., Konnunaho, J., and Karinen, T. 2019. KOSE-Koillismaa Seismic Exploration survey: Acquisition, processing, and interpretation. Geological survey of Finland, GTK Open File Work Report, 101/2019, 33p. https://tupa.gtk.fi/raportti/arkisto/101_2018.pdf

Gustafsson, S. E. 1991. Transient plane source techniques for thermal conductivity and thermal diffusivity measurements of solid materials. Review of scientific instruments, 62(3), p. 797-804. https://doi.org/10.1063/1.1142087.

Hanski, E., Walker, R. J., Huhma, H. & Suominen, I. 2001. The Os and Nd isotopic systematics of c. 2.44 Ga Akanvaara and Koitelainen mafic layered intrusions in northern Finland. Precambrian Research 109, p. 73–102. https://doi.org/10.1016/S0301-9268(01)00142-5

Hatakka, T. 2023. Maaperän geokemialliset taustapitoisuudet Koillismaan syväreiän ympäristössä. Geological Survey of Finland , Open File Work Report 46/2023, 24p.

Heap, M. J., Lavallée, Y., Petrakova, L., Baud, P., Reuschlé, T., Varley, N. R., & Dingwell, D. B. 2014. Microstructural controls on the physical and mechanical properties of edifice-forming andesites at Volcán de Colima, Mexico. Journal of Geophysical Research: Solid Earth, 119(4), p. 2925-2963. https://doi.org/10.1002/2013JB010521

Heap, MJ; Kushnir, ARL., Vasseur J., Wadsworth JB., Harlé, P., Baud, P., Kennedy, BM., Troll, VR., Deegan, FM. 2020. The thermal properties of porous andesite. Journal of Volcanology and Geothermal Research, Volume 398. https://doi.org/10.1016/j.jvolgeores.2020.106901.

Heap, M. J., Wadsworth, F. B., & Jessop, D. E. 2023. The thermal conductivity of unlithified granular volcanic materials: The influence of hydrothermal alteration and degree of water saturation. Journal of Volcanology and Geothermal Research, 435, 107775. https://doi.org/10.1016/j.jvolgeores.2023.107775.

Heinonen, S., Nousiainen, M., Karinen, T. and Häkkinen, T. 2022. Are Seismic P-Wave Velocities Capable of Revealing the Deep-Seated Prospective Intrusion? NSG2022 4th EAGE Conference on Geophysics for Mineral Exploration and Mining, Extended Abstract.

Hölttä, P. and Heilimo, E. 2017. Metamorphic map of Finland. In: Nironen, M. (ed.) Bedrock of Finland at the scale 1:1 000 000 – Major stratigraphic units, metamorphism and tectonic evolution. Geological Survey of Finland, Special Paper 60, 77–128

GTK

Hölttä, P., Mänttäri, I., Huhma, H., Kurhila, M., Ruotoistenmäki, T., Kontinen A. 2021. Growth of the Archean sialic crust as revealed by zircon in the TTGs in eastern Finland. Bulletin of the Geological Society of Finland 93, 77–104. https://doi.org/10.17741/bgsf/93.2.001

Iljina, M. & Hanski, E. 2005. Layered mafic intrusions of the Tornio-Näränkävaara belt. In: Lehtinen, M. et al. (eds.), Precambrian geology of Finland – key to the evolution of the Fennoscandian Shield. Developments in Precambrian Geology 14. Elsevier, pp. 101–137.

Iljina, M., Maier, W. D. & Karinen, T. 2015. PGE-(Cu-Ni) Deposits of the Tornio-Näränkävaara Belt of Intrusions (Portimo, Penikat, and Koillismaa). In: Maier, W. D. et al. (eds.), Mineral Deposits of Finland. Elsevier, pp. 134–164.

Iljina, M., Salmirinne, H., Heikura, P. 2006. Tutkimustyöselostus Kuparivaaran valtauksella (7655/1) Kuusamossa suoritetuista tutkimuksista vuosina 2003–2004. Geologian tutkimuskeskus, Mineral exploration report M06/4523/2006/1/10. https://tupa.gtk.fi/raportti/valtaus/m06_4523_2006_1_10.pdf

Jolie, E., Scott, S., Faulds, J. et al. 2021. Geological controls on geothermal resources for power generation. Nat Rev Earth Environ 2, p. 324–339. https://doi.org/10.1038/s43017-021-00154-y

Järvinen, V., Halkoaho, T., Konnunaho, J., Heinonen, J.S., Kamo, S., Davey, S., Bleeker, W., Karinen, T., Rämö, T. 2022. Petrogenesis of the Paleoproterozoic Näränkävaara layered intrusion, northern Finland, Part II: U-Pb ID-TIMS age and Sm-Nd isotope systematics. Bulletin of the Geological Society of Finland, Vol. 94, 2022, pp 53–74. https://doi.org/10.17741/bgsf/94.1.003

Karinen, T. 2010. The Koillismaa intrusion, northeastern Finland – evidence for PGE reef forming processes in the layered series. Ph. D. thesis, Geological Survey of Finland, Bulletin 404, 176 p.

Kelbert, A., Meqbel, N., Egbert, G.D., Tandon, K. 2014. ModEM: A modular system for inversion of electromagnetic geophysical data 2014. Computers & Geosciences, Vol. 66 p. 40–53.

Key, K. 2016. MARE2DEM: a 2-D inversion code for controlled-source electromagnetic and magnetotelluric data 2016. Geophysical Journal International, Vol. 207, No. 1 p. 571–588.

Kohonen, J., Rämö, OT. 2005. Sedimentary rocks, diabases, and late cratonic evolution. In Precambrian geology of Finland. Elsevier Scientific Publ. Co., pp. 563-604. https://doi.org/10.1016/S0166-2635(05)80014-3

Kontinen, A., Huhma, H., Lahaye, Y. & O'Brien, H. 2013. New U-Pb zircon age, Sm-Nd isotope, and geochemical data on Proterozoic granitic rocks in the area west of the Oulunjärvi Lake, Central Finland. In: Hölttä, P. (ed.) Current Research: GTK Mineral Potential Workshop, Kuopio, Geological Survey of Finland. Report of Investigation 198, 70–74.

Kukkonen, I., Heikkinen, P., Malin, P., et al. 2023. Hydraulic conductivity of the crystalline crust: Insights from hydraulic stimulation and induced seismicity of an enhanced geothermal system pilot reservoir at 6 km depth, Espoo, southern Finland, Geothermics, Volume 112. https://doi.org/10.1016/j.geothermics.2023.102743.

Kärenlampi, K., Kontinen A., Huhma H., Hanski E. 2019. Geology, geochronology, and geochemistry of the 2.05 Ga gneissic A1-type granites and related intermediate rocks in central Finland: implication

for the tectonic evolution of the Karelia craton margin. Bulletin of the Geological Society of Finland 91, p. 35–73. https://doi.org/10.17741/bgsf/91.1.002

Lahermo, P., Väänänen P., Tarvainen, T. & Salminen, R. 1996. Geochemical atlas of Finland. Part 3, Environmental geochemistry: stream waters and sediments. Geological Survey of Finland.

Laukamp, C., Rodger, A., LeGras, M., Lampinen, H., Lau, IC., Pejcic, B., Stromberg, J., Francis, N., Ramanaidou, E. 2021. Mineral Physicochemistry Underlying Feature-Based Extraction of Mineral Abundance and Composition from Shortwave, Mid and Thermal Infrared Reflectance Spectra. Minerals 2021, 11, 347. https://doi.org/10.3390/min11040347

Lauri, L.S., Mikkola, P. & Karinen, T. 2012. Early Paleoproterozoic felsic and mafic magmatism in the Karelian province of the Fennoscandian shield. Lithos 151, 74–82. https://doi.org/10.1016/j.lithos.2012.01.013

Lauri, L.S., Rämö, O.T., Huhma, H., Mänttäri, I., Räsänen, J. 2005. Petrogenesis of silicic magmatism related to the 2. 44 Ga rifting of Archean crust in Koillismaa, eastern Finland. Lithos 86, 137–166. https://doi.org/10.1016/j.lithos.2005.03.016

Leskelä, T. 2023: Fracture measurement method comparison from the Koillismaa deep drillhole. Geologian tutkimuskeskus. Open File Work Report 11/2023. 12 p.

Li, Y., Karrenbach, M. and Ajo-Franklin, J (Eds.). 2022. Distributed acoustic sensing in geophysics: Methods and applications. John Wiley & Sons.

McLeod, RL., Gabell, AR., Green, AA., Gardavsky, V. 1987. Chlorite Infrared Spectral Data as Proximity Indicators of Volcanogenic Massive Sulphide Mineralization. The Australasian Institute of Mining and Metallurgy, Pacific Rim Congress, Melbourne, Proceedings, v. 87, p. 321–324.

Nironen, M. 2017. Guide to the Geological Map of Finland. In: Nironen, M. (ed.) Bedrock of Finland at the scale 1:1 000 000 – Major stratigraphic units, metamorphism, and tectonic evolution. Geological Survey of Finland, Special Paper 60, p. 41–75.

Nordbäck, N., Ovaskainen, N., Markovaara-Koivisto, M., Skyttä, P., Ojala, A., Engström, J., Nixon, C. 2023. Multiscale mapping and scaling analysis of the censored brittle structural framework within the crystalline bedrock of southern Finland. Bulletin of the Geological Society of Finland 95 (1), p. 5–32. https://doi.org/10.17741/bgsf/95.1.001

Pajunen, M. and Poutiainen, M. 1999. Palaeoproterozoic prograde metasomatic-metamorphic overprint zones in Archaean tonalitic gneisses, eastern Finland. Bulletin of the Geological Society of Finland 71, p. 73–132. https://doi.org/10.17741/bgsf/71.1.005

Piirainen, T., Hugg, R., Aario, R., Forsström, L., Ruotsalainen, A. & Koivumaa, S. 1978. Koillismaan malmikriittisten alueiden tutkimusprojektin loppuraportti 1976. Geological Survey of Finland, Report of investigation 18. 51 p.

Rodi, W., Mackie, R.L. 2001. Nonlinear conjugate gradients algorithm for 2-D magnetotelluric inversion 2001 Geophysics, Vol. 66, No. 1. Society of Exploration Geophysicists p. 174-187.

Scheidegger, A. 1974. The physics of flow through porous media, 3rd Edition, University of Toronto Press, Toronto, Canada.

Sruoga, P. and Rubinstein, N. 2007. Processes controlling porosity and permeability in volcanic reservoirs from the Austral and Neuquén basins, Argentina. AAPG Bulletin, 91, p. 115–129, https://doi.org/10.1306/08290605173

Tenhola, M., & Tarvainen, T. 2008. Purovesien ja orgaanisten purosedimenttien alkuainepitoisuudet Suomessa vuosina 1990, 1995, 2000 ja 2006. Geologian tutkimuskeskus.

Thurman, N., Karinen, T., Salmirinne, H., Tirroniemi, J. 2023. Koillismaan Pintamon kerrosintruusiolohkon potentiaalikenttäaineiston mallinnus ja geologinen 3D-malli. Geologian tutkimuskeskus. Open File Work Report 53/2023, 27 p. https://tupa.gtk.fi/raportti/arkisto/53_2023.pdf

Vuollo, J. & Huhma, H. 2005. Paleoproterozoic mafic dikes in NE Finland. In: Lehtinen, M., Nurmi, P. A. & Rämö, O. T. (eds.) Precambrian Geology of Finland: Key to the Evolution of the Fennoscandian Shield. Developments in Precambrian Geology 14. Elsevier, Amsterdam, pp. 195–236.